SOLVENT INGRESS IN POLYMERS

A thesis submitted to the University of Surrey for the degree of
Doctor of Philosophy

Robert Sackin

Department of Physics, University of Surrey
September 2000

Corrections

Page 2 line 5: this should read: "The amorphous molecules are random coils with each molecule overlapping with its neighbours."

Page 30 line 3: a fullstop should be inserted so that the sentence now ends: "$\ldots \tau_c < T_2$."

Page 43 line 9: "Hann" should be written "Hahn".

Page 62 line 9: the sentence starting with "Their are..." should begin "There are...".

Page 66 at end of the caption for Figure 3.2 the following sentence should be added: "Every fifth profile is shown giving a time between profiles of about 2.5 hours."

Page 68: the last line on the page should end: "...found experimentally are...".

Page 135 line 10 should be: "... effective viscosity of the glass η_g. If we follow this suggestion then swelling takes a time of order $\eta_g/(ckT)$, where ckT is an approximation to the osmotic pressure exerted by the solvent."

Page 135 line 15 should be: "... the solvent diffuses in a time $\eta_g/(ckT)$. This is $(D_g\eta_g/ckT)^{1/2}$."

Page 140 equation 6.18: this should read $F_2 = \frac{D_v(p_{tol} - p_{PS})}{d_2RT}$.

Page 140 equation 6.19: this should read $F_1 = \frac{A_3D_v(p_{tol} - p_{PS})}{A_1d_2RT}$.

Page 185 reference [78]: "Hann" should be written "Hahn".

Abstract

The understanding of solvent ingress into polymers is of vital importance in a plethora of applications that embrace such diverse technologies as dental resins and food systems. Two limiting regimes of small molecule diffusion in polymers are widely acknowledged: Fickian and Case II. Fickian diffusion is associated with solvent uptake proceeding with the square root of time and with smooth concentration profiles. Case II ingress is characterised by uptake that is linear with time and by concentration profiles with sharp fronts. This thesis describes new insight into both these transport mechanisms. Binary mixtures of good (methyl ethyl ketone) and bad (ethanol) solvents ingressing polystyrene with Fickian dynamics are investigated. Using both ^{2}H magnetic resonance imaging (MRI) with selectively deuterated solvents and ^{13}C-^{1}H cyclic cross-polarisation chemically selective imaging of normal solvents, the individual components are separately measured. The two solvents are found to ingress together but they have different spatial concentration profiles. These results are explained in terms of a simple model. In a further study using both MRI and ellipsometry, no polymer molecular weight dependence is observed for Fickian solvent ingress. Powerful evidence of a new rate-limiting step to give Case II diffusion is demonstrated. We show that the rate-limiting step can be the solvent flux at the polymer surface as well as the visco-elastic polymer swelling. Numerical simulations of a simple phenomenological model demonstrating these effects are presented. They are supported by experimental measurements of liquid and vapour toluene ingress into polystyrene using MRI and stray field imaging. One problem with ellipsometry for measuring Fickian ingress is that it is difficult to unambiguously fit the ψ and Δ data to the smooth refractive index profile through the swelling sample. Two methods have been implemented to overcome this problem: a Born approximation and a Bayesian inference technique. The latter has shown that ellipsometry can now, in theory, be described as a model independent technique.

Contents

Acknowledgments

Thanks must go first to Professor Peter McDonald and Dr Joe Keddie for their thorough supervision over the last three years. I would like to acknowledge the Engineering and Physical Sciences Research Council who provided me with a studentship . I am extremely grateful to post-docs past and present who have worked with me especially Dr John Godward with whom I shared the efforts required to produce beautiful polystyrene swelling experiments, Dr Eli Ciampi for her input in the CYCLOCROP experiments and to Drs Ben Newling and Ute Gorke who worked patiently with me on early DQF experiments. Thanks go too, to Dr Richard Sear for help in developing the model of surface-flux-limited Case II diffusion described in Chapter 6 and Dr Nuno Barradas who quickly and enthusiastically modified and ran his SA-MCMC programs for me. I am grateful to the British Council and JISTEC who. in funding a Research Experience for European Students Fellowship to visit Japan in the summer of 1999, provided me with the oppurtunity to do battle with a Japanese MRI machine. I would also like to thank Dr Koji Saito and Mr Koji Kanehashi, my hosts at Nippon Steel, who made this trip by far the most culturally rich experience of my PhD. Back at Surrey, I would like to thank Ray, Brian, Willy and Roger who made vital pieces of equipment for me, invariably last thing on a Friday afternoon, and to the current and past inhabitants of room four for their input into a huge variety of useful discussions.

Chapter 1

Introduction

1.1 What is a polymer?

1.1.1 Polymer structure

A polymer is a large molecule made from one, two or occasionally more types of small repeat units, sometimes called "mers". There may be hundreds, thousands, millions or even billions of repeat units forming a single polymer molecule. In the synthesis of a polymer, small molecules called monomers are reacted to form a large molecule. Copolymers are polymers composed of two or more different monomers. If each repeat unit is bonded to only two other units (it is said that the functionality is equal to two) then a linear polymer is formed. However, if the functionality is greater than two then a crosslinked network is made. When the backbone of a polymer chain carries two dissimilar atoms or groups then the polymer may be found with different tacticity or stereoregularity. If the groups are all along the same side of the backbone then the polymer is termed isotactic. In syndiotactic polymers the pendant groups are located on alternate sides of the backbone. In atactic polymers, however, the pendant groups are randomly arranged along the polymer chain. A multitude of individual long-chain polymer molecules are held together by stabilising forces (usually van der Waals' forces) acting between them, to form bulk material. [1] Crystalline polymeric materials have their molecules arranged in a regular and ordered fashion. Amorphous molecules' conformation is a random coil with each molecule overlapping with its neighbours. Amorphous polymeric materials have properties that share characteristics with glass.

1.1.2 The mechanical response of polymers

Glassy polymers are elastic, i.e. obey Hooke's law. They fail cleanly and suddenly, usually after deformations of only a few percent [1], but at any strain below failure, deformation is completely reversible. They have a high Young's modulus which reflects the fact that large forces are needed to move atoms even a tiny amount. Glasses do not show a sharp phase change from solid to liquid at a definite melting point. They change gradually. The glassy state occurs below T_g (the glass transition temperature). Above T_g the polymer is in a rubbery state. There is a transition region of about 20°C between the two. [1] T_g can be reduced for a particular polymer by, for instance, the addition of solvent or the reduction of polymer molecular weight. Rubbery polymers (also termed elastomers) are also elastic but a stress-strain graph is characteristically curved, with varying Young's modulus at large strains. This indicates that Hooke's law is disobeyed. Rubbery polymers can frequently be extended to ten times their unstrained length [2] and their mean Young's modulus is low (between 100 and 1000 times less than for glassy polymers). [1] This is due to the fact that the constituent molecules can rearrange themselves in response to an applied stress. They are ultimately restrained by chemical crosslinks. In the case of polymers such as glassy poly (methyl methacrylate) (PMMA) and polystyrene (PS), where there are no chemical crosslinks, chain entanglements serve the same role in restricting chain motion. However, for entanglement-reliant, rubbery polymers these entanglements eventually free themselves leading to irreversible chain movements and plastic deformation.

1.1.3 The molecular weight of a polymer

The relative molecular mass (RMM) is defined as the relative atomic mass of the constituent atoms. [1] In a real polymer sample, the individual chains have a range of different lengths, and so a number-average relative molecular mass M_N and a weight-average relative molecular mass M_W are used to describe the distribution of chain lengths. The chain length of a polymer molecule is proportional to RMM. The number average chain length is given by

$$n_N = \frac{\sum_i f_i N n_i}{N} = \sum_i f_i n_i \tag{1.1}$$

where, for the ith different chain length, f_i is the fraction of chains with length n_i in a total of N molecules. This definition provides equal weighting to every molecule whatever its size. However, the length-average weights the average to bias a chain proportional to its length. It is defined by

$$n_L = \frac{\sum_i f_i N n_i \times n_i}{\sum_i f_i N n_i} = \frac{\sum_i f_i n_i^2}{\sum_i f_i n_i}. \tag{1.2}$$

We can write a number-average relative molecular mass M_N and a weight-average relative molecular mass as

$$M_N = n_N M_l \tag{1.3}$$

and

$$M_W = n_L M_l, \tag{1.4}$$

respectively. M_l is the relative molecular mass per repeat unit in the polymer chain. The ratio M_W/M_N is called the polydispersity and is equal to unity when all the molecules in a polymer sample have the same chain length and mass. If this condition is true, then the material is called monodisperse. In nearly every synthetic polymer, $M_W/M_N > 1$.

1.2 A brief history of engineering polymers

The first manmade polymer (a form of cellulose nitrate) appeared at the 1862 Great International Exhibition. [2] It was called Parkesine after Alexander Parkes. He was no stranger to the invention of new materials having already sold a patent for a waterproof fabric to Charles Macintosh in 1843. However, Parkesine was not commercially viable. Successful commercial production of a polymer based on cellulose nitrate did not become possible until 1868 when John Hyatt, [3] after much experimentation in his kitchen, successfully met the challenge, set by the Phelan and Collander company, of finding a synthetic material of which billiard balls could be made. [2] This remained the only commercial polymer until Bakelite, named after the Belgian born scientist, Leo Baekeland, who accidently discovered it, was produced in 1907. [4] Thorough scientific research into polymers never really got going in the 19th century. Materials chemists of the day were only interested in producing highly pure new materials. Of course, one of the common tests for purity is a sharp melting point, something that a polymer does not have. Hence many early laboratory-produced polymers could well have been thrown away. In the 1920s Hermann Staudinger suggested that polymer molecules were chains. [5] He used the word macromolecule rather than polymer. Macro means "large" in Greek, and molecule comes from the Latin phrase meaning "tiny mass of something". After Staudinger's work was finally accepted by the scientific community in the 1930s (he eventually received his Noble Prize in 1953), a rational scientific framework for understanding polymers was formed. Large industrial companies began highly successful research programmes leading to the discovery of commercially viable processes for the production of nylon (by Du Pont), polyethylene (by ICI) and polystyrene (by Dow Chemical Company) amongst others. One should not forget that there are naturally occuring polymers such as starches and DNA, which is the longest polymer in existence, containing up to ten billion monomer units. [5]

1.3 What is solvent ingress?

Place a piece of polymeric material in a beaker of liquid or in vapour and the liquid or vapour will often penetrate the polymer causing it to swell. The kinetics of the system can be described using a chemical potential gradient which tends to zero with time, at which point the system is said to be in equilibrium. The chemical potential of a polymer solution is defined as the change in free energy resulting from the addition of one mole of solvent to an infinite amount of solution when temperature and presssure are held constant. [6]

1.3.1 Fick's law: Case I ingress dynamics

Fick's first law [7] describes the rate of the steady state of permeation through unit area of any medium. In one dimension it is written as:

$$J = -D\frac{\partial c}{\partial x} \tag{1.5}$$

where D is the diffusion coefficient, c is the concentration of penetrant and x is the distance. Fick's second law (easily derived from the first [8]) refers to the accumulation or loss of matter as a function of time, t, at any given point in the medium being investigated. It is written as:

$$\frac{\partial c}{\partial t} = \frac{\partial}{\partial x}\left[D\frac{\partial c}{\partial x}\right]. \tag{1.6}$$

Solving Equation 1.6 for boundary conditions for sorption in a semi-infinite medium:

$$c = c_0, \quad x = 0, \quad t > 0, \tag{1.7}$$

$$c = 0, \quad x > 0, \quad t = 0, \tag{1.8}$$

yields a solution for Fickian (also called Case I) dynamics of a solvent ingressing a polymer, that is characterised by smooth concentration profiles that move forward proportional to the square root of time. [8] Kinetically good solvents diffuse quickly through a polymer. They usually contain molecules that are physically small in size, such as methanol or water. [9]

1.3.2 Anomolous and Case II ingress dynamics

Concentration profiles other than those predicted by Fick's theory have been observed in polymer/ solvent systems. This is the so-called anomolous regime where the solvent front position is seen to move as $x \propto t^n$ where $1/2 < n < 1$. In 1965 Alfrey [10] coined the term Case II diffusion to describe the system where $n = 1$. Mills *et al* [11] described an idealised concentration profile for the Case II system. This profile has a constant penetrant concentration in the swollen region followed by a large, sharp drop in concentration at the boundary of the unswollen region. A Fickian precursor penetrates the polymer glass ahead of the solvent front. Mills and Kramer [12] studied a range of iodohexanes with different numbers of carbon atoms ingressing a glassy chemical photoresist that had a chemical composition similar to poly (methyl methacrylate). They saw that the values of the diffusion coefficient extracted from the Fickian precursor decreased strongly with the number of carbon atoms in the iodohexane. They also observed a similar decrease in the Case II front velocity.

1.3.3 Mechanical polymer relaxation

Theories abound to explain the anomolous and Case II phenomena. Some do not have any real physical basis, such as that proposed by Kwei *et al.* [13] Others, discussed below, have a thorough physical justification. These theories have one characteristic in common. Viscoelastic properties are incorporated to describe a time-dependent stress-strain relationship. If a stress is applied to a polymer and then removed, it takes some time for the stress in the polymer to disappear. The effect is due to a molecular rearrangement in the solid induced by the stress. [2] The time scale for this to occur is called the relaxation time. Additionally, if a small sinusoidal stress is applied to a polymer, the resulting strain is out of phase with the stress by an angle δ. There is an in-phase component representing energy storage and a 90° out-of-phase component representing energy dissipation. The relative extent of each of these effects depends on a dimensionless Deborah number, De given by:

$$De = \frac{\tau}{T_{char}} \tag{1.9}$$

where T_{char} is a characteristic time constant of the process of interest, representing the length of time in which the stress is applied. τ is the relaxation time. [14] For low values of De the polymer response is essentially liquid-like (viscous), whereas for high values it is solid-like (elastic). Viscoelastic behaviour is often modelled by spring and damper systems. Such a model comprising units of a spring and damper in series is called a Maxwell element; a parallel combination is called a Voigt element. [1]

The Crank model

In an attempt to produce a model for non-Fickian behaviour, in 1953 Crank [15] postulated that as penetrant concentration increased in a polymer there was a sudden jump in the diffusion coefficient which slowly drifted back to an equilibrium value. This history-dependent system can be described by Fick's second law with the modification that

$$\frac{\partial D(c,t)}{\partial t} = \frac{D_{eq}(c) - D(c,t)}{\tau(c)}. \tag{1.10}$$

D_{eq} is the equilibrium diffusion coefficient, c is concentration and t is time. Under certain limitations this methodology has successfully described pure Fickian, Case II and anomolous behaviour. [16]

The Thomas and Windle model and the Peppas model

In 1982, Thomas and Windle introduced what has become the basis of the most widely accepted model of Case II ingress. Phenomenologically, Thomas and Windle considered that the swelling of the polymer caused a stress across the sample that relaxed over time. The relaxation process was governed by competition between the viscosity of the polymer decreasing the stress across the sample and more solvent entering the polymer thereby increasing the stress. Mathematically,

$$\frac{\partial c}{\partial t} = \frac{\partial}{\partial x}\left[D\frac{\partial c}{\partial x}\right] + \frac{\partial}{\partial x}\left[\frac{D\bar{V}c}{RT(1-c)(1-2\chi c)}\frac{\partial \sigma}{\partial x}\right] \tag{1.11}$$

and

$$\frac{\partial \sigma}{\partial t} = -\frac{\sigma}{\eta/E} + \frac{E}{(1-c)^2}\frac{\partial c}{\partial t} \tag{1.12}$$

where $\bar{V}$ is the solvent molar volume, R is the universal gas constant, T is temperature, σ is the normal stress in the x direction, E is the Young's modulus of the spring in the Maxwell model, χ is the Flory-Huggins interaction parameter (discussed in Section 1.3.4) and η is the viscosity of the damper in the Maxwell model. Numerical solutions to these differential equations are very unstable due to the fact that, for Case II diffusion, concentration profiles are step functions, with a first derivative of infinity at the front. Hence, application of this model using a simple numerical algorithm given by Thomas and Windle [17] yielded solutions that, in the Case II limit, were dependent on the step size of the finite differences used. [18] A more rigorous approach by Wu and Peppas [19] also seemed promising. They adopted asymmetric finite differences in their approach. However, this unfortunately led to solutions which were dependent on the direction of solvent ingress. To overcome this shortcoming, a symmetric finite difference method, using the ideas of Wu and Peppas, that gives stable and symmetric solutions has been implemented by the group at Surrey. [20] One additional limitation with this model, is that it also requires a large number of unknown parameters.

The Cody and Botto model

The Cody and Botto theory appeared in 1994. [21] They explained that the solvent concentration gradient induces a strain across the sample that relaxes in a time that is dependent on the entangled polymer network. This strain is considered to be that from a single Voigt viscoelastic element. Mathematically, Cody and Botto used Fick's second law with the proviso that:

$$\frac{\partial c}{\partial x} = \Pi J(1 - e^{-\frac{t}{\tau}}) + \left.\frac{\partial c}{\partial x}\right|_{front} \tag{1.13}$$

where J is the compliance (a time-dependent reciprocal Young's modulus or creep term) of the polymer network, Π is the osmotic pressure driving diffusion and $\left.\frac{\partial c}{\partial x}\right|_{front}$ is the solvent concentration gradient evaluated at the rubber/ glass interface.

1.3.4 The thermodynamics of a polymer/ solvent system

To fully describe a polymer being swelled by solvent, not only the kinetics of the system must be considered, but the thermodynamics of the resulting polymer solution must be considered also. The chemical potentials in polymer solutions deviate enormously from those given by Raoult's description of an ideal solution (where the activity of a solvent in solution equals its mole fraction). [6, 22] This comes as no surprise because this law assumes equal molecular sizes and intermolecular attraction between the solute and solvent. The thermodynamics of polymer solvent systems were developed independently by Flory [22] and Huggins [23] in 1942. The level of enthalpic and entropic deviation from Raoult's law can be quantified by the Flory-Huggins interaction parameter, χ. [22] Thermodynamically good solvents interact strongly with polymer molecules. That is, they deviate little from ideality and hence have a small χ (< 0.5). [22] Thermodynamically bad solvents, however, interact very little with polymer molecules; they therefore deviate enormously from ideality and hence have large values for χ (> 0.5). [22] The Flory-Huggins interaction parameter is a function of temperature [24], concentration and molecular weight (even at very high molecular weights). [25] The solvent volume and quality decides which technique is used to measure χ. Suitable apparatus include gas liquid chromotography (for low solvent fractions) and light scattering techniques (for high solvent fractions). [26]

1.4 Why study solvent ingress?

Solvent ingress in polymers has huge importance in both the manufacture and end application of polymers. [27] In manufacturing, topics of interest include the motion of monomer, solvent and plasticizer molecules in polymer. [27] End applications of engineering polymers include controlled drug release [28], microlithography [29], membrane separation [30] and in fibre spinning. [31] Solvent ingress in biopolymers such as water in xanthan is also of considerable interest because of its relevance to the storage of water in plant roots. [32] Today, the controlling mechanisms of solvent ingress are reasonably well understood. However, confusion remains in the literature to describe some crucial phenomena. For instance, the rates of ingress in mixed solvent systems, the effects of polymer molecular weight on solvent ingress, and the mechanisms controlling the transition from Fickian to Case II dynamics are all poorly understood. These issues are all considered in this thesis.

Chapter 2

Experimental methods

2.1 Measuring solvent ingress experimentally

The simplest and most common way to measure solvent ingress is to do a gravimetric experiment (see for instance reference [33]). Specifically, the polymer is placed in the solvent and removed every so often and weighed. This methodology has the problem of all ex-situ experiments in that changes can occur to the sample, such as solvent evaporation, when it is transferred from the solvent reservoir to the weighing apparatus and, of course, one cannot look at the effects of just one of the solvents in a mixed solvent system. Additionally, since there is no spatial concentration information one cannot find the diffusion coefficient as a function of concentration. Other methods that have been used in the literature include ion beam analysis [34], nuclear magnetic resonance (NMR) spectroscopy [35], ellipsometry [36], magnetic resonance imaging (MRI) [27, 37, 38, 39, 40], optical microscopy [41], neutron reflectivity [42] and conductivity measurements. [43] Neutron reflectivity is good for investigating sharp interfaces but is much less sensitive to the broad interfaces we expect in this study. [44] Only the magnetic resonance techniques and ion beam analysis can examine two solvent components separately. However, the ion beam technique requires, that at each ingress time step, the solvent has to be frozen into position and then measured hence a true dynamic in-situ measurement cannot be made. It does have the advantage of very high spatial resolution (suitable for examining the Fickian precursor in a Case II system, for instance). NMR spectroscopy can only take information about the swelling sample as a whole. It cannot provide a solvent concentration profile through the sample. The advantage of MRI is that an image can be taken at any position through the swelling sample. The disadvantage of MRI is that spatial and temporal resolution are both relatively low. The temporal and spatial resolution of optical microscopy is very high. However, separate solvent components in a mixed solvent system cannot be individually resolved. Ellipsometry seems the better technique in these applications. Although it cannot easily differentiate between separate solvent types, spatial and temporal resolution are extremely high, and information through the sample can sometimes be obtained (it is difficult for ellipsometry to provide a concentration profile). In the work explained in this thesis, the techniques of magnetic resonance imaging and ellipsometry are used to measure solvent ingress into polymers.

2.2 Nuclear magnetic resonance

2.2.1 The NMR development timeline

The first successful attempts to observe NMR absorption were reported in 1946 by Purcell *et al* at Stanford and by Bloch *et al* at MIT. Purcell's group detected the NMR of protons in paraffin whereas Bloch's group detected the NMR of protons in water. The first major application of NMR became apparent after the discovery of the chemical shift phenomenon in 1950 and its use in spectroscopy quickly became commonplace. Lauterbur, working with liquids, reported the first reconstruction of a proton spin density map in 1973. In the same year, Mansfield and Grannell, working with solids, independently showed the Fourier relationship between the spin density and the NMR signal. MRI is now routinely performed in hospitals. The application of MRI in materials science has only relatively recently started to develop. One of the more notable achievements, for the study of solids and confined liquids, has been stray field imaging suggested by Samoilenko in 1988. A chronology of the development of NMR over the last fifty years is given in Table 2.1.

2.2.2 The NMR phenomenon

Atomic nuclei are characterised by quantum mechanical states. At a macroscopic level the behaviour of nuclei are combined as an ensemble. For nuclei with spin quantum number $I = 1/2$ (a description of this term is given below), these spins are conventionally described by two orientations of a single vector: "up" or "down". This forms the basis for the classical description of NMR, the approach taken by Felix Bloch. It is described in Section 2.2.5. The semi-classical approach for any I, followed by Purcell, is explained next in Section 2.2.3.

2.2.3 The semi-classical energy level approach to NMR

Atomic nuclei are spinning charges. They therefore have an angular momentum or spin **I**. This gives rise to a magnetic moment **m**. We can write

$$\mathbf{m} = \gamma \mathbf{I}. \tag{2.1}$$

γ is usually called the gyromagnetic ratio although more correctly it should be termed the magnetogyric ratio. The value of γ is nuclei specific. Spin is quantised

Table 2.1: A chronology of the development of NMR

1946	Bloch [45] and Purcell [46] independently reported the first successful NMR absorption experiments in condensed matter.
1948	Relaxation described theoretically by Bloembergen, Purcell and Pound (BPP theory). [47]
1950	Chemical shift effect discovered highlighting NMRs use in chemical applications. [48, 49]
	Hahn proposed the use of spin echoes to rephase transverse magnetisation. [50]
1952	Noble prize in physics shared by Bloch and Purcell for their contribution to NMR.
1953	First commercial NMR spectrometer.
1966	Ernst proposed the use of pulsed Fourier spectroscopy rather than continuous wave spectroscopy. [51, 52]
1973	Lauterbur suggested the use of magnetic field gradients to make proton resonant frequencies position dependent. [53]
	Mansfield and Grannell introduced the concept of **k**-space. [54]
1978	First commercial MRI scanner.
1986	First NMR micrographs (voxels smaller than $100\mu m^3$). [55, 56, 57, 58]
1988	Samoilenko proposed stray field imaging. [59]
1991	The Noble prize in chemistry won by Ernst for his contribution to NMR.

with quantum number I such that

$$|\mathbf{I}| = \hbar\sqrt{I(I+1)}. \tag{2.2}$$

$\hbar$ is Planck's constant.* If the magnitude of **I** is known, then, because of the uncertainty principle, the orientation is incompletely specified and only the magnitude in one direction can be known. Having applied a magnetic field the measurement direction is defined. In NMR, it is conventional to use the z axis. Now the z component of the angular momentum is defined as

$$I_z = |\mathbf{I}|\cos\beta = m_L\hbar, \tag{2.3}$$

where $m_L = \pm I, \pm(I-1), \ldots$ and β is the angle of the spin to the z axis. m_L is called the magnetic quantum number. For spin-half systems, i.e. $I = 1/2$, we can rearrange Equation 2.3 to find that $\beta = 54.7°$. The interaction energy E between a magnetic dipole and a magnetic field **B** is

$$E = -\mathbf{m}\cdot\mathbf{B}. \tag{2.4}$$

Assuming that there is a magnetic field in the z direction we can substitute Equations 2.1 and 2.3 into Equation 2.4. This gives the result for the energy of the states as

$$E = -\gamma\hbar m_L B_0. \tag{2.5}$$

Conventionally, in NMR, the magnetic field in the z direction is called the B_0 field. The energy difference between the two possible states of a spin-half system

---

*The fact that the angular momentum of particles is quantised is usually attributed to Bohr. However in 1912, the year before Bohr, the Englishman John Nicholson was really the first to make the discovery. Unfortunately, at this time, Rutherford's model of the atom was not complete, and thus Nicholson's results, using an incorrect model for the atom, were somewhat modest. Nicholson felt that he never received proper recognition for his discovery and he died in obscurity in 1955.

$(m_L = \pm 1/2)$ is written as

$$\Delta E = \gamma \hbar B_0. \tag{2.6}$$

Transition between energy states requires a quantum of energy

$$\Delta E = \hbar \omega. \tag{2.7}$$

Comparing Equations 2.6 and 2.7 we can finally write

$$\omega_0 = \gamma B_0. \tag{2.8}$$

This is the Larmor equation and ω_0 is called the Larmor frequency. If $I \geq 1$, then more than one transition is possible, and in the presence of perturbing interactions, these nuclei may have more than one Larmor frequency. For $I = 1/2$ systems, if a spin has $m_L = +1/2$ it is called a spin-up; if $m_L = -1/2$ then it is a spin-down.

2.2.4 The bulk nuclear magnetisation

The possible energy levels have a thermal equilibrium population given by a Boltzmann distribution. For $m_L = \pm 1/2$ we can say that the distribution of the spins in the two energy states is

$$\frac{n_\uparrow}{n_\downarrow} = e^{\frac{-\Delta E}{kT}} = e^{\frac{-\gamma \hbar B_0}{kT}}, \tag{2.9}$$

where $n_\uparrow$ is the number of spin-ups per unit volume, $n_\downarrow$ is the number of spin-downs per unit volume, T is temperature and k is the Boltzmann constant. We can write that the net magnetisation or magnetic moment per unit volume M is

$$M = (n_\uparrow - n_\downarrow) m. \tag{2.10}$$

Trivially, $n_\uparrow + n_\downarrow = n$ where n is the total number of spin-half nuclei. Combining Equations 2.9 and 2.10 we can write that

$$M = n \tanh\left(\frac{\gamma\hbar B_0}{2kT}\right). \tag{2.11}$$

For a typical proton NMR experiment at the University of Surrey: $B_0 = 9.4$ T, $T = 298$ K and $\gamma = 2.7 \times 10^8$ rad s $^{-1}$ T^{-1}. Hence, $n_\uparrow - n_\downarrow \approx 33 \times 10^{-6}$. For a proton NMR experiment we only get a signal from 33 out of every million nuclei. Additionally, every emitted quantum of energy from a downward transition is tiny ($\hbar\omega_0$). An NMR experiment has an inherently low signal.

2.2.5 The classical approach

The Bloch equations

A nucleus spinning in a magnetic field feels a torque

$$\mathbf{T} = \mathbf{m} \times \mathbf{B}. \tag{2.12}$$

The torque is also equal to the change in angular momentum

$$\mathbf{T} = \frac{d\mathbf{I}}{dt}. \tag{2.13}$$

Equating the two expressions for torque and substituting Equation 2.1 we see that

$$\frac{d\mathbf{m}}{dt} = \gamma(\mathbf{m} \times \mathbf{B}). \tag{2.14}$$

Hence, for an ensemble of spins

$$\frac{d\mathbf{M}}{dt} = \gamma(\mathbf{M} \times \mathbf{B}). \tag{2.15}$$

The steady state solution is precession at an angle β about the field direction with angular velocity $\omega_0 = -\gamma B_0$ such that:

$$M_z = M_0 \cos\beta, \tag{2.16}$$

$$M_x = M_0 \sin\beta \cos\omega_0 t, \tag{2.17}$$

$$M_x = M_0 \sin\beta \sin\omega_0 t. \tag{2.18}$$

When a sample is placed in a magnetic field B_0 the magnetic moment changes from zero to M_0. Equally when the orientation of the equilibrium magnetisation in the magnetic field is perturbed and then released the magnetisation returns to M_0. Bloch assumed that M relaxes to M_0 exponentially and that the components of M parallel and perpendicular to M_0 relax with different time constants T_1 and T_2 respectively. With the z axis chosen along B_0

$$\frac{dM_z}{dt} = -\frac{M_z - M_0}{T_1}, \tag{2.19}$$

$$\frac{dM_x}{dt} = -\frac{M_x}{T_2}, \tag{2.20}$$

$$\frac{dM_y}{dt} = -\frac{M_y}{T_2}. \tag{2.21}$$

This approach to thermal equilibrium is known as relaxation and T_1 and T_2 are relaxation times. The decay of M_z, the longitudinal component can differ from the decay of the transverse components M_x and M_y because the energy of the system depends on M_z. A change in M_z is accompanied by an energy flow between the nuclear spin system and the surrounding lattice of atoms. The relaxation time describing this flow is T_1, usually known as the spin-lattice relaxation time. For protons, at room temperature, typical values are between 0.01 and 10 s. Direct interactions between the spins of different nuclei can cause relaxation M_x and

M_y without energy transfer to the lattice. Hence T_2 is known as the spin-spin relaxation time. Typical values for T_2 are between 10 μs and 10 s for protons at room temperature. [60]

In an NMR experiment a small oscillating magnetic field in the x direction $2B_1 \cos \omega t$ is used to perturb the magnetisation and excite observable resonance phenomena. It can be resolved into two components that precess in opposite directions around B_0 one of which can be ignored as it is effectively off-resonance by $2\omega_0$ when $\omega_0 \approx \omega$. The total field $\mathbf{B}$ acting on the sample is

$$\mathbf{B} = B_1 \cos \omega t \mathbf{i} - B_1 \sin \omega t \mathbf{j} + B_0 \mathbf{k} \tag{2.22}$$

where $\mathbf{i}$, $\mathbf{j}$ and $\mathbf{k}$ are unit vectors in the x, y and z directions. Combining Equations 2.15, 2.19, 2.20, 2.21 and 2.22 and we can write the Bloch equations in the presence of this perturbing field and relaxation as [60]:

$$\frac{dM_z}{dt} = -\gamma(B_1 \cos \omega t M_y + B_1 \sin \omega t M_x) - \frac{(M_z - M_0)}{T_1}, \tag{2.23}$$

$$\frac{dM_y}{dt} = -\gamma(B_0 M_x - B_1 \cos \omega t M_z) - \frac{M_y}{T_2}, \tag{2.24}$$

$$\frac{dM_x}{dt} = \gamma(B_1 \sin \omega t M_z + B_0 M_y) - \frac{M_x}{T_2}. \tag{2.25}$$

The rotating reference frame

The Bloch equations can be made simpler by considering a set of axes (x', y', z) rotating with the applied field with angular velocity $-\omega$ about the z axis. If u is the component of magnetisation in the B_1 direction (along x') and v is the component along the y' axis then:

$$u = M_x \cos \omega t - M_y \sin \omega t, \tag{2.26}$$

$$v = M_x \sin \omega t + M_y \cos \omega t. \tag{2.27}$$

In the rotating frame the Bloch equations are written as [60]:

$$\frac{dM_z}{dt} = -\gamma B_1 v - \frac{(M_z - M_0)}{T_1}, \tag{2.28}$$

$$\frac{du}{dt} = (\omega_0 - \omega)v - \frac{u}{T_2}, \tag{2.29}$$

$$\frac{dv}{dt} = -(\omega_0 - \omega)u + \gamma B_1 M_z - \frac{v}{T_2}, \tag{2.30}$$

which clearly simplify further when the resonance condition $\omega = \omega_0$ is met.

2.2.6 Radio frequency pulses

In a real sample each spinning nucleus will be in a different chemical environment. The causes of these differences are described in Section 2.2.8. The differences in environment produce different resonant conditions. NMR can be used to determine these differences and it is this fact that makes NMR such a powerful method for finding the structure of molecules. The simplest way to obtain an NMR spectrum is to slowly sweep a single radio frequency (RF) to scan all the resonances in a sample. This is called continuous-wave (CW) NMR. One disadvantage with this method is that, since one is only detecting one frequency at a time, an experiment can be very slow. To overcome this shortcoming short pulses of radiation are used. In a pulsed experiment an oscillating RF magnetic field is turned on for a time usually in the range of 1-50μs (i.e. short compared to the relaxation times). The frequency (called the carrier frequency ω_c) of this pulse is chosen so that it is close to the resonance of the nucleus of interest. If one Fourier transforms this time-domain top-hat function one has a sinc function in the frequency domain centred on ω_c, that is to say, a range of frequencies are now excited. One can see the action of the pulse best in the rotating frame. In the rotating reference frame M will precess about the x' axis at $-\gamma B_1$ during the pulse. After a pulse of length τ it will have precessed by $\gamma B_1\tau$. If $\tau = \pi/2\gamma B_1$ then M will have turned through 90° into the y' direction (a so called 90° pulse). If $\tau = \pi/\gamma B_1$ then after the pulse M will be in the $-z$ direction (a 180° pulse). Following a pulse, Boltzmann equilibrium is restored by relaxation. After a 180° pulse there is purely spin-lattice relaxation:

$$M_z(t) - M_0 = (M_z(0) - M_0)\exp(-t/T_1). \tag{2.31}$$

This is a solution to Equation 2.19. A 90° pulse is followed by transverse relaxation:

$$M_y(t) = M_y(0)\exp(-t/T_2). \tag{2.32}$$

This is a solution to Equation 2.21 as well as spin-lattice relaxation.

2.2.7 Signal detection

To measure the NMR phenomenon in the laboratory, a coil must be placed around the sample. The coil geometry should be such that the symmetry axis is perpendicular to the B_0 field. Any transverse magnetisation precessing at ω_0 will induce an EMF at the same frequency in the coil. In an RF receiver the induced EMF in the coil is mixed with a reference RF oscillator at a frequency, ω_r. This is called heterodyning. If two RF references are used that are 90° out of phase, then the output signal is proportional to orthogonal magnetisation phases i.e. M_x and M_y. Hence, in the time domain, the NMR signal is represented as a decaying EMF, oscillating at $\Delta\omega = \omega_0 - \omega_r$. As an example of an expected NMR signal, consider an experiment where an RF pulse is applied that flips the equilibrated spins at $M_0\mathbf{k}$ through 90°. In the laboratory frame of reference and neglecting T_1 relaxation, the magnetisation is then

$$M(t) = (M_0 \cos\omega_0 t\mathbf{i} + M_0 \sin\omega_0 t\mathbf{j})e^{-\frac{t}{T_2}}. \tag{2.33}$$

Expressing this in complex number notation where **i** is the real axis and **j** is the imaginary axis we have that

$$M(t) = M_0 e^{i\omega_0 t} e^{-\frac{t}{T_2}}. \tag{2.34}$$

The heterodyne signal is

$$S(t) = S_0 e^{i\phi} e^{i\Delta\omega t} e^{-\frac{t}{T_2}}. \tag{2.35}$$

S_0, the signal immediately after the RF pulse is proportional to M_0 and ϕ is the absolute receiver phase. Since this EMF is induced by the magnetisation in free precession, it is called a free induction decay (FID). There is a Fourier relationship between the FID and the spectrum measured by CW NMR.

2.2.8 Linewidths and interactions

Linewidth

For a liquid state sample, if we Fourier transform the NMR signal and set the absolute receiver phase to 0°, then we see a Lorentzian in the real channel with a full-width-half-maximum (FWHM), or linewidth, of $1/\pi T_2$ (the absorption spectrum) and what is called a dispersion spectrum in the imaginary channel. These spectra are illustrated in Figure 2.1.

Magnetic field inhomogeneity

In a real NMR magnet, inhomogeneities in the B_0 field, expressed as ΔB_0, are inevitable. In the frequency domain, this leads to a broadening of the NMR spectrum and in the time domain, this gives a more rapid transverse dephasing than T_2 effects alone would suggest. The time constant that represents this is

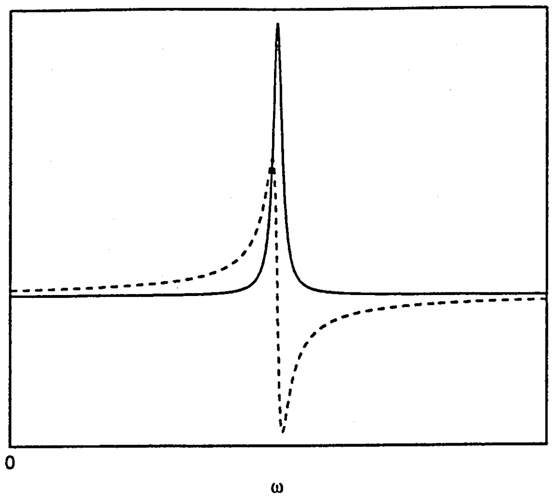

Figure 2.1: The absorption spectrum in the real channel (solid line) and the dispersion spectrum in the imaginary channel (dashed line).

T_2^*. It can be written as

$$\frac{1}{T_2^*} \approx \frac{1}{T_2} + \frac{\gamma \Delta B_0}{2}. \tag{2.36}$$

It should be noted that although coherence lost through relaxation is random and therefore irreversible, coherence lost through magnetic field inhomogeneities is ordered and thus reversible. This is achieved in a two pulse sequence by the formation of a Hahn echo. [50] The first pulse excites and the second pulse refocuses.

Dipole interactions

Given that the separation of nuclei in condensed matter is relatively vast, it is surprising to see that the magnetic fields from spinning nuclei have a massive influence on their neighbours. These effects are called dipole interactions. They have the same magnitude between the nuclei of solids and liquids, but in liquids they are averaged to zero by the motion of the constituent nuclei. Hence, in solids, T_2 is extremely short and the signal can be broadened so much in the frequency domain that the NMR signal can be invisible. Due to the ordered nature of dipole interactions, the FID is Gaussian in shape.

Chemical shift

In condensed matter, the atomic nuclei are surrounded by a cloud of electrons. The field generated from these electrons acts against the B_0 field and we can write

$$B_{nucleus} = B_0(1 - \sigma) \tag{2.37}$$

where σ is called the shielding parameter. This equation means that spins that are in different electronic environments – and therefore in different magnetic fields – precess at different angular velocities. The absolute value of σ is hard to find, so the shift in frequency, the so-called chemical shift δ, from a reference frequency f_{ref} is measured instead, with

$$\delta = \left(\frac{f - f_{ref}}{f_{ref}}\right) \times 10^6 \tag{2.38}$$

where f is the frequency of the compound of interest. The chemical shift is dimensionless, and we describe the shift in parts per million or ppm. It is no overstatement to proclaim that the discovery of the chemical shift phenomenon in the 1950s revolutionised chemistry.

Scalar coupling

Scalar, spin-spin or J-coupling (since it is quantified by the coupling constant J), acts through electrons in chemical bonding and not through space. A nucleus perturbs its bonding electrons, which produces a magnetic field at a neighbouring nucleus, which, in turn, affects its neighbouring nuclei and so on. The value of J is independent of spectrometer frequency, and for protons typical values are rarely above 20Hz. [61]

Quadrupolar coupling

Nuclei with $I > 1/2$ have an electric quadrupole moment that arises from the non-spherical distribution of nuclear charge. These nuclei interact with electric field gradients that are produced by valence electrons. This type of interaction gives $2I$ lines in low symmetry environments. In liquids it is averaged to zero. When $I > 1/2$, the quadrupolar interaction dominates relaxation.

2.2.9 Measuring relaxation times

Measuring T_1

In an experiment after a 180° Equation 2.31 applies but no signal is detected because no magnetisation is produced in the y direction. However, at any time after the pulse the state of M_z can be monitored by applying a 90° pulse. The pulse sequence used is

$$[180^\circ \; - \; \tau \; - \; 90^\circ(\mathrm{FID}) \; - \; T_d]_n \tag{2.39}$$

where T_d is a time longer than the longest T_1 to be measured so that a return to the Boltzmann populations is made between 180° pulses. The FID is Fourier transformed and the time τ is varied. T_1 is then found from a plot of $\ln S$ against τ (S is the peak height at each τ) using:

$$\ln(S(\infty) - S(t)) = \ln(2) + \ln S(\infty) - \tau/T_1. \tag{2.40}$$

Spin-echoes and T_2 measurement

Two factors contribute to the FID after a 90° pulse. Due to magnetic field inhomogeneities, different parts of the same specimen have different Larmor frequencies and so the different contributions to the magnetisation vector slowly fan out. Random processes realign the nuclei to establish thermal equilibrium. These processes can be measured separately by using a series of pulses and observing spin-echoes. A 90° pulse turns M_0 into the y-axis (Equation 2.32). The magnetisation vectors then fan out and the signal decays. A 180°_y pulse is then applied after time τ i.e. all magnetisation vectors are rotated by 180° about y'. The magnetisation vectors continue to move in the same direction and after τ they are again in-phase in the y' direction. This is a spin-echo or Hahn echo. Successive 180°_y pulses can be applied and the amplitude of the resulting echoes decays exponentially due to T_2 relaxation. The value of T_2 can be found from the envelope of the echoes. This is the Carr-Purcell-Meiboom-Gill (CPMG) sequence.

2.2.10 The theory of relaxation

The requirement for spin-lattice relaxation is the presence of a magnetic field fluctuating on a time scale comparable to the Larmor frequency. Such fluctuations give rise to the energy quanta necessary to cause spin transitions. An essentially static or low frequency fluctuation is required for T_2 relaxation. The fluctuations experienced by a nucleus in a liquid $f(t)$ where t is time will be due to the magnetic moments of other nuclei as they move through Brownian motion. This fluctuating field can be resolved into two components perpendicular and parallel to B_0. The component perpendicular to B_0 induces transitions between energy levels, in a similar way to electromagnetic radiation. This gives a non-adiabatic contribution to both T_1 and T_2 relaxation. The populations of the states change until they reach the values given by the Boltzmann distribution (Equation 2.9). This process is entirely described by T_1. T_2, on the other hand, also has an adiabatic component. The linewidth (if B_0 effects are neglected) is inversely proportional to T_2 and is a measure of the uncertainties in the energies of the two states. Through the Heisenberg principle this is found to be inversely proportional to the lifetime of the states. These are reduced by random fluctuations in the local magnetic field. Hence fluctuation in the magnetic field affects both T_1 and T_2. Both the x and y components of the fluctuating field affect T_1. However, M_y is affected only by the x component of the non-adiabatic term, hence the non-adiabatic contribution to T_2^{-1} is half that of T_1^{-1} for mobile liquids. The adiabatic contribution to T_2^{-1} is from the magnetic field fluctuations in the z direction which affect linewidth. For a mobile liquid this contribution is $T_1^{-1}/2$ so $T_1 = T_2$.

The fluctuation in the x-component of the local magnetic field is:

$$B_x(t) = B_{0_x} f(t). \tag{2.41}$$

We need to quantify the persistence of these fluctuations. This is done using an autocorrelation function defined as:

$$G(\tau) = \overline{f(t)f(t+\tau)}. \tag{2.42}$$

The bar shows that this is an ensemble average over all the spins in a region of space. τ is the time over which the ensemble is averaged. $G(\tau)$ is independent of t but decays with τ. This decay can be assumed to be exponential and we can write that:

$$G(\tau) = \exp(-|\tau|/\tau_c). \tag{2.43}$$

τ_c is called the correlation time. From perturbation theory [60] we can write that:

$$\frac{1}{T_1} = \gamma^2 B_{0_x}^2 J(\omega_0). \tag{2.44}$$

$J(\omega_0)$ is the spectral density i.e. the power available from fluctuations at frequency ω. It is the Fourier transform of $G(\tau)$. Hence, using the assumption of Equation 2.43:

$$J(\omega) = \frac{2\tau_c}{1+\omega^2\tau_c^2}. \tag{2.45}$$

Substituting Equation 2.45 into Equation 2.44 gives:

$$\frac{1}{T_1} = \gamma^2 B_{0_x}^2 \frac{2\tau_c}{1+\omega_0^2\tau_c^2}. \tag{2.46}$$

Plots of $J(\omega)$ against $\log(\omega)$ are shown in Figure 2.2. The flat part of the graphs occurs when $\omega^2\tau_c^2 \ll 1$. This is called extreme narrowing. In this case:

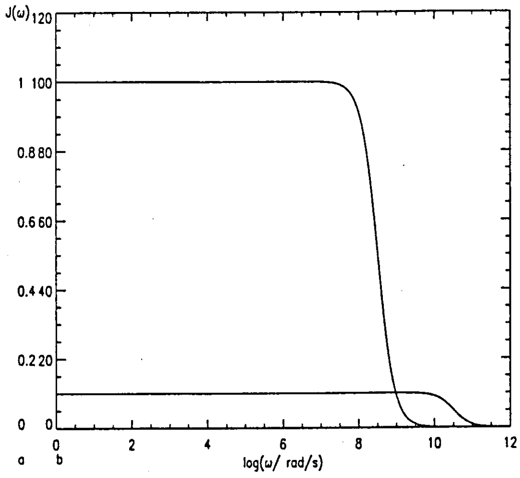

Figure 2.2: A graph of $J(\omega)$ (with arbitrary units) against ω. Case (a) shown by the left hand scale and lower plot shows the extreme narrowing situation when $\tau_c = 10\sqrt{10}$ps valid for mobile systems. Case (b) shown by the right hand scale and the upper plot is far from extreme narrowing ($\tau_c = 10\sqrt{10}$ns) valid for immobile systems

$$\frac{1}{T_1} = 2\gamma^2 B_{0_x}^2 \tau_c. \tag{2.47}$$

In mobile solutions, $\tau_c \sim 10$ps and since for an NMR experiment ω is of the order of 10^8rads^{-1} the extreme narrowing condition holds and hence T_1 increases with τ_c, that is, as mobility decreases. Away from extreme narrowing the full form of Equation 2.46 holds. Its form is plotted in Figure 2.3. For T_2 the adiabatic term, discussed above, requires no energy change hence the appropriate spectral density is $J(0)$. We can write:

$$\frac{1}{T_2} = \frac{1}{2T_1} + \frac{\gamma^2 B_{0_z}^2 J(0)}{2}. \tag{2.48}$$

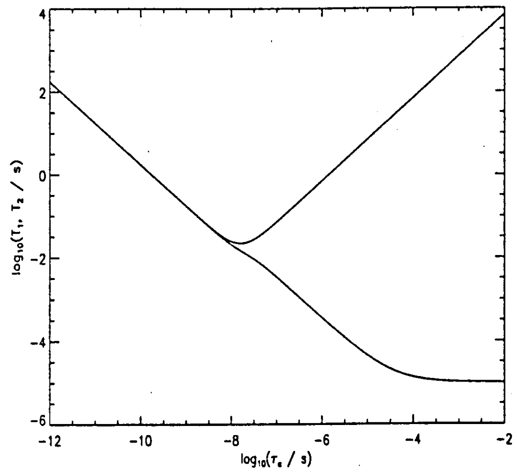

Figure 2.3: A graph of T_1 ('V'-shaped curve) and T_2 (lower curve) versus the correlation time τ_c. The left hand side of the graph is the extreme narrowing regime

Figure 2.3 shows the form of this equation. The concepts in this section were first described by Bloembergen, Purcell and Pound [47] and are usually called BPP theory. They are valid in the so called "weak collision"case when $\tau_c < T_2$ In Figure 2.3 the rigid lattice value of T_2, when $\tau_c \rightarrow \infty$ and BPP theory is not valid, has been arbitrarily chosen as it depends on the distribution of the random fields. [60]

2.3 Magnetic resonance imaging

Consider two spins in a B_0 field to which a magnetic field gradient $\frac{\partial B_z}{\partial x} = G$ has been additionally applied. One of the spins has an angular frequency $\omega(x)$. The other spin a distance Δx away has angular frequency, $\omega(x+\Delta x) = \omega(x)+\gamma G \Delta x$. The difference in frequency between the two spins is therefore $\gamma G \Delta x$. Hence we see that frequency maps to space. The constant of proportionality linking frequency and space is the product of the known terms γ and G. In theory this allows us to find NMR parameters such as nuclei density, T_1 and T_2 as a function of position and not simply an average of the whole, bulk sample. This concept is the basis for magnetic resonance imaging (MRI). How this technique works in practise is described below.

2.3.1 k-space

For simplicity we again consider spins in one-dimension at position x. The spins occupy an element dx and the local spin density is $\rho(x)$. Hence, in an element there are $\rho(x)dx$ spins. These nuclei are in a fixed magnetic field to which a magnetic field gradient has also been applied. From Equation 2.35 we can write that the signal from this element dS is

$$dS(G,t) \propto \rho(x)e^{i\omega(x)t}dx. \tag{2.49}$$

Substituting for $\omega(x)$, we have

$$dS(G,t) \propto \rho(x)e^{i(\gamma B_0+\gamma Gx)t}dx. \tag{2.50}$$

If the on-resonance condition applies (that is the heterodyne reference signal ω_r is set to γB_0), then the signal oscillates with γGx only. So, after integration

$$S(G,t) \propto \int \rho(x)e^{i\gamma Gxt}dx. \tag{2.51}$$

With a change of variables such that $k = \frac{\gamma Gt}{2\pi}$ and neglecting the constant of proportionality

$$S(G,t) = \int \rho(x)e^{i2\pi kx}dx. \tag{2.52}$$

This equation is of course a Fourier transform. Taking the inverse of this means that we can write the spin density as:

$$\rho(x) = \int S(G,t)e^{-i2\pi kx}dk. \tag{2.53}$$

Trivially extending these arguments to three-dimensional space (where the spins are at the cartesian position $\mathbf{r}$):

$$S(\mathbf{k}) = \int\int\int \rho(\mathbf{k}) e^{i2\pi\mathbf{k}\cdot\mathbf{r}} d\mathbf{r}, \tag{2.54}$$

$$\rho(\mathbf{r}) = \int\int\int S(\mathbf{k}) e^{-2\pi\mathbf{k}\cdot\mathbf{r}} d\mathbf{k}. \tag{2.55}$$

This statement of three-dimensional **k**-space giving the mutual conjugacy between S and ρ is the fundamental relationship of MRI. **k** has the units of reciprocal space or m^{-1}. However, normally only two dimensions are encoded in this way and slice selection is used to image three dimensional space.

2.3.2 MRI pulse sequences

The aim of an MRI experiment is to acquire enough information about **k**-space to be able to produce an image in space with a desired contrast weighting. This contrast weighting can come from a wide range of physical factors, such as T_1, T_2, nuclei density, chemical composition, diffusion or flow. It is this huge range of different contrast media that makes MRI such a powerful technique. Different contrast and different views of **k**-space are found by using pulse sequences. These are combinations of RF pulses and switched magnetic field gradients. A careful – and often extremely cunning – choice of these inputs can produce an image with the desired contrast and sample slice selection. In this section a description is given first of spin-warp imaging, its drawbacks are discussed and then the spin-echo imaging sequence is described. The latter is the most commonly used pulse sequence for magnetic resonance microscopy.

2.3.3 Spin-warp imaging

The spin warp pulse sequence is shown in Figure 2.4. In MRI we usually want

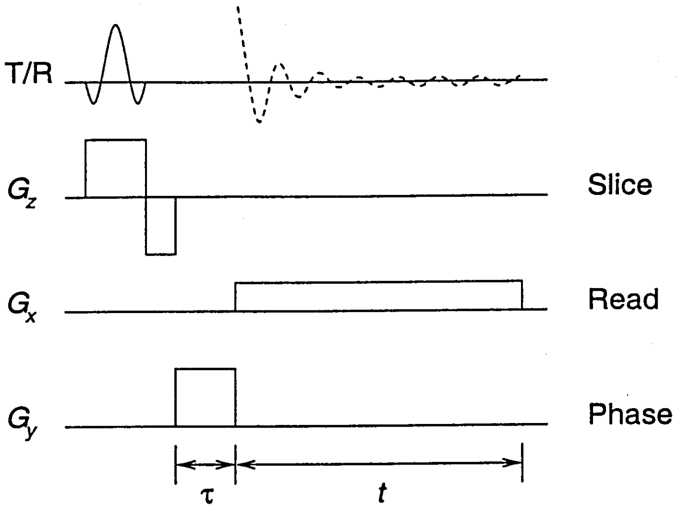

Figure 2.4: The spin-warp pulse sequence. On the top line, the RF transmit (T) signal is shown as the solid line; the received signal (R) is shown as a dashed line. The sequence is repeated many times with τ incremented at each stage.

to record a 2D image, i.e., a slice through a 3D sample. So first we must select a 2D slice. This is achieved by applying a magnetic field gradient in the z direction and then applying a frequency-selective and therefore, because of the magnetic field gradient, a slice-selective (or soft) 90° RF pulse. Ideally, a soft pulse should be rectangular in the frequency domain. However, this is a sinc function in the time domain, which expands infinitely in time. Hence, in practise, it will always be truncated, producing unwanted modulation in the frequency domain. Nevertheless, sinc pulses with three or five lobes are usually good enough. Soft pulses are also often Gaussian in the time domain and therefore Gaussian in the frequency domain, which is an acceptable approximation to a rectangular, frequency domain pulse. The first order phase shift introduced by the soft pulse must be refocused. This is done by reversing the slice gradient for a time equal to half the pulse length. Another gradient is now applied in the y direction, the so called phase direction. This gradient causes the spins to rotate at different rates so after a time τ they each have a different phase, hence the name of this axis. The spins now precess at a frequency dependent only on their y position, hence their phase ϕ also depends only on this position as:

$$\phi(y) = \omega(y)\tau = -\gamma y G_y \tau. \tag{2.56}$$

Acquisition of the signal now begins at the same time as a further gradient in the x direction is switched on. The spins now precess at a rate dependent on their x position:

$$\omega(x) = -\gamma x G_x. \tag{2.57}$$

The signal from each spin is now:

$$dS(x, y, t) = e^{i\phi(y)} e^{i\omega(x)t} \rho(x, y) dx dy. \tag{2.58}$$

Integrating over the whole sample gives

$$S(x, y, t, \tau) = \int_{-\infty}^{\infty} \int_{-\infty}^{\infty} e^{-\gamma x G_x t} e^{-\gamma y G_y \tau} \rho(x, y) dx dy. \tag{2.59}$$

Performing a change of variables, we can write Equation 2.59 as

$$S(x, y, t, \tau) = \int_{-\infty}^{\infty} \int_{-\infty}^{\infty} e^{-x k_x} e^{-y k_y} \rho(x, y) dx dy. \tag{2.60}$$

This is of course the Fourier transform of $\rho(x, y)$. So inverse transforming returns the spin density $\rho(x, y)$. Additionally, one should note that for a single acquisition period described above we obtain values for a range of t but only one τ value. The sequence is therefore repeated for a range of different τ values. To produce a full representation of $\rho(x, y)$ we need to measure as much of **k**-space as possible. One problem with the spin-warp sequence is that, because we cannot make an acquisition in negative time, it is not possible to measure k_x and k_y for negative values. This leaves a huge portion of **k**-space unknown. A second drawback with this sequence is that the NMR signal decays because of inevitable B_0 inhomogeneities.

2.3.4 Spin-echo imaging

Both of the problems with the spin-warp sequence are overcome with the addition of a second application of a magnetic field gradient in the read direction and a 180° RF pulse. A schematic of the timing of the complete spin-echo sequence is shown in Figure 2.5. To measure negative k_x a negative phase is introduced to the spins before acquisition. This is done by using a read-dephase gradient lobe. A gradient is applied during the period τ so that the spins are phased. The 180° pulse then inverts these spins. The read gradient is applied again and as t evolves we measure increasing k_x from negative, through zero, to positive. The 180° pulse also refocuses magnetisation that has been dephased by B_0 inhomogeneities. This increases the measured signal compared to spin-warp imaging. To measure negative k_y, gradient G_y is incremented every T_R to go from negative to positive rather than changing τ, which cannot be negative. The other advantage in not incrementing τ is that the relaxation weighting remains constant across the sample. If T_R is less than between three and five times the value of T_1, then the level of T_1 contrast is changed. If the echo time is in the

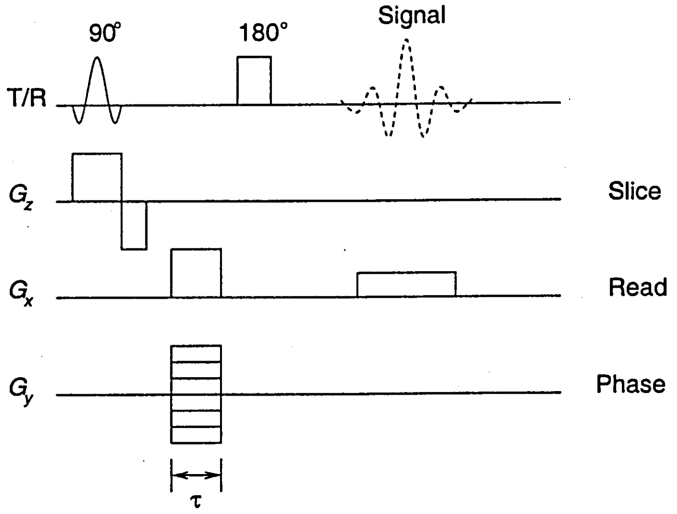

Figure 2.5: The spin-echo pulse sequence. On the top line, the RF transmit (T) signal is shown as the solid line; the received signal (R) is shown as a dashed line.

region of T_2 then an image has T_2 contrast. An alternative to spin-echo imaging is gradient-echo imaging. Here, an echo appears without applying a 180° RF pulse because the magnetisation is refocused by reversing the first read gradient pulse. This sequence, however, gives T_2^* weighting rather than the T_2 weighting of spin-echo imaging, but the minimum echo time is shorter without the 180° pulse.

2.3.5 Spatial resolution

We cannot, of course, measure our NMR signal at an infinite rate. Neither can we measure it for an infinite time. This means that a magnetic resonance image has a finite resolution and field of view. The level of the digital resolution can easily be explained by rearranging our definition of 1D k-space, say k_x, and writing Δk_x as the increment in k_x-space we measure, Δx is the space between image pixels, Δt is the time between samples of the NMR signal and N is the number of samples in total time T. This gives

$$\Delta x = \frac{2\pi}{N\Delta k_x} = \frac{2\pi}{N\gamma G_x \Delta t} = \frac{2\pi}{\gamma G_x T}. \tag{2.61}$$

We can assume that features are resolved across next nearest neighbour pixels so that spatial resolution is

$$\Delta r_{best} = 2\Delta x. \tag{2.62}$$

Our lines in frequency space are not of course infinitely small but are broadened (Section 2.2.8) with FWHM $1/\pi T_2$ so there is a limit on T such that after scaling the line broadening by $2\pi/\gamma G_x$

$$\frac{1}{\pi T_2} = \frac{1}{T}. \tag{2.63}$$

Hence,

$$\Delta r_{best} = \frac{4}{\gamma G_x T_2}. \tag{2.64}$$

This argument is of course valid in all three dimensions. [62] Spatial resolution is also limited by diffusion. This attenuates the signal as: $\exp(-\gamma^2 G_x^2 t^3 D/3)$ giving $\Delta r_{best} \approx 2.6[D/(\gamma G_x)]^{1/3}$. [63] Other phenomena that limit resolution are susceptibility inhomogeneity and spin motion. [64] Solids have very short T_2s. This makes them a challenge to image with MRI.

2.3.6 Stray field imaging

One way to improve spatial resolution is to maximise the magnetic field gradient. In conventional MRI, gradient coils are used to produce this gradient and a typical maximum obtainable value for a microimaging set is between 1 and 10Tm^{-1}. [62] In 1988 Samoilenko *et al* [59] [65], proposed placing the probed sample in the fringe field of a superconducting magnet. It is well known that a magnetic field reduces as the reciprocal of the distance squared. However, this gradient can only be approximated as linear over short distances and it is not switchable. Nevertheless, huge magnetic field gradients, roughly linear over short distances, are obtainable. At the University of Surrey, our superconducting magnet with an isocentre field of 9.4T can can give a near linear gradient of 58Tm^{-1} in a 5.5T fringe field. In a conventional stray field imaging (STRAFI) experiment, a profile is acquired by using an RF pulse to excite the resonating spins. The high gradient ensures that even a short pulse is highly spatially selective. The resulting magnetisation is recorded directly as a measure of the spin density in the resonance plane. A Fourier transformation is not required. Instead, the sample is then moved mechanically so that a different slice of the sample is then at the position in the field corresponding to the coil resonant frequency. Usually only 1D profiles are obtained although it is possible to move the sample in all three dimensions and construct an image using back projection type algorithms. In 1992, Miller and Garroway [66] proposed frequency swept imaging. In this technique, the excitation frequency is incremented rather than the position of the sample. This is a relatively fast method but it has the disadvantage that the field of view can be rather small (say 2mm). It is limited by the bandwidth of the RF coil and the sensitivity of the coil at a distance. The latter is usually the ultimate limiting factor. Both STRAFI acquisition methodologies, however, have one great advantage over conventional MRI. Since time is not spent switching gradients, measurements can be made close to the pulse before T_2 decay has occured and so true proton density maps can be obtained. It should also be noted that with such a large gradient, T_2^* is short, usually much less than the dead time of the spectrometer, hence no FID can be measured. Instead, the signal must be refocussed as an echo. Usually, a quadrature echo sequence that generates an echo train is used such as $90_x - \tau - (90_y - \tau - \text{echo} - \tau)_\text{n}$ where τ is the time period between RF pulses and n is the number of echoes. [67] This sequence has the advantage of producing spin-relaxation weighted profiles. Alternatively, if the SNR is low, the echoes can be summed.

2.3.7 MRI hardware

In a conventional system magnetic field inhomogeneity in the magnet is critical. Values of the order of one part in 10^7 are required. This is achieved by putting an additional set of adjustable magnetic field coils or shims inside the fixed B_0 magnet. The shims are computer controlled and their values can be optimised by the NMR experimenter. The gradient pulses are also computer controlled. The signal from the computer is first passed through a digital to analogue converter and then amplified to drive the gradients in all three dimensions. The RF pulses are controlled by the computer modulating the output from an RF generator at the desired Larmor frequency. These pulses are then passed through an amplifier.

A typical broadcast power is 1kW. The RF signal is both transmitted and received by the same coil. The received signal is passed through a pre-amplifier which amplifies the signal from the order of μV to a level more suitable for further amplification. If different nuclei are probed with the same spectrometer, then a range of frequencies need to be amplified. The usual balance between bandwidth and signal-to-noise ratio that results is, in our case, dealt with by using a broadband pre-amplifier. However, the signal is first passed through a filter to remove any signal out of the frequency range of interest. This signal then needs to be fed back to the computer for processing. However, analogue to digital converters do not work at RF frequencies so the signal is first demodulated, that is the NMR signal is removed from the Larmor frequency carrier. A demodulator works by mixing the NMR signal $S(t) = f(t)e^{i(\omega_0+\Delta\omega)t}$ with a reference signal $\cos\omega_0 t$. This gives

$$S(t)\cos\omega_0 t = \frac{f(t)}{2}[\cos(2\omega_0 + \Delta)t + \cos\Delta\omega t + i(\sin(2\omega_0 + \Delta\omega t)]. \tag{2.65}$$

We can simplify this expression to

$$S(t)\cos\omega_0 t = \frac{f(t)}{2}(e^{i(2\omega_0+\Delta\omega)t} + e^{i\Delta\omega t}). \tag{2.66}$$

The signal now has two frequency components. The high one is removed with a low pass filter to leave the low frequency component, which yields the NMR frequency with respect to the rotating frame of reference. This low frequency component can then be digitised. [68]

2.3.8 RF coil design for isocentre MRI

There are a number of designs for coils that provide a homogeneous RF field perpendicular to the B_0 field. Usually these coils have a circular cross section to house a sample test tube. The solenoidal coil provides the greatest SNR.

However, a normal superconducting magnet, suitable for MR microscopy, has a narrow bore and so housing a sample test tube within this bore can be awkward. Consequently, saddle [69] or birdcage [70] type coils are used. [64] A saddle coil has an SNR of about one-third of that of a solenoid [71], however, they provide a more convenient sample geometry. Hoult and Richards [71] show that the optimal geometry for both homogeneity and proximity is given by a coil length twice that of the coil diameter. For the saddle coil the optimum angular width is 120°.

2.3.9 Chemically selective imaging

One advantage of MRI over other techniques for measuring mixed solvent ingress is that one can probe specific chemical species. There are a number of different methodologies for doing this.

Chemical substitution

In a mixed solvent system, such as methyl ethyl ketone and ethanol ingressing polystyrene, to be looked at later, we may want to look at just one solvent at a time. To observe ethanol only, for instance, we can substitute deuterium atoms for some hydrogen atoms in the ethanol only and perform an MRI experiment at the deuterium Larmor frequency. Alternatively, one can perform an additional ^{1}H experiment on the same system and deduce ingress information from the signal that has disappeared from the signal of the fully-protonated system. This has the advantage of having a better SNR and hence quicker experiment time. The disadvantage is that signal from the increasingly mobile rubber cannot be easily deducted without performing an experiment where all the ingressing solvents have been isotopically substituted, to give signal only from the polymer. However, with any type of labelling experiment, there will always be the worry that the labelled molecules behave differently from their unlabelled counterparts. Sometimes the effect is major, in the case where fluorine is used for labelling, if acetone (a liquid) is fluorinated it becomes perfluoroacetone (a gas) and cyclohexane (a liquid) becomes perfluorocyclohexane (a solid). [72] Indeed, even when the atomic species remains the same after labelling, e.g. deuterium instead of hydrogen, the diffusion coefficient varies with mass.

Relaxation time editing

Different chemical species display different relaxation times. Hence, editing an image based on the relaxation time of each species would appear to be very convenient. The problem with this type of method for mixed solvent ingress experiments is that there will be a spread of relaxation times across the sample depending on the relative concentrations of each of the solvent components. This means that accurate nulling of the response from either of the solvent components across the whole sample would be very difficult. [72]

Chemically resolved imaging

If the NMR spectrum of a mixed solvent reservoir has more than one line with a separation greater than a single pixel, each line will produce an image displaced by its respective chemical shift. There are a number of NMR techniques available that allow one to obtain separate images from each resonance. The easiest method is to make one of the excitation pulses a soft pulse, applied in the absence of gradients and then to use the other pulse for slice selection. There are other techniques where a fourth spectral dimension is introduced such as chemical-shift imaging. [73] Here, all spatial dimensions are phase encoded and the NMR signal is acquired without a magnetic field gradient. The result is an NMR spectrum at each point in **k**-space. The disadvantage of chemically resolved imaging is that if chemical shifts are small between species, then unambiguous distinction between them is not possible. Also, with the addition of a spectral dimension to the MRI experiment, measurement time can become prohibitively high [74] for in-situ solvent ingress experiments.

Cyclic *J* cross polarisation edited imaging

Another alternative is cyclic *J* cross polarisation (CYCLCROP) edited imaging which exploits the wider chemical shift of ^{13}C with respect to ^{1}H whilst still retaining the SNR advantages of ^{1}H imaging. The pulse sequence consists of two modules: one for editing and the other for imaging. The editing sequence selects a single resonance from a specific $^{13}CH_n$ group of a molecule while suppressing all other resonances. The output is an FID. A suitable imaging sequence, such as a spin-echo, can then be implemented. The sequence has already been successfuly implemented by Kimmich and coworkers [75] and used to study carbohydrate metabolism and transport [76] and to selectively determine elastomer distribution in multicomponent polymer mixtures. [77] The CYCLCROP editing sequence is shown in Figure 2.6. It consists of a forward step ^{1}H → ^{13}C, a saturation step during which unwanted signal is destroyed, and a backward ^{13}C → ^{1}H

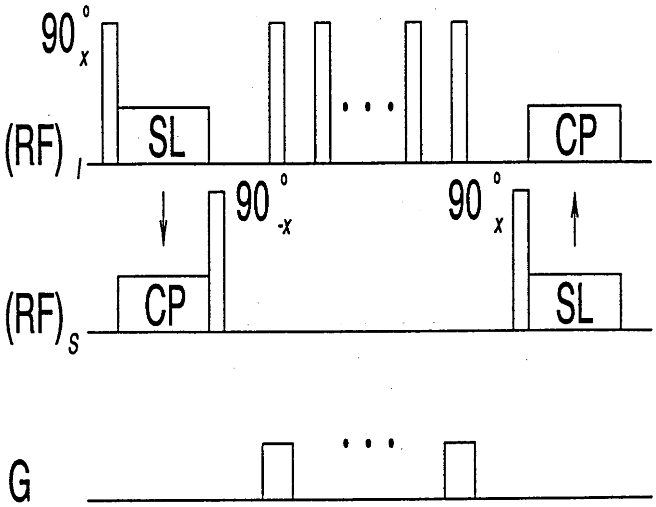

Figure 2.6: The CYCLCROP pulse sequence

polarisation transfer step. The forward and backwards steps are both composed of a spin-locking pulse (SL) on one side and a contact pulse (CP) on the other. Magnetisation is said to be spin-locked when after a 90°_x pulse, the B_1 field is not switched off but its phase is shifted by 90° so that it is aligned with the magnetisation along the $+y$ axis for a time τ. In the rotating frame of reference, the magnetisation only experiences the B_1 field and undergoes no precession. It does, however, decay with a time constant $T_{1\rho}$ (the spin-lattice relaxation time in the rotating frame). Spin-locking is the preparation mode used in the Hartmann-Hann experiment. [78] This allows magnetisation transfer from NMR favourable spins (high γ and/ or abundance) in this case ^{1}H to NMR unfavourable spins (low γ and/ or abundance) in this case ^{13}C. In a two-spin system, one set, I can be locked along an RF field B_1 (the spin-locking pulse) and another, S along a second RF field B_2 (the contact pulse). If the Hartmann-Hann condition

$$\gamma_I B_1 = \gamma_S B_2 \tag{2.67}$$

is satisfied, then coherence can be transferred between the two chemical species. In solid state systems, I and S spins interact through dipolar interactions. In liquids, indirect spin-spin or J coupling prevails. This is also called J cross polarisation. In the CYCLCROP sequence, magnetisation is first transferred from the ^{1}H to the ^{13}C spins. The carbon magnetisation is then stored in the z direction. All residual proton spin resonances are saturated with a combination of spoiler gradient pulses and a comb of RF pulses at the proton spin resonance. The ^{13}C spins are then spin-locked and the polarisation transferred back to the J coupled protons. Another module, for instance a spin-echo imaging sequence, can then be deployed. The polarisation transfer for the ^{13}CH$_n$ system of interest only occurs if the Hartmann-Hann condition holds for that methyl group. In a CYCLCROP experiment, the RF frequencies of the ^{1}H and ^{13}C channels are set to the resonant frequencies of the nuclei one wants to observe. The optimum duration for the SL and CP pulses for the most complete transfer of magnetisation depends on the value of the spin-spin coupling constant J and the number of protons in the probed molecular group. [76] The efficiency of the transfer of magnetisation discussed above is highly susceptible to inaccurate adjustment in the RF amplitude and to sample inhomogeneity. To minimise any Hartmann-Hann mismatch effects various modifications have been proposed including MOIST [79] and PRAWN. [80] The latter uses a train of m pulses with flip angle α of duration τ_w separated by a delay τ_s. The α pulses must satisfy the condition $m\alpha = 2\pi$ and $\tau = m(\tau_w + \tau_s)$. PRAWN has the advantage of requiring low RF powers, increased efficiency and it is both adaptable for a variety of applications and easy to implement.

2.4 Ellipsometry

Ellipsometry has been around for more than 30 years. It is an optical technique and as such is non-invasive if the sample is not light sensitive. Under good experimental conditions, a measurement of refractive index can be returned to the nearest 0.001 and the thickness of a layer to the nearest Å. In an ellipsometry experiment, light in a known polarisation state is reflected from a planar sample surface or parallel interfaces. The state of polarisation after reflection is then measured and used to deduce characteristics of the sample.

2.4.1 What is polarised light?

For a non-conducting, non-dispersive medium any propagating light must obey Maxwell's equations. [81] These equations can be combined to give the wave equation for the electric field of the propagating light beam

$$\nabla^2\mathrm{E} - \frac{\epsilon\mu}{c^2}\frac{\partial^2\mathrm{E}}{\partial t^2} = 0. \tag{2.68}$$

A solution to this is the electromagnetic plane wave

$$\mathbf{E}(\mathbf{r},t) = \mathbf{E}_0 e^{\frac{i2\pi N}{\lambda}\mathbf{q}\cdot\mathbf{r}} e^{-i\omega t}. \tag{2.69}$$

$\mathbf{E}$ is the electric field, c is the speed of light, ϵ is the dielectric function, μ is the permeability, $\mathbf{E}_0$ is a complex vector constant specifying the amplitude and polarisation state of the wave, $N = n + ik$ the complex refractive index, λ is the wavelength of the light, $\mathbf{q}$ is a unit vector along the direction of wave propagation and $\mathbf{r}$ defines a Cartesian coordinate system. If there is no absorption, that is $k = 0$, such a wave will propagate indefinitely with the electric field, magnetic field and direction of travel all orthogonal to each other. Hence, the E-field and the propagation direction are all that are needed to define a plane wave. If k is non-zero, then the amplitude of the wave decays exponentially with propagation distance. If you look at linearly polarised light where the direction of travel is out of the page (in the z direction) then the electric field vibrates back and forth tracing a line at all times. That is, the x and y components of the E-field, E_x and E_y, are in phase. If E_x and E_y are equal in magnitude but 90° out of phase, then the light is called circularly polarised because, if the light travels out of the paper, the E-field vector traces out a circle as a function of time. If, E_x and E_y do not have equal magnitudes and and have a phase relationship not equal to 90°, the E-field vector traces out an ellipse, and the light is elliptically polarised.

2.4.2 The ellipsometry experiment

In a typical experiment, linearly or circularly polarised light is reflected from a sample. After reflection the light becomes elliptically polarised, hence the name ellipsometry. The change in amplitude and phase of the polarised light are determined both in the plane of reflection (p-plane or parallel plane) and perpendicular to this plane (the s-plane or *senkrecht* plane, the German word for perpendicular). Before reflection, the light has a polarisation state given by the amplitude ratio $\frac{A_p}{A_s}$ and phase difference $d_p - d_s$. The two ellipsometry angles ψ and Δ are then given by

$$\Delta = (d_p^r - d_s^r) - (d_p^i - d_s^i), \tag{2.70}$$

and

$$\tan\psi = \frac{A_p^r/A_s^r}{A_p^i/A_s^i}. \tag{2.71}$$

The subscripts p and s, refer to the two orthogonal planes. A superscripted i indicates the incident wave and a superscripted r is a reflected wave. ψ and Δ are related to the Fresnel reflection coefficients R_p and R_s by the so-called ellipticity given by

$$\rho = \frac{R_p}{R_s} = \tan\psi e^{i\Delta}. \tag{2.72}$$

This equation is particularly useful as it relates the polarisation state to the physical parameters of the sample, namely the refractive indices and thicknesses of the sample layers via the Fresnel coefficients.

2.4.3 The Fresnel equations

For m layers on a semi-infinite substrate, we can write the Fresnel reflection coefficients using a convenient matrix system. [82] First recall Snell's law [81]

$$N_0 \sin\phi_0 = N_1 \sin\phi_1 = \ldots = N_j sin\phi_j = \ldots = N_{m+1} \sin\phi_{m+1}. \tag{2.73}$$

N_j is the refractive index of the jth layer and ϕ_j is the angle between the angle of propagation in the jth layer and the perpendicular to the plane of the layer's interfaces. N_0 is the ambient refractive index. If the jth layer has thickness d_j, then the Fresnel reflection coefficients are

$$R_p = \frac{S_{21p}}{S_{11p}}, \tag{2.74}$$

$$R_s = \frac{S_{21s}}{S_{11s}} \tag{2.75}$$

where

$$\mathbf{S}_{p,s} = \begin{bmatrix} S_{11p,s} & S_{12p,s} \\ S_{21p,s} & S_{22p,s} \end{bmatrix}. \tag{2.76}$$

$\mathbf{S}_{p,s}$ is given by

$$\mathbf{S}_{p,s} = \mathbf{I}_{01p,s}\mathbf{L}_1\mathbf{I}_{12p,s}\mathbf{L}_2 \ldots \mathbf{I}_{j(j-1)p,s}\mathbf{L}_j \ldots \mathbf{L}_m\mathbf{I}_{m(m-1)p,s} \tag{2.77}$$

where

$$\mathbf{I}_{abp,s} = \begin{bmatrix} \frac{1}{t_{ab}} & \frac{r_{ab}}{t_{ab}} \\ \frac{r_{ab}}{t_{ab}} & \frac{1}{t_{ab}} \end{bmatrix}, \tag{2.78}$$

$$\mathbf{L}_a = \begin{bmatrix} e^{i\beta_a} & 0 \\ 0 & e^{-i\beta_a} \end{bmatrix}, \tag{2.79}$$

and

$$\beta_a = \left(\frac{2\pi d_a N_a}{\lambda}\right) \cos\phi_a. \tag{2.80}$$

r_{ab} is the amplitude reflection coefficient at the interface between substance a and b and t_{ab} is the amplitude transmission coefficient of the ab interface. By convention, the ambient medium is called medium 0 and the substrate is given the highest number. The reflection and transmission coefficients are expressed by

$$r_{ab} = \frac{v_a - v_b}{v_a + v_b}, \tag{2.81}$$

and

$$t_{ab} = \frac{2v_a}{v_a + v_b}, \tag{2.82}$$

where for the s-polarised component,

$$v_a = N_a \cos \phi_a, \tag{2.83}$$

and for the p-polarised component,

$$v_a = \frac{N_a}{\cos \phi_a}. \tag{2.84}$$

Other expressions can be included to incorporate such features as surface roughness and anisotropic refractive indices. [83]

2.4.4 Ellipsometry data collection and inversion strategies

To extract useful N_j and D_j information from ellipsometry data (ψ and Δ) the Fresnel equations must be inverted. Drolet *et al* [84] state that so far, this has been done analytically only for six simple cases when one or two (ψ, Δ) pairs are found to find one or two unknowns, such as finding the complex refractive index of a single layer on a known substrate. To analyse more complicated sample structures, this inversion can sometimes be enabled by acquiring (ψ, Δ) pairs at different values of ϕ_0 and λ so that sufficient simultaneous equations are formed to solve for all the unknown variables. One should add at this point that since each refractive index has two unknown components (the real and imaginary parts respectively) that are both functions of incident wavelength each additional (ψ, Δ) pair found from an extra spectroscopic scan merely produces another *two* unknowns. For polymers (where $k = 0$) this problem is solved by using the well known Cauchy dispersion model [81]

$$N_j(\lambda) = na_j + \frac{nb_j}{\lambda} + \frac{nc_j}{\lambda^4} + \dots. \tag{2.85}$$

Usually the terms in λ^4 and higher are so small that they are neglected resulting in only two unknowns needing to be found to characterise a polymer refractive index at any wavelength. One final note on this subject is to consider the effects of changing ϕ_0. We get more information from different ϕ_0s if the path length of the light beam is changed as a result. This does not happen when there are no layers on a substrate, when the layers are very thin, or if the refractive index is very high ($N > 3$) such as for semiconductor samples. As it was just stated, with many unknowns the Fresnel equations cannot be inverted analytically. In commercial ellipsometers the data are analysed instead by entering some realistic initial guess values and then using a Levenberg-Marquardt least-squares fitting algorithm (LM) [85] to minimise the error between the experimental data and the simulated data generated from the Fresnel equations. This works both accurately and quickly if the measured sample structure is already well known. However, if the sample structure is quite complicated, say $m > 2$, and the structure of the sample is unknown, LM can be extremely difficult to use. The reason for this is that ellipsometry data is inherently ambiguous. For instance, sets of ψ and Δ data cannot be inverted to necessarily differentiate between two layers p and q of different refractive indices and thicknesses on a substrate arranged p on q or q on p. Although experimentalists know of this ambiguity, as far as we are aware, thorough quantification of it has never been made. The two issues of inverting ellipsometry data for an arbitrary refractive index profile and assessing the ambiguity inherent in ellipsometry data to produce a more robust fitting methodology for unknown samples are both considered in Chapter 5.

2.4.5 The sensitivity of ellipsometry

In Figure 2.7 one can see a demonstration of the sensitivity of ellipsometry for simulated noise-free data. The Δ curve for a Cauchy semi-infinite substrate ($na = 1.5$ and $nb = 0$) is a step function. ψ is a smooth V-shaped curve. The discontinuity in Δ occurs when $\psi = 0°$ and at a specific angle-of-incidence called the Brewster angle. If a 100Å thick Cauchy layer with a refractive index of

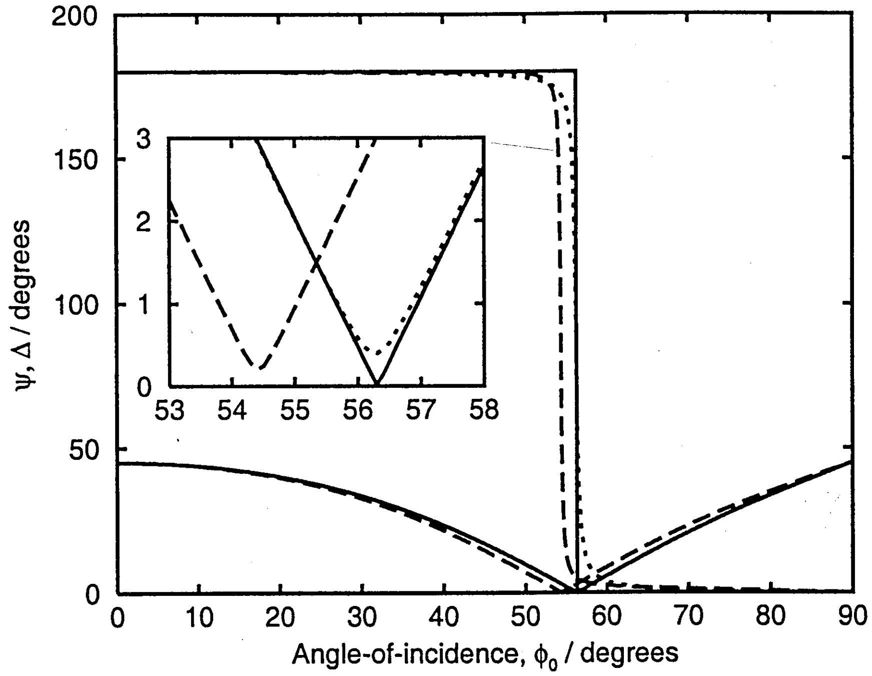

Figure 2.7: Simulated ellipsometry ψ and Δ data at various angles of incident light. The Δ data is at the top, the ψ data is at the bottom. The solid line shows a single semi-infinite Cauchy layer substrate with $na = 1.5$ and $nb = 0$; the dotted line shows the same substrate with a 100Å thick Cauchy layer on top with $na = 1.45$ and $nb = 0$; the dashed line show the same substrate but with a 1000Å thick Cauchy layer on top with $na = 1.45$ and $nb = 0$. The inset shows only ψ to demonstrate the change in ψ at the Brewster angle.

$na = 1.45$ and $nb = 0$ is placed on top of this substrate, then some curvature can be seen in the Δ plot, and refering to the inset of the graph ψ no longer goes to zero at the Brewster angle. With a thicker, 1000Å layer, with the same refractive index parameters as before, on top of the substrate then a noticeable shift is seen in both ψ and Δ. The largest changes occur around the Brewster angle. For a single, fast (2s) scan, typical of those used in a solvent ingress experiment, the ellipsometer at Surrey can produce precisions of ±0.15° in ψ and ±1.5° in Δ. [86]

2.4.6 Ellipsometry hardware

How does the ellipsometer return values of ψ and Δ? An ellipsometer has the following elements: light source $\longrightarrow$ polarisation generator $\longrightarrow$ sample surface $\longrightarrow$ analyser $\longrightarrow$ detector. There are three types of ellipsometer: 1. the null ellipsometer, 2. the phase modulated ellipsometer and 3. the rotating element ellipsometer. The first option is often manually operated and hence very slow. They are therefore not an option for the fast dynamics involved in a solvent ingress experiment. It is also difficult to perform spectroscopic scans with this type of ellipsometer. Phase modulated ellipsometers are extremely fast, however they are extremely sensitive to temperature and so it is difficult to find stable spectral calibrations for them. The third type are ideal for accurate measurements over a broad wavelength range. At the University of Surrey we have a variable angle spectroscopic ellipsometer (VASE) (J. A. Woollam Co., Inc., Lincoln, Nebraska, USA) that uses a rotating-analyser. We briefly consider here each of the elements in this type of ellipsometer. [87]

2.4.7 VASE at the University of Surrey

The monochromated light source

The perfect light source would have an output intensity that is completely constant with time and the same output at every wavelength. This ideal source does not exist. We use a xenon source that is a fair match for these criteria. The flaw is low intensity in the far ultra violet (below 260nm) and high intensity in the infra red (880 to 1010nm). The white light is passed through a monochromator that uses a set of moveable gratings to produce interference patterns that constructively interfere at a selected wavelength. The monochromated light is passed through a mechanical chopper that modulates the light so that ambient light at the same wavelength but modulated at a different frequency can be rejected later. The light travels up an optical fibre where it is then passed through a collimating lens before being linearly polarised using a calcite Glan-Taylor polariser. This beam is reflected off the sample that has previously been carefully aligned. The reflected beam then goes into a rotating analyser, which is described in the next section.

The rotating analyser: obtaining ψ and Δ from polarised light

The rotating analyser is a rotating linear polariser with a photo-detector behind it. It provides a measure of how the light is now polarised. How does this component work? Figure 2.8 shows the voltage $V(t)$ that is produced from the photo-detector behind the rotating analyser with elliptically-polarised incident light. This voltage has the general form

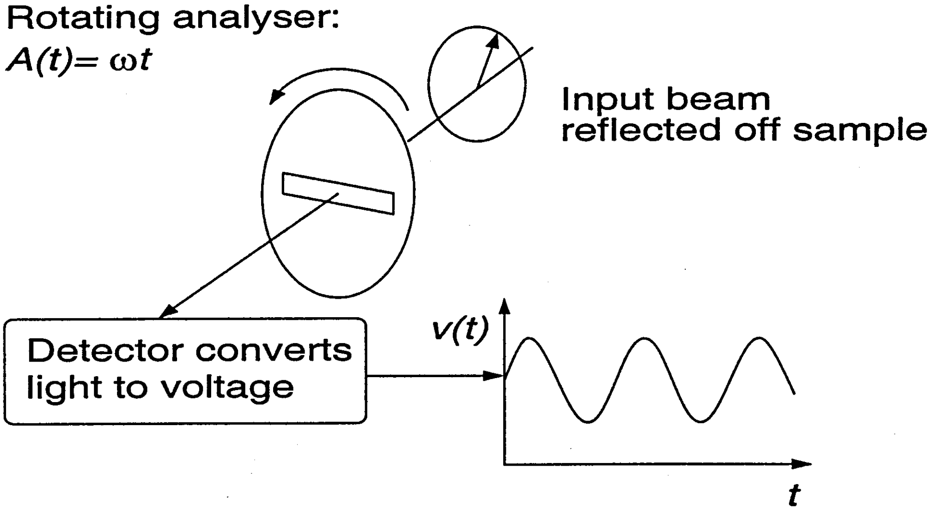

Figure 2.8: The detector signal associated with an elliptically polarised beam entering the rotating analyser polarisation detector

$$V(t) = d + a\cos(2\omega t) + b\sin(2\omega t) \tag{2.86}$$

where a, b and d are constants for each characteristic polarisation state, ω is the angular velocity of the rotating analyser, and t is time. $V(t)$ oscillates in magnitude as the analyser sweeps through angles of rotation. How this voltage is related to ψ and Δ is best described using Jones vectors and matrices. In this system an electric field $\mathbf{E}$ is described as components of p-polaristaion E_p and s-polarisation E_s such that

$$\mathbf{E} = \begin{bmatrix} E_p \\ E_s \end{bmatrix}. \tag{2.87}$$

With this notation any effect by a component on the polarisation state can be written as a 2 × 2 transfer matrix. These are called Jones matrices. The electric field at the detector E_d will then be given by

$$E_d = [\text{analyser matrix}][\text{sample matrix}][\text{polariser matrix}][\text{input beam}]. \tag{2.88}$$

The detector intensity I_d and thus voltage is proportional to $|E_d|^2$. All we need to do now is write Jones matrices for each of the optical components in the ellipsometer. To make things simple we consider a rotated coordinate system such that the axis of the input polariser is in the p-direction. Rotating the cordinate system back to the p and s system of the ellipsometer, we can write that the beam incident on the sample is

$$\begin{bmatrix} \cos P & -\sin P \\ \sin P & \cos P \end{bmatrix} \cdot \begin{bmatrix} 1 \\ 0 \end{bmatrix} \tag{2.89}$$

where P is the angle between the polariser axis and the plane of incidence. Assuming that the sample is isotropic and smooth, then there are no off-diagonal elements in the sample Jones matrix. It is simply

$$\begin{bmatrix} R_p & 0 \\ 0 & R_s \end{bmatrix}. \tag{2.90}$$

It should be noted that anisotropic samples are sometimes of interest. If this is the case, then the off-diagonal elements of the Jones matrix must be considered. With respect to the analyser frame of reference, where the angle between the analyser and the plane of incidence of the light is A, the Jones matrix for the analyser is then

$$\begin{bmatrix} 1 & 0 \\ 0 & 0 \end{bmatrix} \cdot \begin{bmatrix} \cos A & \sin A \\ -\sin A & \cos A \end{bmatrix}. \tag{2.91}$$

Combining all these expressions as indicated in Equation 2.88 gives

$$E_d = \begin{bmatrix} 1 & 0 \\ 0 & 0 \end{bmatrix} \cdot \begin{bmatrix} \cos A & \sin A \\ -\sin A & \cos A \end{bmatrix} \cdot \begin{bmatrix} R_p & 0 \\ 0 & R_s \end{bmatrix} \cdot \begin{bmatrix} \cos P & -\sin P \\ \sin P & \cos P \end{bmatrix} \cdot \begin{bmatrix} 1 \\ 0 \end{bmatrix} \tag{2.92}$$

Evaluating this expression and we have

$$E_d = \begin{bmatrix} R_p \cos P \cos A + R_s \sin P \sin A \\ 0 \end{bmatrix}. \tag{2.93}$$

The intensity of the beam is then the non-zero element of E_d multiplied by its complex conjugate. We can use a few trigonometric identities and then normalise the expression by dividing through by the term that is independent of the analyser angle. The result is that

$$I_d \propto 1 + \frac{\left|\frac{R_p}{R_s}\right|^2 - \tan^2 P}{\left|\frac{R_p}{R_s}\right|^2 + \tan^2 P} \cos 2A + \frac{2\Re\left(\frac{R_p}{R_s}\right) \tan P}{\left|\frac{R_p}{R_s}\right|^2 + \tan^2 P} \sin 2A. \tag{2.94}$$

$\Re$ indicates the real part of an expression. Substituting in Equation 2.72 gives an expression effectively relating ψ and Δ to the electric signal from the detector:

$$I_d \propto 1 + \frac{\tan^2 \psi - \tan^2 P}{\tan^2 \psi + \tan^2 P} \cos 2A + \frac{2 \tan \psi \cos \Delta \tan P}{\tan^2 \psi + \tan^2 P} \sin 2A. \tag{2.95}$$

Divide Equation 2.86 by its DC component d and then compare this to Equation 2.95 and we can see that

$$\frac{a}{d} = \alpha = \frac{\tan^2 \psi - \tan^2 P}{\tan^2 \psi + \tan^2 P} \tag{2.96}$$

$$\frac{b}{d} = \beta = \frac{2 \tan \psi \cos \Delta \tan P}{\tan^2 \psi + \tan^2 P}. \tag{2.97}$$

Finally, solving these two simultaneous equations in terms of ψ and Δ yields

$$\tan\psi = \sqrt{\frac{1+\alpha}{1-\alpha}}|\tan P| \tag{2.98}$$

$$\cos\Delta = \frac{\beta}{\sqrt{1-\alpha^2}}\frac{\tan P}{|\tan P|}. \tag{2.99}$$

Thus from knowledge, in advance, of P, and measurement of a, b and d the ellipsometry parameters ψ and Δ are obtained.

Calibrating the rotating analyser ellipsometer

Before performing an experiment on an unknown sample, the ellipsometer must be calibrated to find the difference in angle between the dial reading of the polariser (P) and analyser(A) and the true angle between the polariser and analyser and the plane of incidence. We define P_s and A_s as calibration parameters between the true and dial angle measurements of the polariser and analyser, respectively. The relative attenuation of the AC signal, with respect to the DC component of the detector, due to the signal processing electronics must also be calibrated. The calibration parameter η is used to represent this attenuation. We can then write that

$$\alpha = \frac{1}{\eta}[\alpha' \cos 2A_s - \beta' \sin 2A_s] \tag{2.100}$$

and

$$\beta = \frac{1}{\eta}[\alpha' \sin 2A_s + \beta' \cos 2A_s] \tag{2.101}$$

where

$$\alpha' = \frac{\tan^2\psi - \tan^2(P-P_s)}{\tan^2\psi + \tan^2(P-P_s)} \tag{2.102}$$

$$\beta' = \frac{2\tan\psi\cos\Delta\tan(P-P_s)}{\tan^2\psi+\tan^2(P-P_s)}. \tag{2.103}$$

To calibrate the ellipsometer first a smooth, isotropic sample must be mounted and aligned. Typically a silicon wafer with a 20nm thermal oxide layer is used. This will give a well defined polarisation state. The Fourier coefficients, α and β, are then measured as P is changed. Equations 2.100 to 2.103 are then fitted to the measured Fourier coefficients and to the residual function to find the three calibration parameters (P_s, A_s and η).

Chapter 3

Fickian ingress of binary solvent mixtures into glassy polymer

3.1 Introduction

In everyday situations, polymers are often exposed to mixtures of solvents. Typical examples are polymer composites in aircraft or cars being exposed to petroleum/ water mixtures and dental resins being exposed to mixtures of water and ethanol or other solvents in the mouth. The resulting ingress is of obvious importance. The manufacturing of the important industrial product of asymmetric membranes relies on the mass transfer of good and bad solvents in glassy polymer. Either a solvent/ non-solvent/ polymer ternary mixture or a polymer/ solvent binary mixture is exposed to a coagulation bath of non-solvent. Precipitation times have been shown to be dependent on the ternary diffusion coefficients. [88] It has been highlighted in the literature [89] that the diffusivity of a binary solvent mixture cannot be considered to be the additive sum of its components when they differ in molecular volumes and polarities.

The ingress of binary solvents has been measured experimentally by a large number of groups. However, the literature is very confused. There are two schools of thought regarding mixed thermodynamically good/ kinetically bad and thermodynamically bad/ kinetically good solvents ingressing polymer.* They are that only the thermodynamically good solvent ingresses; the thermodynamically bad solvent does not ingress at all. The second way of thinking is that the kinetically good solvent ingresses *ahead* of the kinetically bad solvent. In addition, when both the solvents are thermodynamically good but kinetically different, the two trains of thought continue. Some experimenters hypothesise that the kinetically better solvent leads; others suggest that the solvents ingress at the same rate. All these ideas are discussed below.

3.1.1 Literature summary of binary mixed thermodynamically good and bad solvents

Only the thermodynamically good solvent ingresses

In 1954, Long and Thompson [90], using a gravimetric method [91], found that the ingress rate of polystyrene by water and benzene vapours was only very slightly less than the ingress rate of benzene alone. They concluded that since the water does not ingress alone into the polymer, then it also does not ingress even when mixed with a good solvent for the polymer. Kwei and Zupko [92] used optical methods to measure bicomponent solvent ingress into crosslinked glassy epoxy polymers. For the diffusion of methanol (a thermodynamically bad/ kinetically good solvent) and MEK (a thermodynamically good/ kinetically bad solvent), they found that there was a single advancing front and that it progressed with Fickian dynamics. However, using these techniques no unambiguous visualisation

---

*A thermodynamically good solvent has a value of χ (the polymer-solvent Flory-Huggins interaction parameter) that is less than 0.5. A kinetically good solvent is a physically small molecule.

of the individual solvent component concentrations through the swelling sample could be made. Titow *et al* [93] assumed that Kwei and Zupko's work showed that the bad solvent does not interfere with the "active" solvent (in their words) but correctly speaking no such inference can be made. Miller *et al* [94] looked at the solvent stress-cracking of polycarbonate. They diffused a mixture of isopropanol (a non-stress cracking agent) with varying proportions of various stress-cracking agents (acetone, toluene, benzene, xylene and carbon tetrachloride) and saw that only the stress-cracking agent was sorbed. These experiments used gas chromatographic techniques. Webb and Hall studied Fickian diffusion of two solvents in rubbery polymers using NMR techniques. [95] In one experiment [72], vulcanised rubber (VR) was placed in a reservoir containing a 1:1 mixture of water and acetone. An NMR spectrum was taken of the sample after two weeks. It showed that only acetone had ingressed the polymer. No water signal at all was evident. A further experiment was performed with pure acetone. The signal in the rubber was greater after the same time period when compared to the bicomponent experiment. This indicated that the acetone ingress rate was reduced in the mixed solvent system. Pure water ingresses VR several orders of magnitude slower than acetone [96, 97], much slower than one would expect from the consideration of physical size alone. Webb and Hall suggest that hydrophilic sites within the rubber act as a sink for water molecules and prevent further diffusion into the VR of any solvent. Models have been written with the assumption that for a mixture of water and organic solvent in contact with polymer, only the organic solvent and not the water ingress the polymer. [98] Some researchers have used this assumption but they have presented no unambiguous evidence to prove that water is excluded from the polymer phase. [99]

The kinetically good solvent ingresses ahead of the kinetically bad solvent

In 1968, Ueberreiter [100] stated that some kinetically good but thermodynamically poor solvents may penetrate a polymer matrix at a much faster rate than thermodynamically good but kinetically poor solvents. In a set of dissolution experiments by Cooper *et al* using binary solutions into glassy polymer (PMMA), a small amount of kinetically good but thermodynamically bad solvent (methanol or ethanol) with a kinetically bad but thermodynamically good solvent (MEK) was seen to increase the polymer dissolution rate. [89] Manjkow *et al* [36] also observed enhanced dissolution rates for a thermodynamically good/ bad mixture of MEK and isopropanol. They concluded that the smaller non-solvent molecules diffused *ahead* of the larger good solvent molecules. A model to explain the results of Cooper *et al* [89] and Manjkow *et al* [36] has been developed by Devotta and Mashelkar. [101]

An additional interesting set of experiments were performed by Lane *et al.* [18] They used MRI to show that a small quantity of acetone could induce a transition form Fickian to Case II ingress for methanol diffusion into PMMA.

3.1.2 Literature summary of binary mixed thermodynamically good solvents

The solvents ingress at the same rate

For the system of VR ingressed by benzene and acetone (both thermodynamically good solvents), Webb and Hall [95] used a chemical shift selection technique to observe the solvent components independently. They saw that the ingress rates of the two components were identical, with the diffusion rate of the acetone increased compared to when it was ingressed alone into VR. The rate of benzene diffusion was reduced when mixed with acetone compared to ingress of benzene as the lone component. Like Kwei and Zupko, they made no assessment, even qualitatively, of the solvent concentration distribution of the two components within the swelling polymer.

The kinetically good solvent ingresses ahead of the kinetically bad solvent

Long and Thompson also studied thermodynamically good solvent binary mixtures ingressing polymer. [90] They explained the two stage absorption process they observed by stating that the small solvent molecules diffuse ahead of the larger solvent molecules even when the two solvents are immiscible.

3.1.3 Aim

The review above leads to the conclusion that understanding of the ingress of mixed solvents into glassy polymers is far from complete. The issues raised highlight the need for spatially resolved and solvent specific concentration data. The availability of this kind of data is extremely limited. It is the purpose of this chapter to explore the separate concentration profiles of mixtures of good and bad solvents ingressing a glassy polymer and to monitor the changes when the relative fractions of the solvents in contact with the polymer are varied. We chose a polymer/ solvent system that could be used to test the model proposed by Devotta and Mashelkar. [101] Namely a mixture of a thermodynamically good/ kinetically bad solvent (we chose MEK, also commonly called 2-butanone) and a thermodynamically bad/ kinetically good solvent (we chose ethanol) ingressing a glassy polymer (we chose polystyrene). MEK has a value of χ of 0.49 [102] for a large excess of solvent in the polymer at 25°C. For ethanol, $\chi = 1.80$ [103] for a large excess of polymer in the mixture, at 162°C. χ is a function of temperature [103] so the value at room temperature may be much higher. MEK and ethanol have molar volumes of $90.1\text{cm}^3\text{mol}^{-1}$ and $58.5\text{cm}^3\text{mol}^{-1}$, respectively, indicating that ethanol is the better solvent kinetically. [89]

^{1}H, ^{2}H and CYCLCROP profiling techniques have been used. For the deuterium experiments, one of the solvent components was selectively deuterated and then deuterium NMR profiling was performed so that the ingress dynamics of the individual solvent type could be measured. This was done with an 80% MEK and 20% ethanol mixture (by volume) with first one solvent component deuterated and then the other. Their are two disadvantages with visualising the solvent components in this way. Firstly, two experiments need to be run with alternate deuterated components. Differences between samples may exaggerate differences in the ingressing solvents. Secondly, the mass of the deuterated solvents is higher than their protonated equivalents. This may have an effect on the ingress rate.To overcome the shortcomings of these ^{2}H NMR experiments, CYCLCROP, a chemically selective NMR technique was also used. This pulse sequence was implemented on a 70vol% MEK and 30vol% ethanol mixture ingressing polystyrene. The position of each component can be tracked separately and simultaneously so variations between samples can be excluded as the cause of any differences. Normal, unlabelled solvents have been used overcoming the second shortcoming of performing deuterium experiments. We have assumed that the two solvent components have similar relaxation time characteristics in solution and thus obtained solvent concentration profile shapes of the individual solvents.

Additional experiments have been run with conventional ^{1}H spin-echo imaging and ellipsometry to ascertain the effects of varying the solvent ratios in the reservoir. Encouragingly, MRI and ellipsometry were found to be entirely complementary in their temporal and spatial resolution. MRI was found to be ideal for looking at fast experiments with a high MEK fraction (50vol% MEK and above) and ellipsometry good for probing slow ingress with 40vol% MEK fractions and below. In this chapter, we also suggest that the Devotta and Mashelkar model is based on erroneous equations. We present a simple new model that describes well the essential features of our experimental findings.

3.2 Polystyrene sample preparation

Polystyrene powder with Mw= 325,000g/mol (Mw/Mn=1.04) (Polymer Laboratories Ltd., Church Stretton, UK) was compressed in a steel press under a pressure of 50kPa at 180°C for eight hours under vacuum. A vacuum was used to prevent oxidation of the samples. The polystyrene was slowly cooled, still under vacuum, until the temperature was well below the glass transition. The final cylindrical pellets were approximately 4mm thick with a diameter of 8mm. The PS was then inserted into a polytetrafluoroethylene (PTFE) sleeve. A solid glass rod was placed on the bottom of an NMR test tube (10mm outside diameter) to provide a flat base. The PS in its sleeve was then pushed onto the glass rod and glued down with an industrial adhesive. The PTFE sleeve was of such a thickness that it prevented flow of polymer down the sides of the test tube without applying a transverse stress. An MEK and ethanol mixture (all solvents were obtained from Sigma Aldrich Co. Ltd., Gillingham, UK) was then poured on top. A bung was placed on the end of the tube to prevent the solvent from evaporating. This sample presentation was chosen as it allowed the ingress to be considered as one dimensional, very useful as it makes later modelling much simpler. As one can see in the MR images shown in Figure 3.1 and described in Section 3.3, the PS is indeed seen to swell unidirectionally, with a negligible amount of curvature on the surface.

3.3 ^{1}H NMR imaging of MEK and ethanol ingressing polystyrene

A reservoir containing 80vol% MEK and 20vol% ethanol was used first to ingress the PS. The spin-echo imaging sequence at $\omega_0 = 400$MHz was used as described in Section 2.3.4. The acquisition parameters used were: 90° pulse length= 4μs, echo time= 0.0145s, repetition time= 1s and number of phase steps= 128. The maximum phase and read gradient strengths were 2.45 and 9.79G/cm respectively. These parameters gave an acquisition time of 34 minutes for 16 averages. For the initial, quick swelling only four averages were used. This still gave an adequate signal-to-noise ratio. The plane image pixel size was 23μm by 94μm. After the run had been completed, NMR proton spectra were taken of the solvent mixture above the swollen PS to verify that the polystyrene had not dissolved. No polystyrene lines were found in the MEK/ ethanol reservoir indicating that dissolution had not occured. A typical set of images is shown in Figure 3.1. At the top of each image one can see the solvent reservoir in grey. The bright region is the expanding gel layer. The PTFE, glassy polystyrene and the glass rod supporting the sample appear dark. From each image, profiles through the sample were made by summing the middle ten rows. A set of profiles is shown in Figure 3.2. The central part of each profile shows signal from the swollen rubber region. With time, this region is seen to swell. The solvent reservoir is to the left in the profiles. The signal from the reservoir is strongly attenuated by rapid self diffusion of the liquid molecules in the magnetic field gradient and by the short repetition time of the experiment compared to the free liquid nuclear spin-lattice relaxation time. The polymer glass (not visualised) is to the right. The width of the rubber region has been directly measured from these profiles and is shown in Figure 3.3. The polymer swelling is in accordance with generalised Fickian diffusion, since the width increase is proportional to the square root of time.

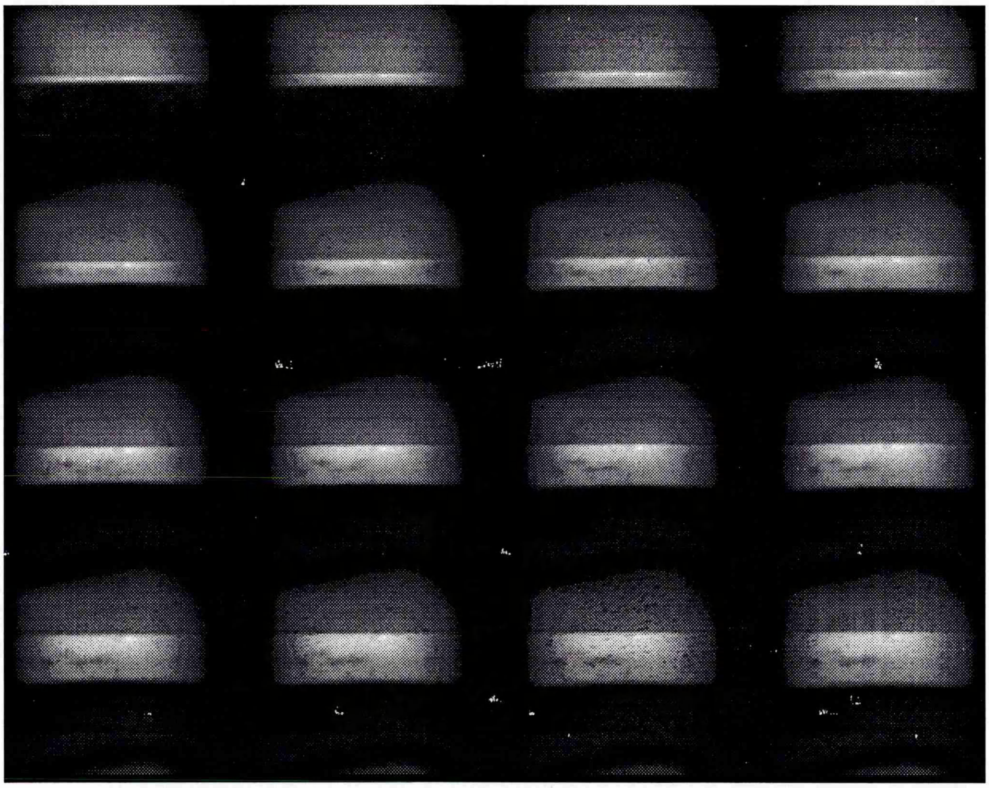

Figure 3.1: NMR microscopy images of a mixture of 80% MEK and 20% ethanol ingressing Mw= 325,000g/mol PS. Alternate images are shown hence the time between each displayed image is 68 minutes.

3.4 ^{2}H NMR profiling of MEK and ethanol ingressing polystyrene

To assess whether both solvents ingress together two further experiments were now recorded in which one or other of the solvents was partially deuterated.

3.4.1 The ^{2}H probe, NMR acquisition parameters and experimental details

An in-house built deuterium probe was used (ω_0 = 61.4MHz at 9.4T). This comprises a saddle type inductor coil (as discussed in Section 2.3.8) and fixed-

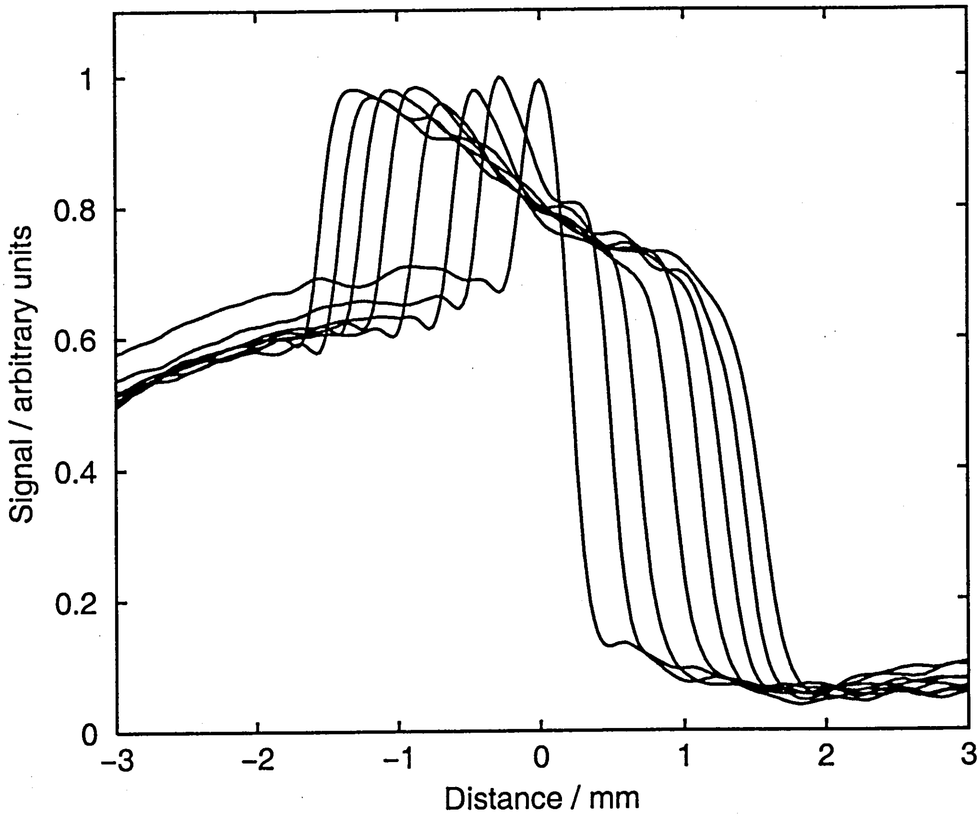

Figure 3.2: ^{1}H profiles of 80% MEK and 20% ethanol ingressing PS. The solvent is to the left, the progressively swelling rubber is in the middle and the glass is to the right. The original sample surface is at 0mm on the scale.

value tuning capacitors connected in parallel. The coil was wound with sticky backed copper tape onto a thin walled glass rod with a 10mm inside diameter suitable for standard MRI test tubes. The glass rod was glued with epoxy resin into a PTFE holder which was screwed onto an aluminium probe body. A spin-warp 1D profiling sequence was implemented rather than a 2D image acquisition, as the SNR was poor due to the low γ of deuterium. The acquisition parameters used for deuterium profiling were: Gaussian pulse length= 500μs, read gradient stength= 30.0 G/cm, read time= 10.24ms and repetition time= 1s. These parameters gave an acquisition time of 17 minutes for 1024 averages. The spatial resolution in the x direction was 51μm. The binary solvent mixture of 20% ethanol and 80% MEK by volume was placed in contact with the PS. It

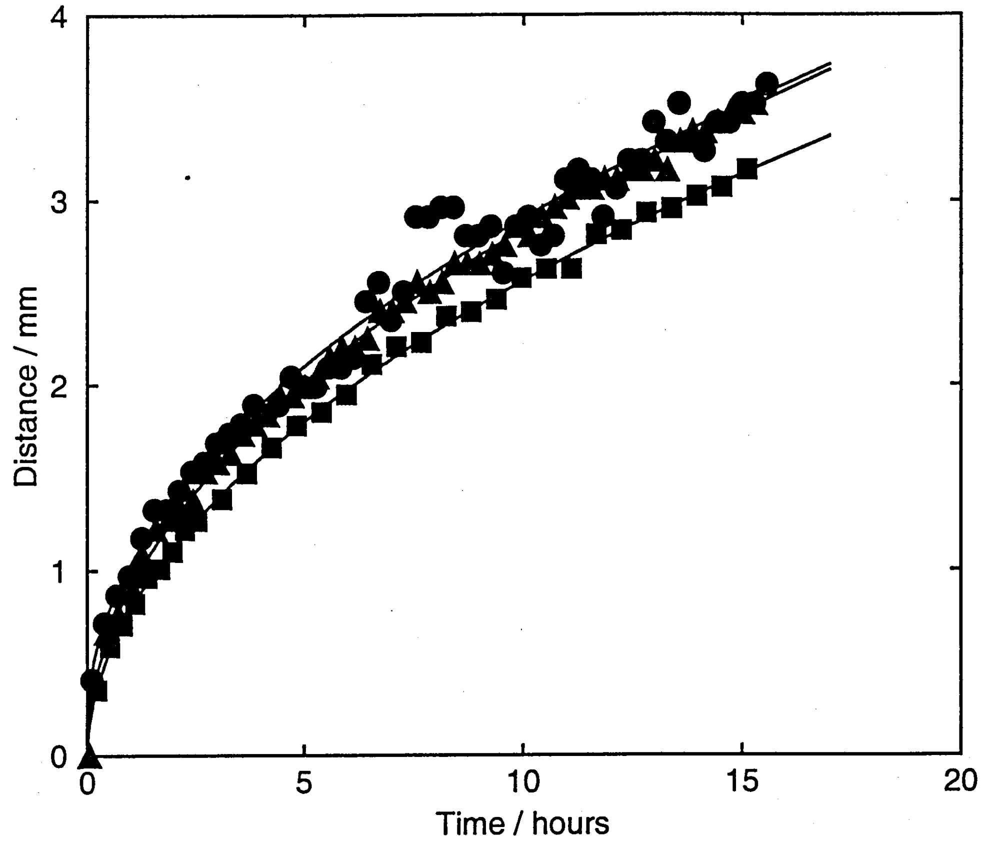

Figure 3.3: The width of the rubber region in swelling PS recorded using ^{1}H (squares), ^{2}H MEK (circles) and ^{2}H ethanol (triangles) profiling. The solid lines are fits to the equation $x = At^{1/2}$. The solvent fronts go in together.

contained either 20% deuterated MEK/ 60% protonated MEK / 20% protonated ethanol or 20% deuterated ethanol/ 80% protonated MEK. The deuterated solvents were chosen such that exchange of deuterium with the protons of the non-deuterated solvent would not occur. The solvents used were $CH_3CD_2COCD_3$ and CD_3CH_2OH.

3.4.2 Experimental results and analysis

Half-heights of the ingress of the solvent front positions were plotted against time as shown in Figure 3.3. Comparison of the half-height solvent front positions clearly and unambiguously show the MEK and ethanol fronts ingressing at the same rate and with Fickian dynamics. The concentration profiles have

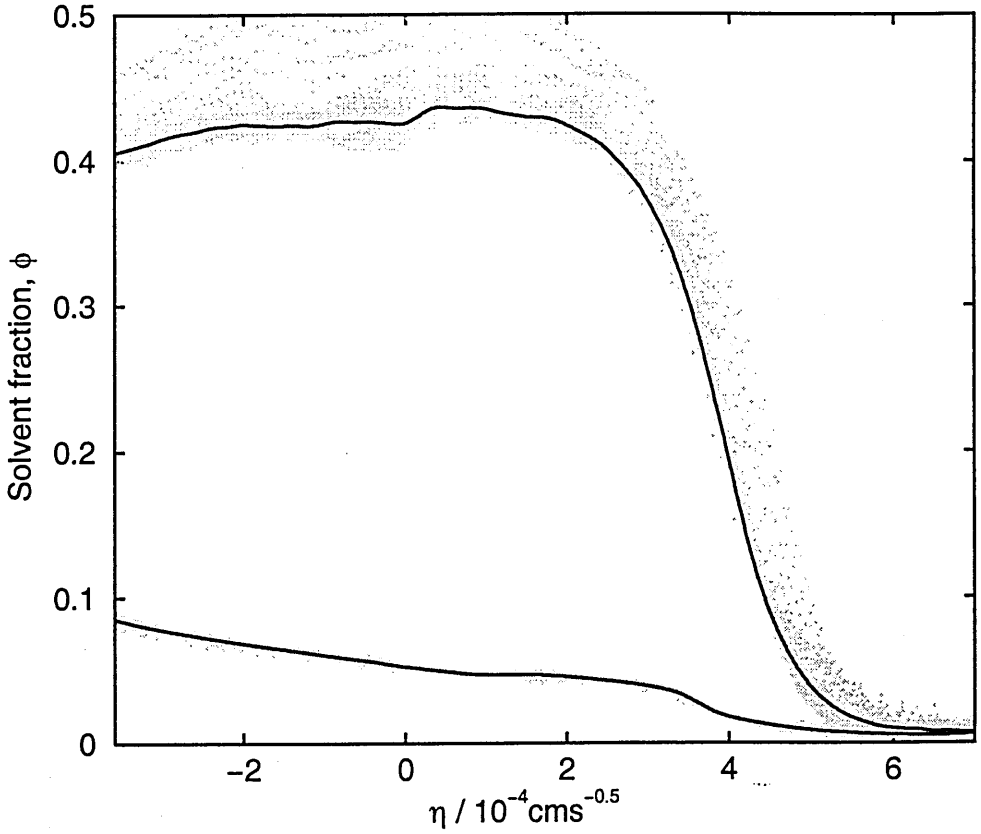

Figure 3.4: Boltzmann transformed profiles of 80% MEK / 20% ethanol ingressing 325,000g/mol PS. The averaged MEK is shown with the top line, the averaged ethanol below. The dots show the unaveraged signal from all the profiles

been transformed according to the Boltzmann transform [8], $\eta = z/2t^{1/2}$. The resulting master experimental concentration profiles for Mw= 325,000g/mol are shown in Figure 3.4. The solid MEK curve shows 53 transformed and summed profiles (recorded over 15 hours) and the ethanol curve shows 69 transformed and summed profiles (recorded over 19.5 hours). The profiles were normalised to the concentrations shown in the figure by considering the fact that the concentration at the reservoir/ gel boundary is always at the equilibrium value. The equilibrium concentration values have been found experimentally are are described in Section 3.6. The reservoir/ gel boundary position is found easily. It is indicated by a steep gradient in the signal versus η plot. Figure 3.4 has been scaled only to include concentration values from this point. The solvent concentration profiles for the MEK and ethanol are not the same. Assuming the spin relaxation times and self diffusion of the two solvents are comparable at any given location, then the MEK profile is more square and the solvent front more sharp than the corresponding ethanol profile.

3.5 CYCLCROP profiling of MEK and ethanol ingressing polystyrene

A CYCLCROP profiling sequence was used next to follow the ingress of 70% MEK / 30% ethanol into Mw= 325,000g/mol PS. The solvents had ^{13}C present only at the level of natural abundance. The CH_3 bonded to the ethyl group of the MEK and the CH_3 group of the ethanol were selected. Alternate profiles of these species were obtained. The PRAWN variant of the method was used with 15 coupling pulses with a nominal flip angle of 24° applied over 4.5ms for both MEK and ethanol. The profiles typically took 2.4 hours to acquire. They were not therefore acquired during the early part of the ingress when the concentrations were varying rapidly. Boltzmann transformed profiles of the ingress are shown in Figure 3.5. In this plot, both the lines show 10 summed profiles. They were normalised to the concentrations shown in the same way as described in Section 3.4.2. The dots are the complete set of unaveraged Boltzmann transformed profiles. These profiles were not only summed but corrected for the roll-off from the coil. To find how the signal varied through a homogeneous sample, a CYCLCROP profile of a pure solvent sample that filled the coil was recorded. The resulting curve was fitted to a parabola. The dotted Boltzmann transformed profiles shown were divided by this parabola. Again, the resulting profiles for the two solvents are different,

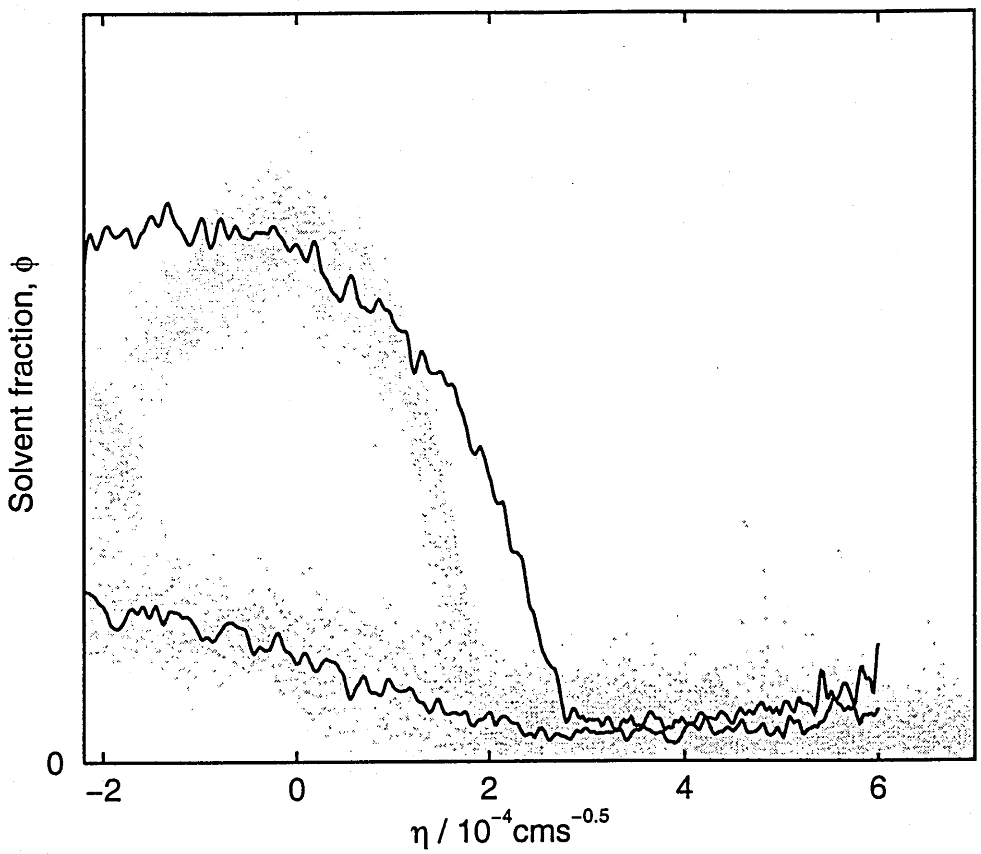

Figure 3.5: Boltzmann transformed profiles of 70% MEK / 30% ethanol ingressing 325,000g/mol PS. The MEK is shown in the top line, the ethanol below. These lines represent an average value obtained from the two sets of ten profiles. These data have been corrected to compensate for the coil roll-off. The dots show the the original signal from all the uncorrected profiles

but their shapes are very similar to the deuterium profiles shown previously in that there is a square MEK profile and a smooth ethanol profile. As one would expect, since there is a lower MEK fraction in this experiment compared to the ^{2}H experiment, the solvents are shown to move in more slowly.

3.6 Equilibrium fractions of MEK, ethanol and polystyrene mixtures

When modelling ingress experiments, it is vital to know the equilibrium fractions of solvents in the polystyrene. These can be calculated using the equations of Flory and Huggins. At thermodynamic equilibrium, the chemical potentials of the solvents in the reservoir are equal to those in the swollen polymer. According to Flory-Huggins theory [22], the chemical potentials of the two solvents in the gel phase relative to the pure solvents are given by

$$\begin{aligned}\frac{\mu_1^G-\mu_1^0}{RT} &= \ln(\phi_1)+(1-\phi_1)-\phi_2(V_1/V_2)-\phi_3(V_1/V_3)\\ &+ (\chi_{12}\phi_2+\chi_{13}\phi_3)(\phi_2+\phi_3)-\chi_{23}(V_1/V_2)\phi_2\phi_3, \qquad (3.1)\end{aligned}$$

$$\begin{aligned}\frac{\mu_2^G-\mu_2^0}{RT} &= \ln(\phi_2)+(1-\phi_2)-\phi_1(V_2/V_1)-\phi_3(V_2/V_3)\\ &+ (\chi_{21}\phi_1+\chi_{23}\phi_3)(\phi_1+\phi_3)-\chi_{13}(V_2/V_1)\phi_1\phi_3, \qquad (3.2)\end{aligned}$$

where the subscripts 1,2 and 3 denote solvent 1, solvent 2 and the polymer respectively. μ_i^G is the chemical potential of component i in the gel phase, μ_i^0 is the chemical potential of component i when it is pure, ϕ_i is the volume fraction of component i, V_i is the molar volume of component i and χ_{ij} is the Flory-Huggins interaction parameter between components i and j. The chemical potentials of the two solvents in the liquid reservoir relative to the pure solvents are

$$\frac{\mu_1^L-\mu_1^0}{RT}=\ln(\phi_1)+(1-(V_1/V_2))\phi_2+\chi_{12}\phi_2^2, \qquad (3.3)$$

$$\frac{\mu_2^L-\mu_2^0}{RT}=\ln(\phi_2)+(1-(V_2/V_1))\phi_1+\chi_{21}\phi_1^2, \qquad (3.4)$$

where μ_i^L is the chemical potential of component i in the liquid phase. However, to find the equilibrium solvent fractions by equating Equation 3.1 to Equation

3.3 and Equation 3.1 to Equation 3.3 requires knowledge of the Flory-Huggins interaction parameters χ_{ij} as a function of concentration. The concentration effects on χ_{ij} are often wrongly neglected. [19, 103] One can find values in the literature for the interaction parameter of MEK and PS. [104] Since ethanol only ingresses PS at very high temperatures, values of χ_{ij} can only be found at 162°C or above and for an infinitely small solvent fraction. [24] Too few values are known to extrapolate back from this data to temperature and concentration levels used in the experiments described above. Solvent-solvent interaction parameters are rarely quoted in the literature. [22] As a consequence of a dearth of information, we have chosen to find the equilibrium fractions experimentally using ^{1}H NMR spectroscopy. Large volumes of mixtures of MEK and ethanol with volume fractions of 70, 75, 80 and 90% MEK were poured onto PS pellets with Mw= 280,000g/mol (Sigma Aldrich Co. Ltd., Gillingham, UK) in NMR test tubes and allowed to equilibrate for a number of weeks. Care was taken to ensure that no air bubbles were present. The spectra of the resulting swollen polymer samples were recorded. Integrating under the peaks of the NMR spectra of these samples allowed us to extract the equilibrium concentrations. These are shown in Figure 3.6. Attempts were made to solve for the solvent-solvent and solvent-polymer interaction parameters simultaneously using the Flory-Huggins equations and assuming χ_{ij} varied as $\chi_{ij} = X_0 + X_1\phi_3 + X_2\phi_3^2$ where ϕ_3 is the PS fraction and X_0, X_1 and X_2 are the constants for each χ_{ij}. [103] It should be noted that χ_{ij} is not the same as χ_{ji}. They are related by the ratio of their molar volumes: $\chi_{ji} = \chi_{ij}(v_j/v_i)$ where v_j and v_i are the molar volumes of components i and j respectively. [22] Solving for all the χ parameters did not give a meaningful result. Inevitable experimental errors appeared to dominate. Setting $\chi_{12} = 0.0$, $\chi_{23} = 0.5$ and $\chi_{13} = 1.5$, where the subscripts 1, 2 and 3 denote ethanol, MEK and PS, respectively, and neglecting concentration dependence does predict equilibrium concentrations close to those we have measured. These values of χ_{ij} are very reasonable in that $\chi_{12} = 0$

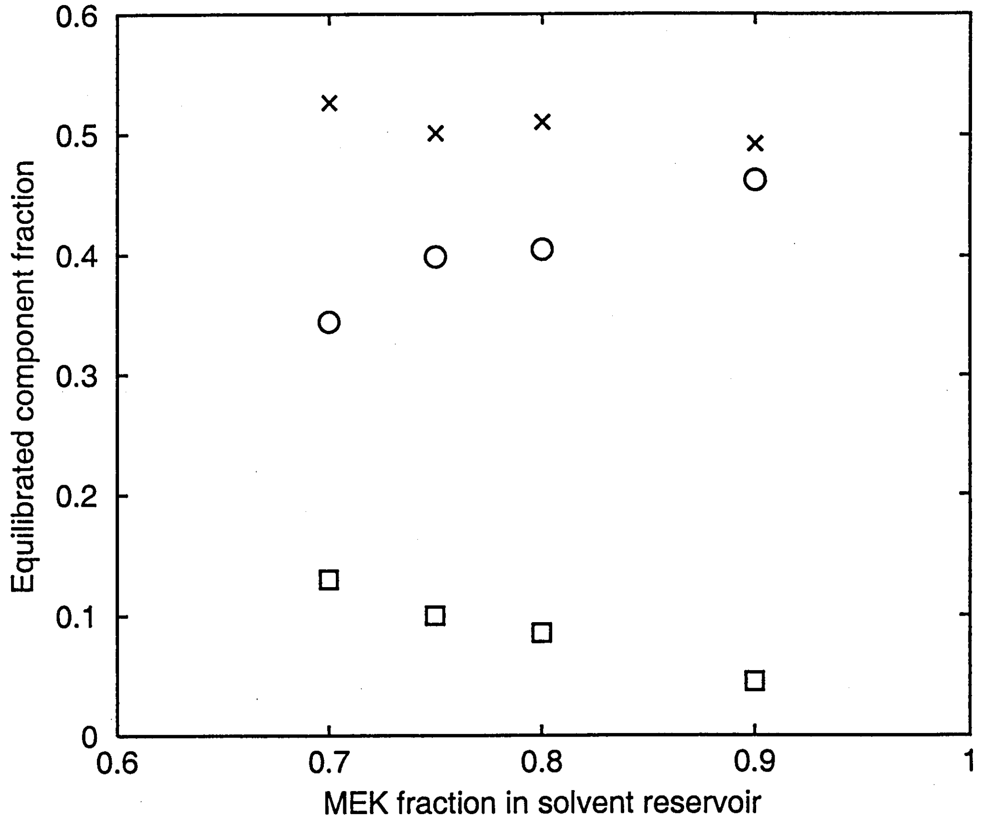

Figure 3.6: Equilibrium fractions of MEK (circles) and ethanol (squares) in PS (crosses) for a reservoir of ethanol and MEK as a function of MEK fraction.

corresponds to mixing of solvents in all fractions, $\chi_{13} = 1.5$ describes ethanol as a bad solvent and $\chi_{12} = 0.5$ describes MEK as a good solvent. [22] With a technique that could find values for equilibrium solvent fractions with less error, using a bicomponent mixture of solvents could prove a good way to find χ_{ij} values for bad solvent-polymer combinations. Such measurements would otherwise not be experimentally determinable as the bad solvent does not ingress the polymer.

3.7 The Devotta and Mashelkar model

Devotta and Mashelkar [101] have presented a model, in part to explain the unexpected dissolution behaviour in some systems already discussed. [36, 89] The model predicts that, in general, competition between thermodynamic and kinetic factors will lead to differential uptake rates. We have neglected dissolution in our implementation of the model. Devotta and Mashelkar consider the swollen system to include three regions: a glassy polymer region, a swollen gel region and an infinite reservoir of two mixed solvents. Having used Equations 3.1 to 3.4 to find the solvent volume fractions at the surface of the gel region, Devotta and Mashelkar use Fick's second law written in terms of concentration gradients to describe the solvent flux in the gel region. They write:

$$\frac{\partial \phi_1}{\partial t} = \frac{\partial}{\partial x}\left(D_1 \frac{\partial \phi_1}{\partial x}\right), \tag{3.5}$$

$$\frac{\partial \phi_2}{\partial t} = \frac{\partial}{\partial x}\left(D_2 \frac{\partial \phi_2}{\partial x}\right), \tag{3.6}$$

where D_1 and D_2 are the diffusion coefficients of solvents 1 and 2 in the polymer. The concentration dependence of the diffusion coefficients depend on the size of the solvent molecules and they can be related to the free volume by:

$$D_1 = A_1 \exp\left(\frac{-B_1}{f_1\phi_1 + f_2\phi_2 + f_3\phi_3}\right), \tag{3.7}$$

$$D_2 = A_2 \exp\left(\frac{-B_2}{f_1\phi_1 + f_2\phi_2 + f_3\phi_3}\right). \tag{3.8}$$

A_1, B_1, A_2 and B_2 are parameters that depend on the size of the diffusing species. The free volumes of the two solvents and the polymer are: f_1, f_2 and f_3. Devotta and Mashelkar also use the initial boundary condition that at $x > 0$ $t = 0$ $\phi_1 = \phi_2 = 0$. A computer program has been implemented to solve these equations. Figure 3.7 shows the output for the model for the parameters: $A_1 = 3.0 \times 10^{-10}\mathrm{cm}^2\mathrm{s}^{-1}$, $A_2 = 1.5 \times 10^{-10}\mathrm{cm}^2\mathrm{s}^{-1}$, $B_1 = 0.3$, $B_2 = 0.15$, $f_1 = 0.102$, $f_2 = 0.034$ and $f_3 = 0.0905$, where subscript 1 indicates ethanol, subscript 2 indicates MEK and subscript 3 indicates PS. The equilibrium surface concentrations used were $\phi_1 = 0.0855$ and $\phi_2 = 0.404$. The free volumes

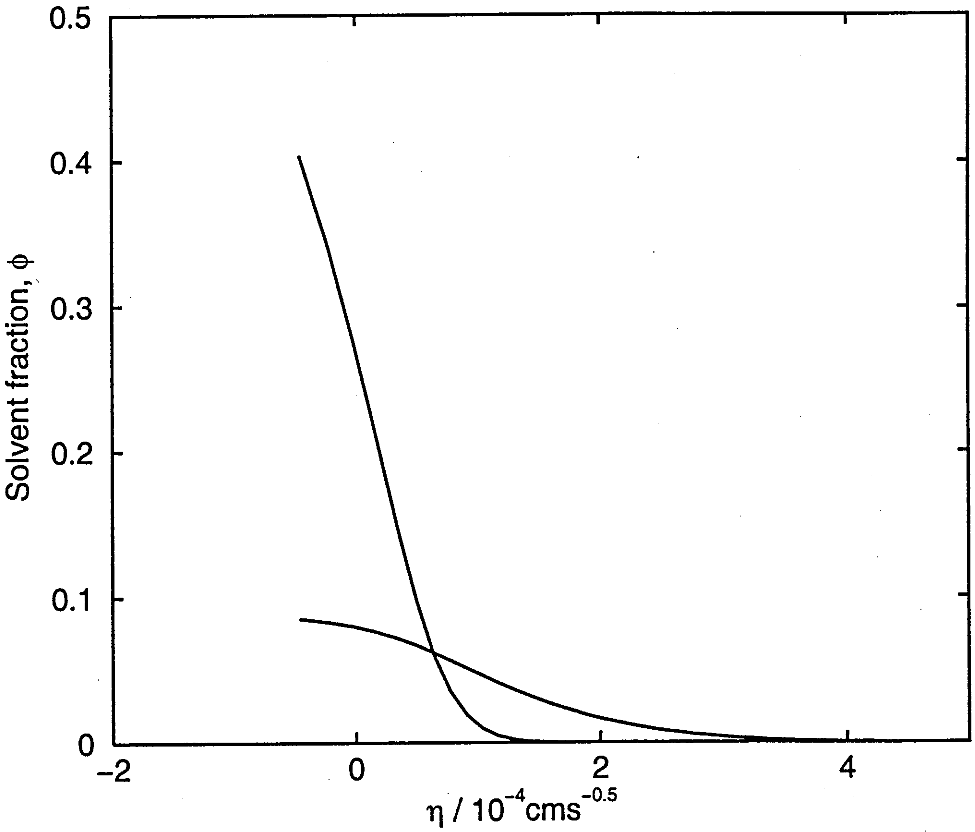

Figure 3.7: Boltzmann transformed profiles of simulated 80% MEK / 20% ethanol ingressing PS using the Devotta and Mashelkar model. The MEK is shown above, the ethanol below.

were calculated from theory discussed in the literature. [6, 105] The equilibrium solvent fractions were found experimentally as described in Section 3.6. The diffusion coefficients are of the same order of magnitude to those found in the literature. The ethanol was predicted to diffuse in PS more quickly than does MEK because of the smaller physical size of the former. In Figure 3.7 one can see that the Devotta and Mashelkar model predicts that the solvent fronts move at different rates and the concentration profiles have similar smooth profiles, far from the square MEK profile we observe in our experiments. The only way that this model can predict the fronts moving in at the same rate is if the diffusion coefficients of the two solvents are identical. The only way this can realistically occur is, of course, when the solvents are the same. The limitation of the Devotta and Mashelkar model is that they consider only the diffusion coefficients of the solvent diffusing the polymer (D_{13} and D_{23}). They neglect the diffusion of the solvents in each other (D_{12}).

3.8 A new model for mixed solvent ingress into polymer

In the model described here, we build on the early work of Cussler and Lightfoot into mixed solvent ingress in polymers. [106] For a ternary ($n = 3$) multi-component diffusion system one can write:

$$F_i = -\sum_{j=1}^{3} D_{i,j} \frac{\partial \phi_j}{\partial z} \tag{3.9}$$

where F_i is the flux of component i, $D_{i,j}$ is a multi-component diffusion coefficient, ϕ_j is the concentration of component j, and z is position. In general $D_{i,j} \neq D_{j,i}$ and the coefficients are strongly concentration dependent. Conservation of mass and flux means that only four of the nine components $D_{i,j}$ are mutually independent. [107] These four can be chosen in a variety of equivalent ways. For systems such as dilute gases, the equations can be reformulated in terms of the pairwise binary diffusion coefficients $D^*_{i,j}$. [108] However, for condensed liquids and polymers this is not so straightforward. Some authors develop the analysis in terms of chemical potential driving forces and Flory-Huggins theory. [88] Such analysis is attractive from the viewpoint of trying to characterise the ingress fully. However, it suffers in so much as it relies on adequate models of the chemical potential in the non-equilibrium swelling polymer and of the mobilities of the different components, both of which are difficult to obtain. Moreover, the approach then requires the use of a large number of fitting parameters. We base our analysis on a model derived from pairwise exchange of components as might be used in a simple Monte Carlo calculation. According to this very much simpler model we write:

$$F_i = \frac{\sum_{i\neq j} D^{+}_{i,j}}{\sum_k \phi_k}\left(\phi_i \frac{\partial \phi_j}{\partial z} - \phi_j \frac{\partial \phi_i}{\partial z}\right). \tag{3.10}$$

Equation 3.10 is derived in Appendix A. We can then write that

$$\frac{\partial \phi_i}{\partial t} = \frac{1}{\sum_k \phi_k}\left[\sum_{i\neq j} \frac{\partial}{\partial z} D^{+}_{i,j}\left(\phi_j \frac{\partial \phi_i}{\partial z} - \phi_i \frac{\partial \phi_j}{\partial z}\right)\right]. \tag{3.11}$$

The number of independent parameters is now reduced to three since we require $D^{+}_{i,j} = D^{+}_{j,i}$. The set of diffusion equations have been solved numerically for the boundary conditions

$$\phi_i = \phi_i^{eq} \qquad z = 0,\ t \geq 0 \tag{3.12}$$

$$\phi_i = 0 \qquad z > 0,\ t = 0. \tag{3.13}$$

The first states that the surface of the sample is maintained at equilibrium concentration throughout. The second states that the body of the sample is initially pure polymer. The characteristic features of the data now result if we assume that

$$D^{+}_{1,2} = \text{constant}, \tag{3.14}$$

$$D^{+}_{1,3} = 0, \tag{3.15}$$

$$D^{+}_{2,3} = \begin{cases} 0 & \text{if } \frac{\phi_2}{\phi_2+\phi_3} < \phi_{TG} \\ \text{constant} & \text{otherwise.} \end{cases} \tag{3.16}$$

The subscripts 1,2 and 3 denote ethanol, MEK, and PS respectively. Equation 3.14 implies a single, concentration independent mutual diffusivity for the two solvents. Equation 3.15 implies that ethanol does not diffuse in PS. Equation

3.16 implies a strongly concentration dependent diffusivity for MEK in PS. The simplest possible form has been chosen, namely a step function. The critical concentration ϕ_{TG} is the MEK in PS fraction required to induce a glass-to-rubber transition at the experimental temperature. The diffusion coefficients used here represent a simplification of the problem. More correctly, they will all be strong functions of concentration, but in this instance we only wish to demonstrate the essentials of the physics involved, rather than producing perfectly fitted diffusion coefficient parameters. In our implementation of the mathematics, all are calculations are performed in a fixed polymer mass reference frame. The swelling is incorporated later. As the solvents swell the polymer, the increase in the concentration of the solvents in a fixed quantity of polymer must lead to a relative decrease in polymer concentration. Hence to find the amount of swelling in each element, the initial size of each one is simply divided by the polymer concentration. Figure 3.8 shows the resulting theoretical, Boltzmann transformed profiles, which can be directly compared to the experimental data. An overlay has not been attempted, since the experimental data is relaxation attenuation weighted. Nonetheless, the essential features are seen. The key point is that the solvent fronts move in together but the shape of the concentration profiles are very different. The MEK shows a sharp solvent front, whereas the ethanol concentration varies much more uniformly. The MEK front arises because of the strong concentration dependence of $D^{+}_{2,3}$. However, since the flux at the solvent front is not limited by the viscoelastic polymer swelling, the system stays Fickian and not Case II. The ethanol cannot proceed beyond the front, but can diffuse rapidly in the swollen region due to the presence of the MEK. The flux of the ethanol across the swollen region, which is proportional to the concentration gradient, matches that required to keep pace with the swelling of the polymer by the ingressing MEK. In consequence, the ethanol concentration at the front remains constant and small. The values of diffusion coefficient used

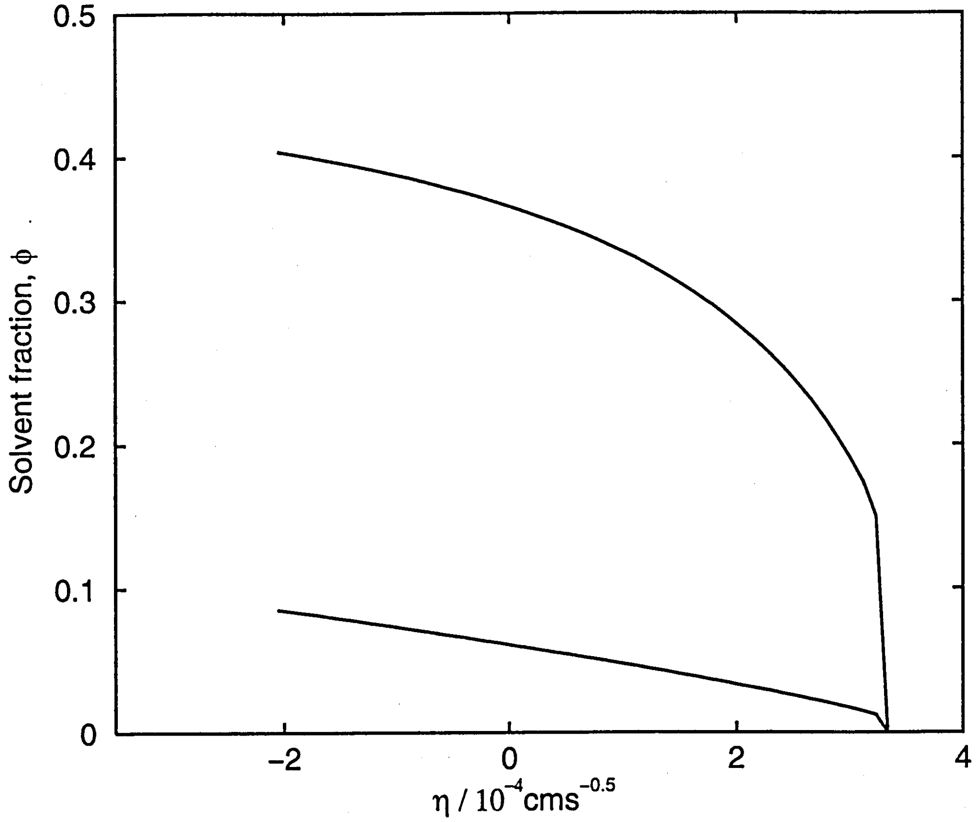

Figure 3.8: Theory master curves of MEK (top) and ethanol (bottom). The MEK profile shows a sharp front with a high solvent fraction throughout the rubber. The ethanol fraction decreases across the rubber to near zero at the front. This compares favourably with the experimental data.

in this comparison are: $D^{+}_{1,2} = 1 \times 10^{-5}\mathrm{cm}^2\mathrm{s}^{-1}$ and $D^{+}_{2,3} = 1 \times 10^{-5}\mathrm{cm}^2\mathrm{s}^{-1}$ for $\phi_2/(\phi_2 + \phi_3) > \phi_{TG} = 0.17$. From the experimental results described in Section 3.6, the surface concentrations were set at $\phi_1 = 0.0855$ and $\phi_2 = 0.404$. These values of diffusion coefficient are consistent with experimentally measured diffusion coefficients resulting from direct integration of the Boltzmann transformed experimental data. In particular, $D^{+}_{1,2}$ is also consistent with typical values of diffusion coefficient of small molecules to be found in the literature, and $D^{+}_{2,3}$ for larger concentrations is consistent with values reported for small molecules in swollen rubbers. The diffusion coefficient of both MEK at low concentration and ethanol in the glass is expected to be very small.

3.9 Experimental results: varying MEK fraction

3.9.1 ^{1}H NMR microimaging data acquisition

Polysytrene samples were prepared as described in Section 3.2. The solvent reservoir contained mixtures of MEK and ethanol varying from 50vol% MEK to 90vol% MEK in steps of 10%. This range was chosen as lower MEK fractions were too slow to be measured by MRI, but higher fractions dissolved the PS. Plots of solvent front position at half-height against time for mixtures of MEK and ethanol varying from 90% MEK/ 10% ethanol to 50% MEK/ 50% ethanol ingressing PS (Mw= 1,460,000g/mol, Mw/Mn= 1.06) are shown in Figure 3.9 The results of fitting the front positions to $x = kt^n$ are shown in Table 3.9.1. Fickian dynamics corresponding to $n = 0.5$ were observed, as one would expect given the results of Section 3.3. Mean diffusivities, D, have been extracted from the k fit parameter. For a semi-infinite medium, with the boundary at constant concentration C_0, for a non-swelling sample and assuming a constant D, we can

Table 3.1: The results of fitting $x = kt^n$ and $x = k't^{0.5}$ to diffusion profiles with varying solvent fractions

MEK fraction	k	n	D/ 10^{-7}cm^{2}s^{-1}	k'
50%	0.116	0.516	0.406	0.123
60%	0.274	0.517	2.27	0.286
70%	0.458	0.519	6.34	0.479
80%	0.793	0.509	19.0	0.809
90%	1.084	0.496	35.5	1.079

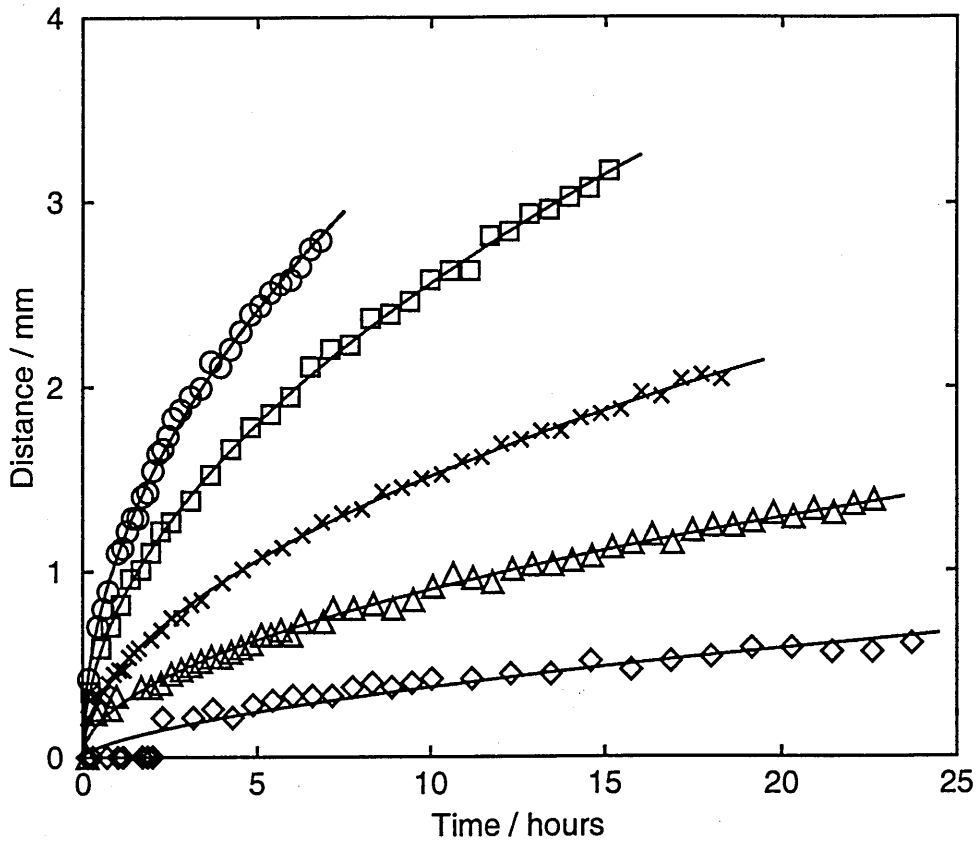

Figure 3.9: Half-height solvent front position of MEK/ ethanol mixtures ingressing PS. The symbols depict the different solvent fractions as follows: 50% MEK/ 50% ethanol (diamonds), 60% MEK/ 40% ethanol (triangles), 70% MEK/ 30% ethanol (crosses), 80% MEK/ 20% ethanol (squares), 90% MEK/ 10% ethanol (circles).

write that the concentration C through the sample is [8]

$$C = C_0 \mathrm{erfc}\left(\frac{x}{2(Dt)^{1/2}}\right). \tag{3.17}$$

Assuming concentration is proportional to NMR signal, we have plotted our front positions at $C/C_0 = 1/2$, so rearranging Equation 3.17 gives

$$x = 0.959(Dt)^{1/2}. \tag{3.18}$$

Hence

$$D = \left(\frac{k'}{0.959}\right)^2. \tag{3.19}$$

The calculated values of *D* are shown in Table 3.9.1. These increase markedly with MEK fraction.

3.9.2 Ellipsometry data acquisition

Ellipsometry sample preparation

PS films were prepared by the following procedure. PS of molecular weight 325,000g/mol (Mw/Mn=1.04) (Polymer laboratories Ltd., Church Stretton, UK) was dissolved in cyclohexanone (Sigma-Aldrich Co. Ltd., Gillingham, UK) in a conical flask, attached to a Leibig condensor and heated to boiling point until the PS was seen to be fully dissolved. This took about one hour. Approximately 5wt% polymer solutions were made and spin-cast onto clean (111) silicon wafers at 2000 rpm for 30 seconds. A syringe fitted with a filter was used to drop the solution onto the silicon wafers in order to remove any residual undissolved polymer or any other solid contamination. The aim was to make samples roughly 3000 Å thick. This thickness is sufficient to be considered a bulk film but not too thick to reduce the sensitivity of the ellipsometer or to give a rough surface. The samples were then heated in a vacuum oven at 180°C for 24 hours. This heating protocol was chosen firstly to be warm enough to remove any residual cyclohexanone and secondly to be well above T_g so as to relax any molecular order resulting from the spin coating process.

Ellipsometry data acquisition

An initial spectroscopic multiple angle ellipsometric scan, in air, was made of the bare silicon wafer to allow accurate measurement of the native oxide layer. The same scan was then performed on each of the PS coated samples to give an accurate pre-swelling thickness. The polystyrene samples were placed in a sample cell. The cell has thin stress-free glass windows at a fixed angle. In this case, an angle of 75° has been used, as this is close to the Brewster angle of the samples being measured. This provides the greatest sensitivity for ellipsometry. Values of ψ and Δ were obtained as a function of time using a wavelength of 500nm, initially without the solvent. After a minute or two of data acquisition, the solvent was quickly added. A typical set of ψ and Δ data is shown in Figure 3.10. The jump in ψ and Δ after about four minutes is when the solvent was quickly added. The gradual change in the parameters after this time are attributed to polymer swelling. Measurements of ψ and Δ are taken at about two second intervals. In this set of experiments, the MEK/ ethanol ratio was varied from 0:100 to 40:60 in increments of 10.

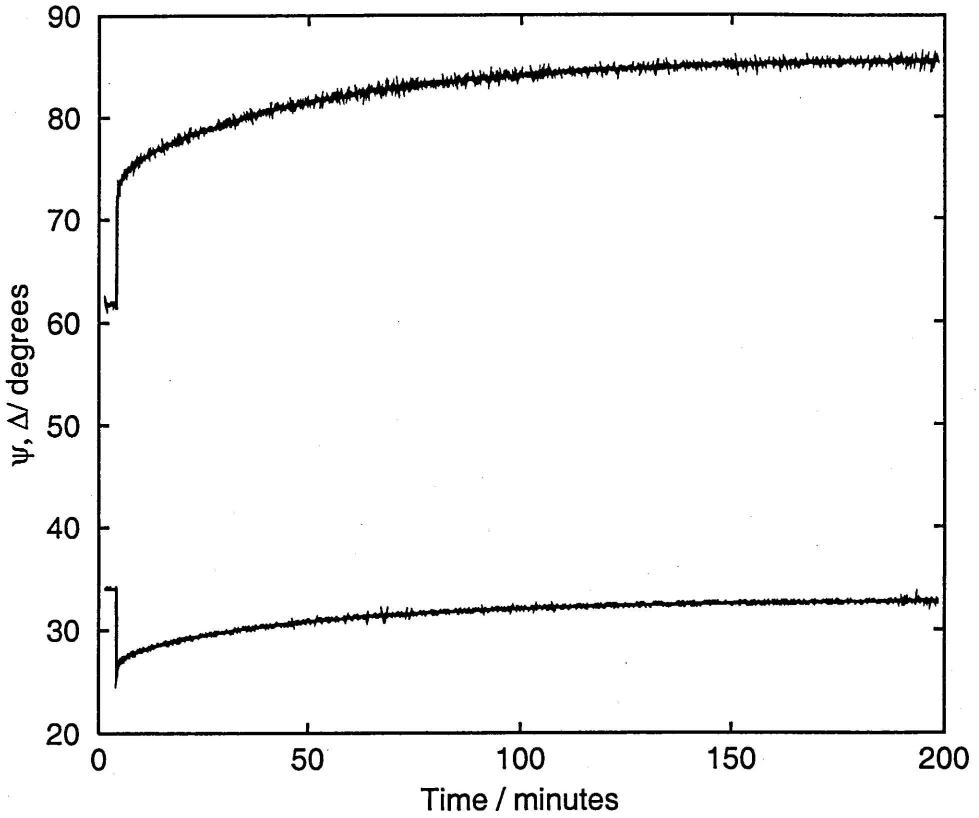

Figure 3.10: Typical ψ and Δ data recorded as a function of time for 20% MEK and 80% ethanol ingressing PS. The top line shows the values for Δ. ψ is shown by the lower line

Data fitting

The ψ and Δ versus time data were fitted to a three-layered model using a Levenberg-Marquardt algorithm. [85] The model consisted of a silicon substrate with a native oxide with a Cauchy layer (see Section 2.4.4) on top, representing the polymer. The refractive indices and the thicknesses of the silicon substrate and the native silicon oxide were fixed in the data analysis to standard values. The only fitting parameters were d, the PS thickness and na, the wavelength-independent component of the Cauchy dispersion model. The ambient refractive indices of the MEK in ethanol fractions were also fixed. Their refractive index values were measured independently using refractometry. These values are given in Table 3.2.

Experimental results

The results of fitting to the experimental ψ and Δ data are illustrated in Figure 3.11, which shows the effects of different reservoir solvent fractions on ingress. The replicate ellipsometry measurements show that the thickness values are extremely reproducible. On the whole, the ingress slows down with time. The

Table 3.2: The Cauchy coefficients for various fractions of MEK in ethanol

Solvent	na	nb
40% MEK/ 60% ethanol	1.3300	0.0062
30% MEK/ 70% ethanol	1.3312	0.0062
20% MEK/ 80% ethanol	1.3359	0.0061
10% MEK/ 90% ethanol	1.3338	0.0062
100% ethanol	1.3317	0.0062

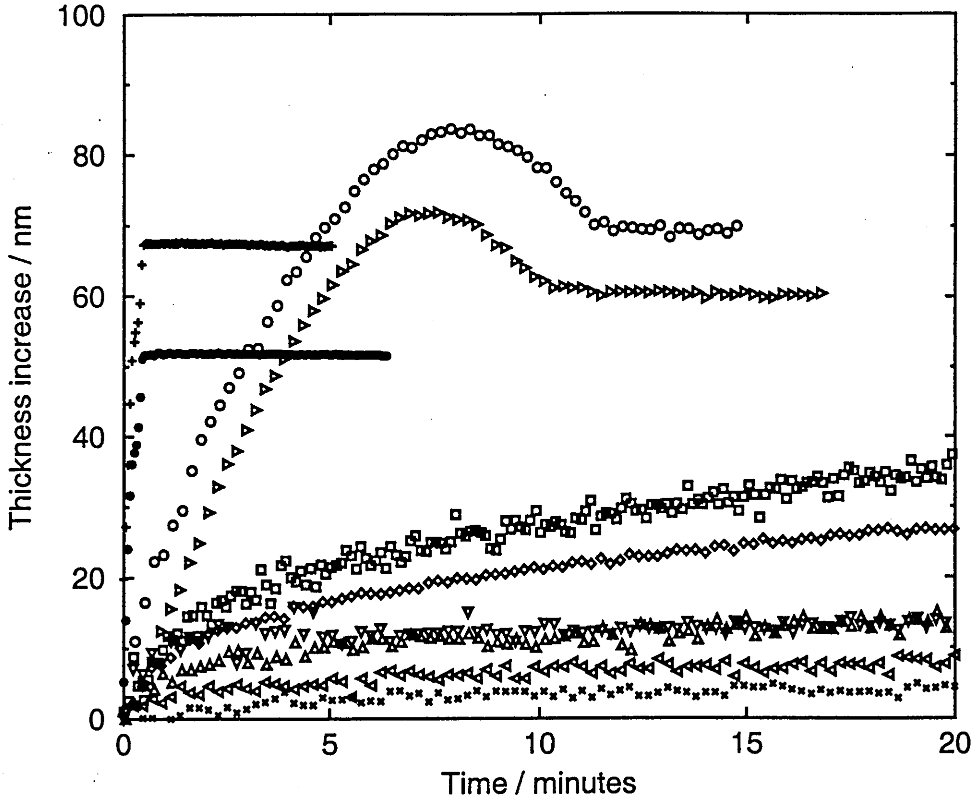

Figure 3.11: The depth of the Mw= 325,000 g/mol polystyrene being ingressed by varying fractions of MEK and ethanol mixtures as a function of time. This measurement has been made using ellipsometry. The crosses and left triangles are pure ethanol, the up and down triangles are 10% MEK, the diamonds and squares are 20% MEK, the right triangles and circles are 30% MEK and the pluses and circles are 40% MEK.

"hump" in the 30% MEK data is peculiar and is probably a result of an ambiguity in fitting the ellipsometry ψ and Δ data. Alternatively, it may be thought to indicate polymer dissolution. However, the results of NMR spectroscopy on ingress experiments involving *higher* MEK fractions (which are more likely to cause dissolution) described earlier show that PS dissolution does not occur. Overall, the greater the MEK fraction in the reservoir, the faster the ingress. Fitting an equation of the form: $x = kt^n$ to the solvent fraction data sets does not, however, give sensible values of n. Typically, when there is MEK in the reservoir values between 0.2 and 0.3 are found. At early times ingress rates, as also found in the MRI data, are of the order of nms^{-1}. For the pure ethanol sample, a value of n only slightly above zero (0.03) is found. This may show a tiny amount of very quick ingress followed by a complete halt. The difficulties in fitting realistic values of n to the ellipsometry data are likely to be due to the inadequacy of the model we are fitting to. It is simply not correct to assume that the swelling polymer has a constant refractive index throughout. However, even if we had recorded data over a range of wavelengths and angles to allow us to fit more Cauchy layers to represent a refractive index gradient through the swelling sample, the inherent ambiguity in the ψ and Δ data would make it extremely difficult to fit these layers, with any measurable confidence level, using conventional fitting techniques. These issues are discussed thoroughly in Chapter 5.

3.10 Rule of mixture analysis

Kwei and Zupko [92] suggest that the advancing front obeys the rule of mixture. That is:

$$x = (N_1 k_1' + N_2 k_2') t^{1/2} \tag{3.20}$$

where N_1 and N_2 are the mole fractions of the two solvents in the reservoir (the molar volumes of MEK and ethanol are 90.1 cm^3/mol and 58.5 cm^3/mol respectively) and k_1' and k_2' are the fit parameters to $x = kt^n$ assuming $n = 0.5$ for the pure solvents. We have not been able to extract k_1' and k_2' directly with the MRI and ellipsometry experiments here. However, we know that pure ethanol barely ingresses polystyrene, so we can assume that $k_1' = 0$. We can then make a best-fit of k_2' to $k' = N_2 k_2'$. The result of this fitting is shown in Figure 3.12. The best-fit compares reasonably well with the experimental values indicating that the rule of mixture applies to the data.

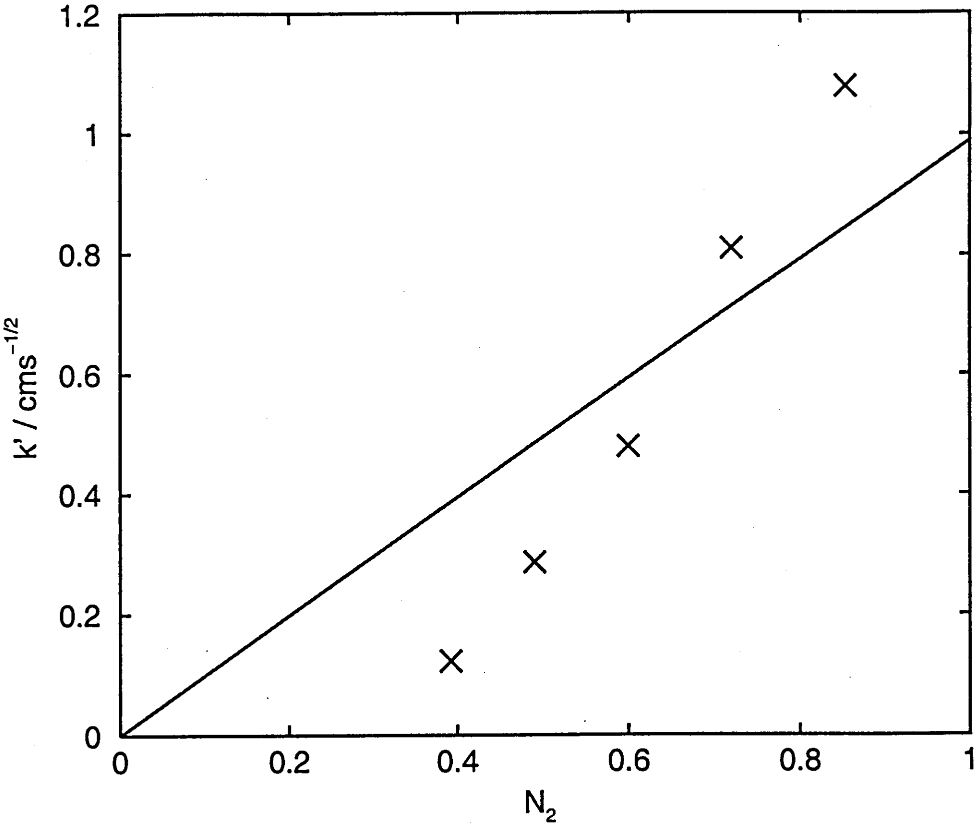

Figure 3.12: A best-fit of k_2' to $k' = N_2k_2'$. The experimental vales of k' are shown by the crosses

3.11 Conclusions

We have obtained the first data which provides separate spatially-resolved concentration information about the components of mixtures of good and bad solvents ingressing glassy polymer. For the system studied, MEK and ethanol ingressing polystyrene, the two solvents ingress together. However, the concentration profiles appear rather different. The good solvent exhibits a strong solvent concentration front whereas the poor solvent concentration varies smoothly and slowly across the swollen region. The effects can be explained in terms of a simple model wherein the poor solvent diffuses within the swollen rubber only by virtue of the presence of the good solvent. We have verified additionally that increasing the fraction of MEK in the reservoir increases the ingress rate according to the so-called rule of mixture. MRI and ellipsometry were found to be entirely complementary in their temporal and spatial resolution. However, fitting ψ and Δ ellipsometry data for Fickian ingress did not give entirely sensible results.

A paper describing the MRI experiments and modelling covered in this chapter has been submitted to *Macromolecules*.

Chapter 4

The effect of molecular weight on Fickian solvent ingress into glassy polymer

4.1 Introduction

The literature on the effects of polymer molecular weight on solvent sorption in polymers dates back to the 1950s. Studies have been made into both anomolous and Fickian diffusion. The conclusions are however contradictory. In 1953, Park [109] observed that when sorption kinetics were close to Fickian, methylene chloride ingressed polystyrene at a rate that was independent of the polymer molecular weight. A similar result was observed by Hutcheon *et al* for the diffusion of acetone into polyvinyl acetate. [110] These results were reinforced for a Fickian system by Tang *et al* in 1997 for ethylbenzene vapour ingressing monodisperse polystyrene with molecular weights well above that of the critical molecular weight (Mc). [111] Mc is the molecular weight above which the viscosity of the polymer changes as $Mw^{3.4}$. Below Mc, polymer viscosity varies linearly with

Mw. [112] Mc is a function of tacticity. [113] Conflicting results were obtained from gaseous carbon dioxide ingressing poly(dimethylsiloxane) (PDMS) with Fickian dynamics, which was reported to be dependent on polymer molecular weight. [114] A small decrease in ingress rate with increasing molecular weight was observed. However, although the molecular weights examined were above Mc, the PDMS was polydisperse with Mw/Mn of around 2.3.

The conclusions of experiments into Case II diffusion are similarly diverse. In 1971, in a study of the Case II system, n-pentane vapour ingressing polystyrene, Baird *et al* [115] explicitly considered not only the effects of polymer molecular weight on the ingress rate but also polydispersity and molecular orientation in the glassy polymer. They concluded that the ingress rate was neither a function of polymer molecular weight (even below Mc) or polydispersity. However, sorption was extremely sensitive to residual orientation in the polymer, with highly oriented films showing an ingress rate ten times that of annealed films. Umezawa *et al* [116] showed that the Case II solvent front velocity, when PS films were exposed to a fluorinated hydrocarbon vapour, was decreased with increasing molecular weight even far above Mc. For Case II transport of liquid methanol into monodisperse poly(methyl methacrylate), Hassan and Durning [117] observed no molecular weight dependence until well below the Mc. However, in a preliminary study, the same group did find a molecular weight dependence for the same system when the PMMA was polydisperse. [118]

In this chapter, further experiments, using ellipsometry and MRI, have been performed for the system of monodisperse polystyrene ingressed by mixtures of MEK (a thermodynamically good but kinetically bad solvent) and ethanol (a thermodynamically bad but kinetically good solvent) as a function of polymer molecular weight. The two techniques of MRI and ellipsometry are applicable for two different time and length scales. MRI is most suitable for relatively fast ingress rates, owing to its poor spatial resolution. Ellipsometry is faster and also has a higher spatial resolution, so it is suitable for slow ingress. MRI experiments were run for a mixture of 80vol% MEK and 20vol% ethanol in which the molecular weight of the polystyrene was varied from 10,000g/mol to 1,460,000g/mol. The polymer molecular weight effects on ingress were also probed using ellipsometry for pure ethanol ingress and a mixture of 20vol% MEK/ 80vol% ethanol. Experiments used Mw above and below the Mc for polystyrene which is 36,000 g/mol. [119] Additionally, the effects of orientation in the polymer stucture were examined using ellipsometry. For these experiments, crystallised isotactic polystyrene was ingressed by a mixture comprising 20vol% MEK/ 80vol% water. For comparison, unoriented atactic PS, with an identical thermal history, of similar molecular weight was ingressed by the same solvent mixture.

4.2 NMR microimaging data acquisition

4.2.1 Polystyrene sample preparation

Polystyrene powders with Mw= 9,860g/mol (Mw/Mn=1.04), 13,000g/mol (Mw/Mn=1.04), 50,400g/mol (Mw/Mn=1.03), 96,000g/mol (Mw/Mn=1.03), 325,000g/mol (Mw/Mn=1.04) and 1,460,000g/mol (Mw/Mn=1.06) (Polymer Laboratories Ltd., Church Stretton, UK) were made into pellets as described in the previous chapter. The temperature to which each sample was heated was dependent on PS molecular weight. The temperature range was 140°C to 200°C. The lower temperatures were used for lower Mw and hence lower T_g specimens so that samples were prepared at about the same temperature increment above their T_g.

4.2.2 ^{1}H data acquisition

The same MR acquisition parameters were used as in Section 3.3. Plots of half-height solvent front position against time for 80% MEK and 20% ethanol mixtures are shown below in Figure 4.1 The results of fitting the front positions to $x = kt^n$

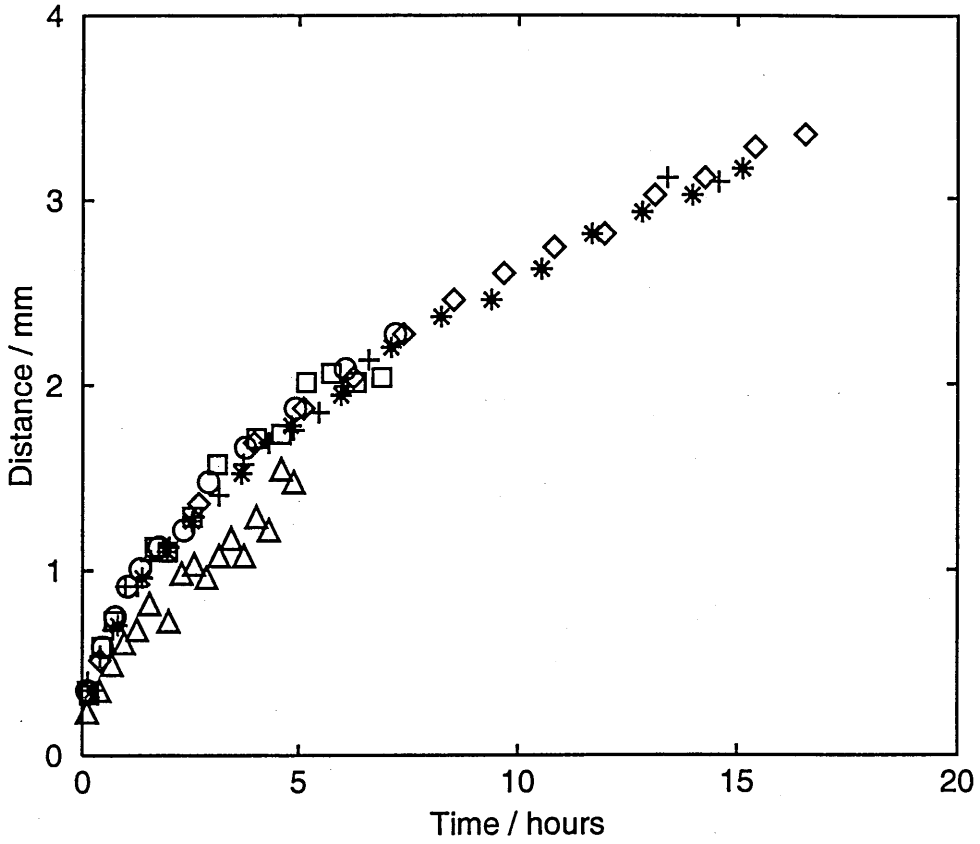

Figure 4.1: Half-height solvent front position of a mixture of 80% MEK and 20% ethanol ingressing PS. The symbols depict the different molecular weights as follows: 10,000g/mol (triangles), 13,000g/mol (squares), 50,000g/mol (pluses), 96,000g/mol (circles), 325,000g/mol (diamonds), 1,460,000g/mol (stars).

are shown in Table 4.1. The ingress rates, reflected in the value of k, for all the molecular weights are remarkably similar. Some deviation may be seen below Mc. However, at low molecular weight the swelling front position was harder to distinguish. This is demonstrated by comparing the profiles from ingress into Mw= 10,000g/mol shown in Figure 4.2 to those for ingress into 325,000g/mol

Table 4.1: The results of fitting $x = kt^n$ to the Mw varied experimental data

Mw/ gmol^{-1}	k	n
10,000	0.569	0.570
13,000	0.850	0.486
50,000	0.808	0.510
96,000	0.851	0.503
325,000	0.829	0.500
1,460,000	0.793	0.509

shown in Figure 3.2. In both of the molecular weight experiments shown, the border between the glass and the rubber is easy to distinguish, however, in the case of the Mw= 10,000g/mol experiment, the border between the liquid reservoir and the rubber region is difficult to make out. For the low molecular weight experiments sample preparation was also less reliable. At these molecular weights, during the pressing process, when molten, the PS is less viscous and flows more. It fills any tiny spaces in the press, sticking the unit tightly together. When it has solidified the low molecular weight PS is more brittle than the higher molecular weight samples. Because the PS is more strongly held to the press at low molecular weight it requires a larger force to extract. However, since it is more brittle, this larger force is more likely to damage the PS sample.

Clearly, ingress rate does not vary significantly with molecular weight above Mc and below Mc the slight indications of a change in ingress rate may be due to experimental error. For every sample a best fit was achieved for n close to 0.5. This indicates Fickian kinetics which are consistent with Chapter 3.

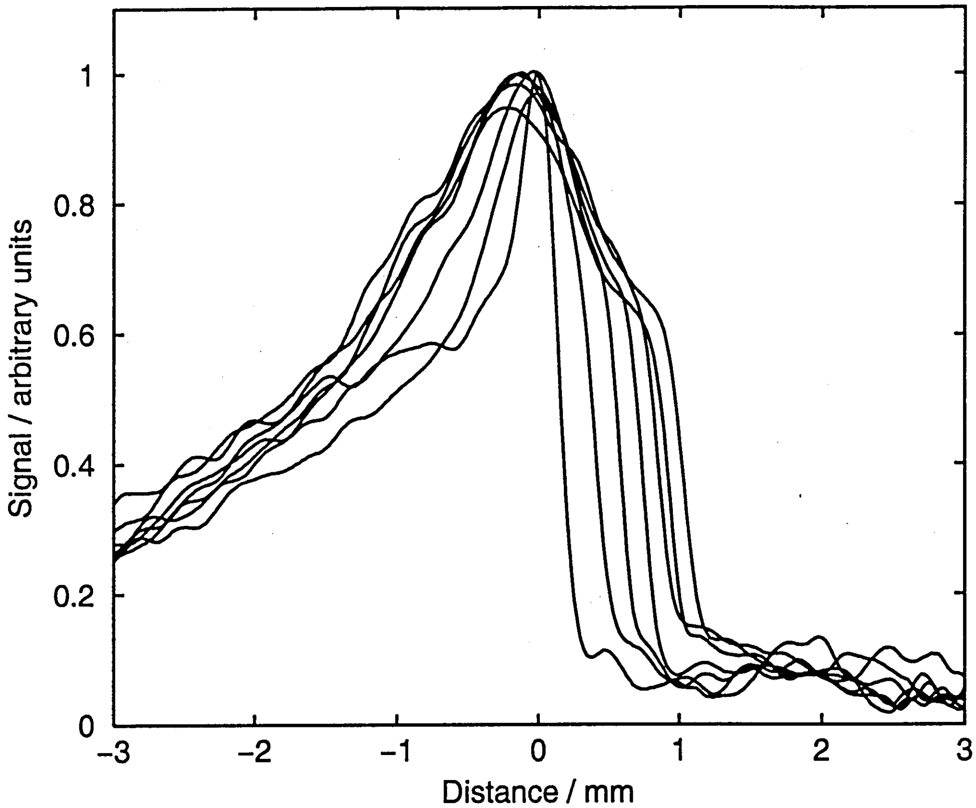

Figure 4.2: ^{1}H profiles of 80% MEK and 20% ethanol ingressing Mw= 10,000g/mol PS. The solvent is to the left, the progressively swelling rubber is in the middle and the glass is to the right. The original sample surface is at 0mm on the scale. In the first profile the change in gradient between the solvent reservoir and rubber region can be seen, however, in later profiles, this change is difficult to distinguish. Profiles are shown about 2.5 hours apart

4.2.3 ^{2}H data acquisition

Additional ^{2}H experiments to those performed with 325,000g/mol PS in the previous chapter were run with Mw= 50,400g/mol PS ingressed with a mixture of 80% MEK and 20% ethanol. The same deuterated solvents in the same fractions were used as in the previous chapter. The half-height front positions are shown in Figure 4.3 where they are compared to the Mw= 325,000g/mol results. The front positions of the different solvent components are clearly identical. The best-fits of these graphs to $x = kt^n$ are shown in Table 4.2. The relatively large deviation

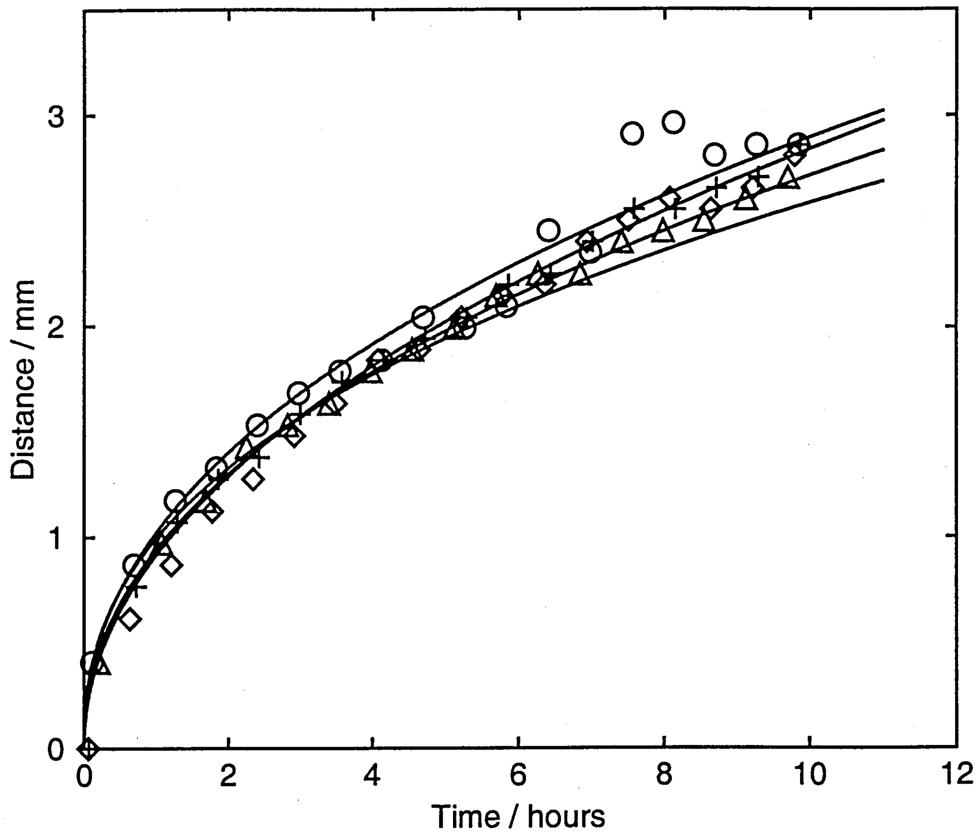

Figure 4.3: Half-height solvent front position of a mixture of 80% MEK and 20% ethanol ingressing PS in a ^{2}H MRI experiment where one or the other solvent has been selectively deuterated. The symbols show the following: 50,000g/mol PS and ethanol (diamonds), 50,000g/mol PS and MEK (triangles), 325,000g/mol PS and ethanol (pluses) and 325,000g/mol PS and MEK (circles). The solid lines show the best fits to the equation $x = kt^n$. For clarity, only alternate points are shown

from Fickian diffusion shown by the 325,000 g/mol sample ($n = 0.414$) are likely to be due to particularly large changes in temperature during the experiment caused through problems with the gradient set cooling unit. Again, ingress rate is seen not to vary significantly with polymer molecular weight, even when close to Mc. Deviations can be attributed to experimental error.

Table 4.2: The results of fitting $x = kt^n$ to the experimental deuterated solvent data.

Mw/ gmol^{-1}	Solvent	k	n
50,000	MEK	1.025	0.451
50,000	ethanol	0.917	0.491
325,000	MEK	0.997	0.414
325,000	ethanol	0.946	0.458

4.3 Ellipsometry data acquisition

To further explore the molecular weight effects a further set of experiments were performed on solvent ingress using ellipsometry.

4.3.1 Solvent ingress in amorphous polymer films

Films were prepared as described in the previous chapter for Mw= 50,400g/mol, 72,000g/mol, 195,000g/mol, 325,000g/mol, 696,500g/mol and 1,290,000g/mol. As before we tried to make film thicknesses of around 3000Å. Of course, film thickness, when spin coating, is a weak function of polymer molecular weight [120], but the effects were not seen to be too great in the molecular weight range studied. All of the samples except Mw= 50,400g/mol were then heated in a vacuum oven at 180°C for 24 hours. If the molecular weight of the PS is too low when heated, it dewets from the silicon substrate. Molecular weights below 50,400g/mol could not be studied as the PS film dewetted from the substrate at these low molecular weights even without heating. The purpose of heating the polymer is to allow it to become homogeneous, removing any molecular order formed during the spin coating process. For the ingress of pure ethanol and

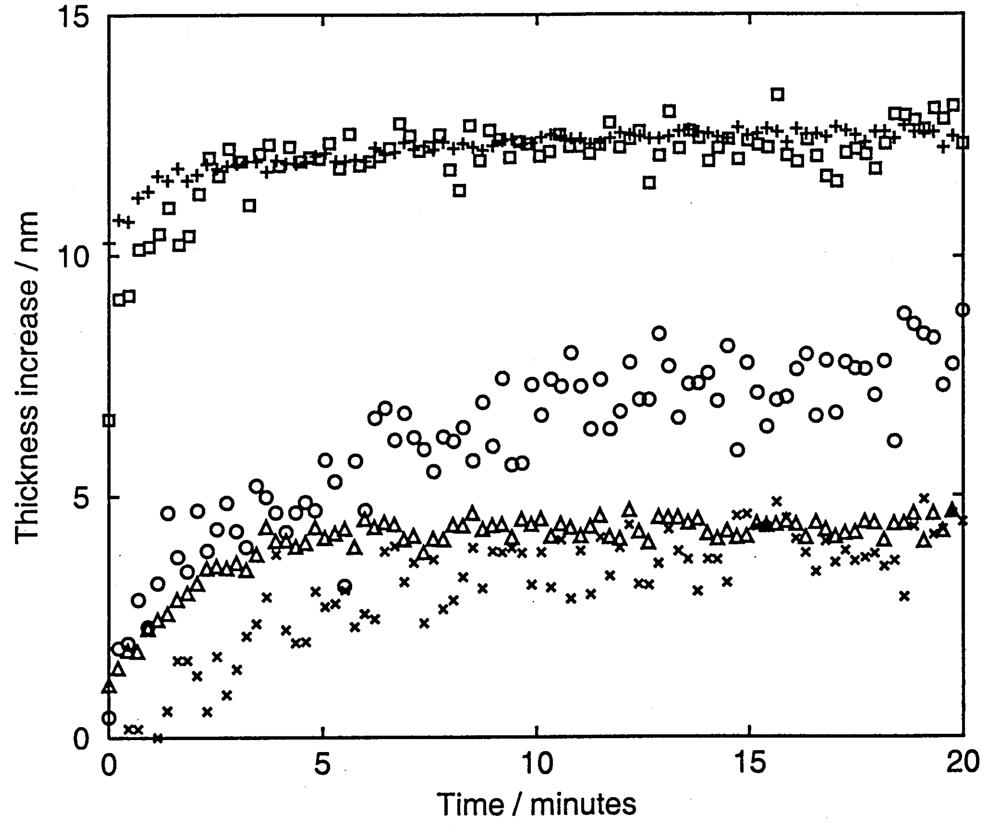

Figure 4.4: The amount of swelling of PS of varying molecular weight being ingressed by pure ethanol as a function of time. This measurement has been made using ellipsometry. The triangles are Mw= 195,000g/mol, the crosses and circles are Mw= 325,000g/mol, the squares are Mw= 696,500g/mol and the pluses are Mw= 1,290,000g/mol

a mixture of 20% MEK/ 80% ethanol respectively, the thickness of the samples as the PS molecular weight is varied is shown in Figures 4.4 and 4.5. It should be mentioned that at low molecular weight (72,000g/mol) the PS has been seen to craze during ingress and thus gave ingress ψ and Δ data that could only be fitted with large errors. Hence, these results are not shown. This phenomenon is due to the increased brittleness of low Mw polystyrene. There appear to be some differences between the different molecular weights. Refering first to the pure ethanol ingress in Figure 4.4. The high molecular weight samples (Mw= 696,500g/mol and Mw= 1,290,000g/mol) appear to be extremely similar. They

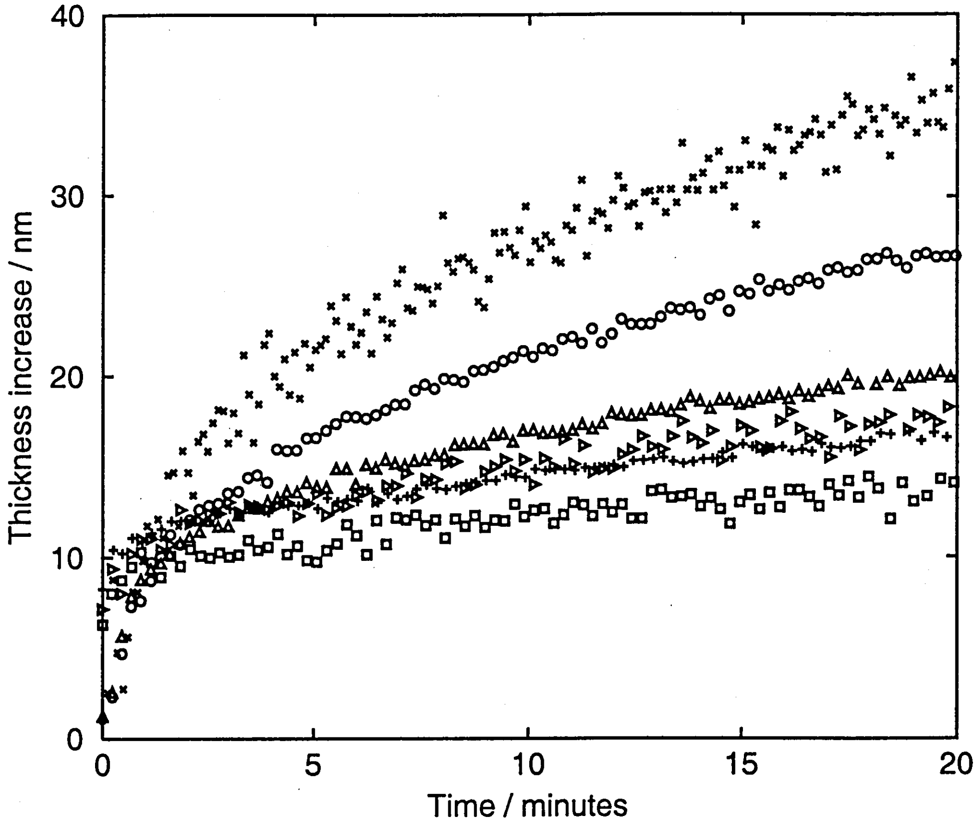

Figure 4.5: The amount of swelling of PS of varying molecular weight being ingressed by a mixture of 20% MEK and 80% ethanol as a function of time. This measurement has been made using ellipsometry. The up triangles are Mw= 195,000g/mol, the crosses and circles are Mw= 325,000g/mol, the squares and right triangles are Mw= 696,500g/mol and the pluses are Mw= 1,290,000g/mol

show an almost instantaneous swelling before ingress is largely halted. The lower Mw samples have a much more gradual increase in thickness and the eventual equilibrium thickness is much lower (roughly half) that of the higher Mw samples. Overall, although ethanol is a bad solvent we observe a small amount swelling indicative of solvent ingress. Best-fits were made to $x = kt^n$ at short times, but the results were not reasonable, with values of n considerably less than 0.5. For the ingress of 20% MEK/ 80% ethanol (shown in Figure 4.5) the change in thickness of all the different molecular weight samples appears to be a two-stage process. For the first minute, there is rapid increase in film thickness. After this time, the ingress slows apparently instantaneously and we observe relatively slow and decelerating ingress until equilibrium. There is no obvious pattern relating ingress rate to molecular weight for the 20% MEK samples. The overall swelling, both in depth and time, is greater for the 20% MEK sample than compared to the pure ethanol. The inability to fit $x = kt^n$ meaningfully can be attributed to the fact that the single layer Cauchy model we use is not good enough for the refractive index gradient we expect for Fickian diffusion. However, it is reasonable to expect that, even if the model to fit ψ and Δ is wrong, if there were no molecular weight effects on solvent ingress then the fitted film thickness increase versus time graphs would be the same. One explanation that could describe these apparent molecular weight effects is residual oriention of the polymer chains. Spin coating, is known to order thin films. [121, 122] Although, an annealing strategy was chosen that was thought to relax all orientation in the film, this may not necessarily be the case. The research of Bray and Hopfenberg [123] has shown that subtle differences in residual orientation in films can result in different sorption rates. Longer polymer chains take longer to relax, so increased sorption rates due to increased orientation, will be observed for higher molecular weights. The effects of orientation have not been observed in our MRI experiments because their effects are only seen up to 10μm from any substrate. [124] In addition, this distance is for high molecular weight polymers, in lower molecular weight samples orientation is only observed up to 1μm.

4.3.2 Solvent ingress in crystallised polymer films

In Section 4.3.1 it was mentioned that some apparent polymer molecular weight effects on solvent ingress have been attributed to different levels of orientation in the polymer. In this section a comparison is made between highly oriented PS films and largely unoriented PS when ingressed by a mixture of 20%MEK and 80% deionised water. To achieve high levels of orientation in a PS film isotactic

PS (iPS) is used as opposed to the atactic PS (aPS) discussed elsewhere in this thesis. The ordered structure along the molecule means that, unlike aPS, iPS will crystallise after melting and slow cooling. [112]

A brief introduction to polymer crystallisation

A crystal may be defined as a portion of matter within which the atoms are arranged in a regular, repeated, three-dimensionally periodic pattern. From early X-ray diffraction work, it is known that polymers never crystallise to 100%. In 1938, Storks [125] introduced the idea of chain folding. He concluded that the chains of semi-crystalline polyisopropene had to fold back and forth. This hypothesis, however, went unnoticed by the scientific community. Later, in 1957, three independently published papers by Keller [126], Till [127], and Fischer [128], reported that single crystals were 10nm thick and that the polymer chain direction lies transverse to the plane of the lamellae. Finally, Keller postulated chain folding to explain why crystal lamellae were very much thinner than the length of polymer chains. [112] The visible microstructural units of crystalline bulk polymers are normally spherical spherulites. [1] These are complicated assemblies of chain-

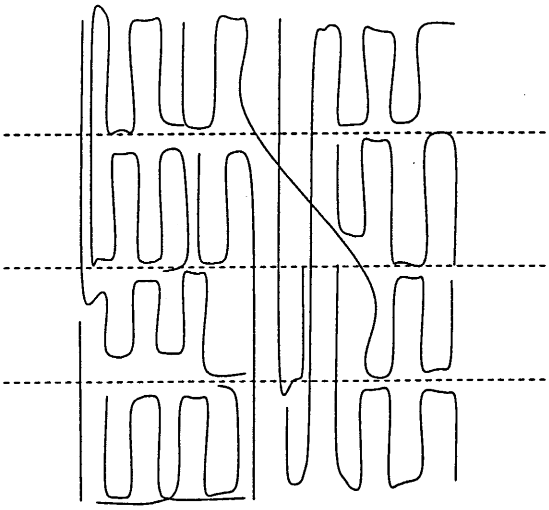

Figure 4.6: Chain folding in semi-crystalline polymer. The dashed lines show the divisions between lamellae

folded lamellar units. [1]

Experimental method

Monodisperse aPS and iPS of comparable molecular weight (Mw= 696,500g/mol (Mw/Mn= 1.05) and Mw= 752,000g/mol (Mw/Mn= 1.75) respectively) were obtained from Polymer Laboratories Ltd., Church Stretton, UK. These were prepared in a similar way as described earlier but with a lower weight fraction of polystyrene dissolved in the cyclohexanone (2wt%). Again, the samples were heated after spin coating at 180°C for 24 hours. This heating protocol not only allowed enough time and heat to remove any residual cyclohexanone but there was also plenty of time for complete crystallisation of the iPS. [129] Different annealing strategies and even different substrate materials will form crystals with different structures and at different rates. [129, 130] Each sample was viewed under an optical microscope to confirm crystallisation. A typical crystallised sample is shown in Figure 4.7. The extent of the spherulites can be clearly seen. An initial spectroscopic multiple angle ellipsometric scan was made of each of five iPS and five aPS samples. The thickness of the PS film was typically found to be around 900Å. The polystyrene samples were placed in the same ellipsometry cell as described in Chapter 3. Scans of ψ and Δ as a function of time were made at a wavelength of 500nm, initially without the solvent. Then, after a minute or two, the MEK/ water mixture was quickly added. The ψ and Δ data were fitted to a three layer model as before.

Results

The percentage change in thickness against time for typical aPS and iPS samples are shown in Figures 4.8 and 4.9. The results for the five iPS and five aPS samples are not entirely reproducible. A general trend is that the iPS samples

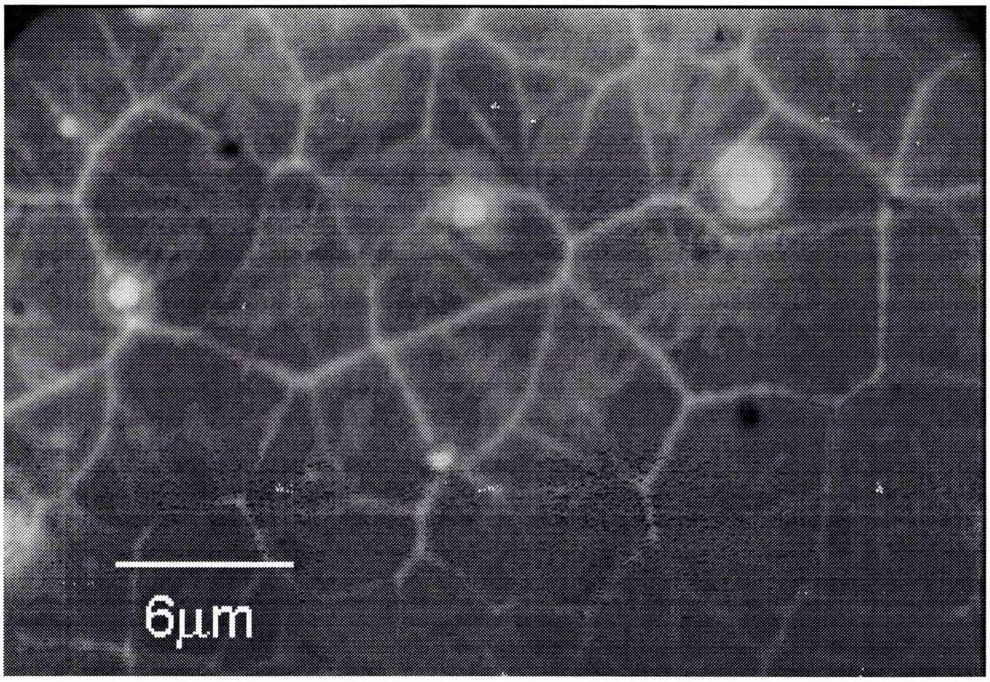

Figure 4.7: An optical micrograph of iPS crystals on a silicon substrate. The border between each sperulite is shown bright. The spherulites are similar in size (approximately 6μm in diameter)

swelled more than the aPS samples (on average 10% compared to 5%). Both types of PS took a similar range of times to reach their maximum equilibrium thickness (between 20 and 40 minutes). However, it is difficult to say which swelling mechanism is active. After correcting so that the ingress started at zero time, fits of the complete data sets to $x = kt^n$ did not give a meaningful best-fit. Typically, values of n were about 0.2. Fixing $n = 0.5$ and fitting only k gave very poor fit quality. If one assumes that ingress is linear at short times, then the iPS samples have a front velocity three times faster than the aPS samples (0.3 nm/s compared to 0.1 nm/s). Looking again at Figures 4.8 and 4.9 and one notices another difference between the two samples. The iPS appears to have two changes of gradient (at about 10 minutes and at about 30 minutes after the experiment was started) whereas the aPS sample is a single smooth curve. We propose that in the iPS there are two different ingress rates. Refering back to the structure

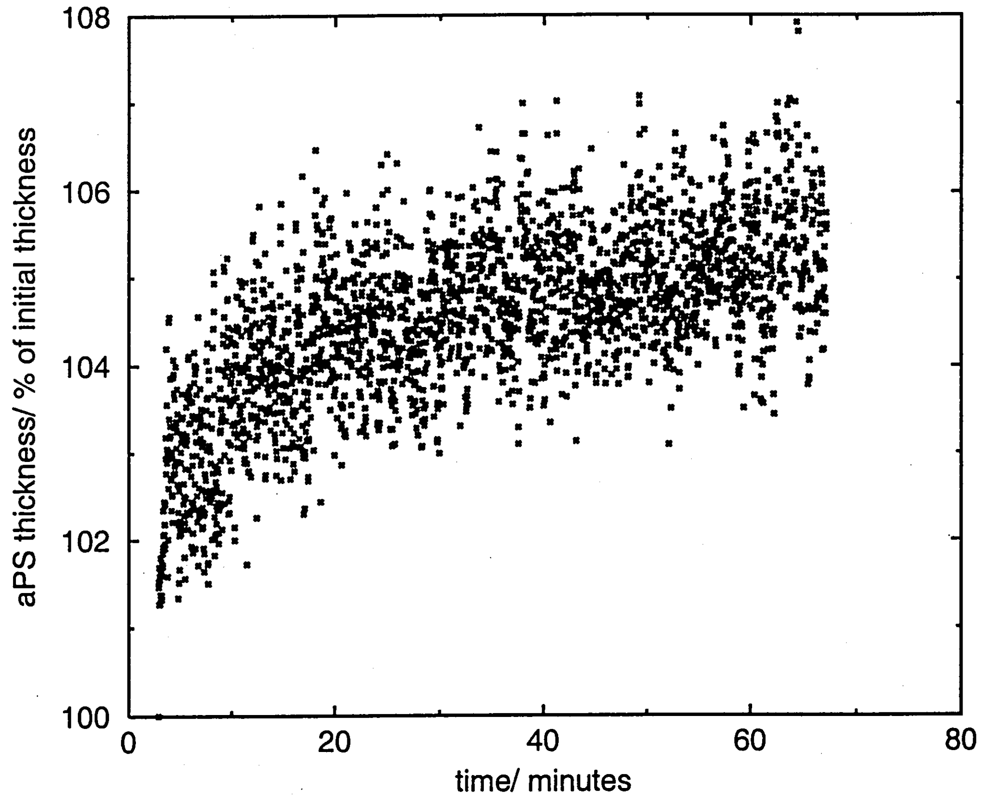

Figure 4.8: A graph of the percentage swelling against time of a typical aPS sample. Time zero represents when the ellipsometry scan was started and not when the solvent was added to commence ingress. The solvent was added after three minutes.

of crystallised polymer in Figure 4.6 and one can see that there are two areas of different polymer chain density. In between the folded chains and between lamellae there is a low density of amorphous polymer chains. These pathways will allow quick ingress, like that in the first five minutes of ingress. However, ingress through the crystallised densely packed folded chains is a slower process shown by the distinct change of gradient. On the other hand, the aPS sample has a homogeneous polymer chain density throughout the sample giving the single ingress regime. Overall, this result is not inconsistent with the observations of Baird *et al.* [115] in that polymer swelling is increased when the polymer structure is oriented.

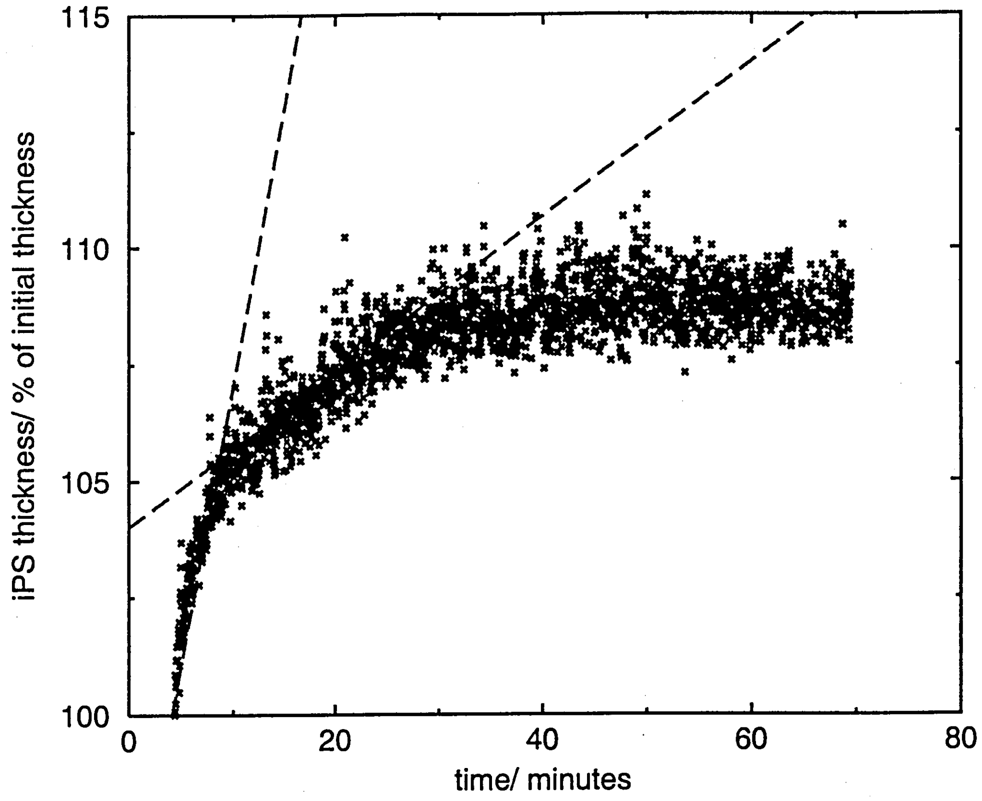

Figure 4.9: A graph of the percentage swelling against time of a typical iPS sample. The iPS thickness is shown by the crosses. Time zero represents when the ellipsometry scan was started and not when the solvent was added to commence ingress. The solvent was added after five minutes. The dashed lines are guides to the eye to show the change of gradient that we suggest is caused by quick ingress through the low density amorphous polymer chains and slow ingress through densely packed folded polymer chains

4.4 Further work on the effects of polymer order

An obvious addition to this work would be to perform measurements on bulk crystallised iPS samples using MRI. However, attempts to make bulk samples failed. iPS has a considerably higher melting point than aPS, and a bulk sample could not be made to melt with readily available heating and pressure equipment. With a very thin layer on a silicon substrate, crystallisation occurs at around 180°C and this temperature limit is not a problem. A more subtle experiment could be performed with MRI using not a spin-echo NMR image but a double quantum filtered image. [131, 132, 133]

This imaging technique gives contrast to the level of molecular ordering in spin $I = 1$ systems. Using this technique one could witness the change in the molecular structure during swelling rather than simply a change in thickness. Deuterated solvent or polymer would have to be used. This pulse sequence was successfully implemented with the in-house built deuterium probe. We also tried to implement it in the stray field. However, this proved unsuccessful. Unfortunately, without good bulk crystallised iPS samples, no reliable DQF experiment on ordered polystyrene could be attempted. Experiments with the lamellar liquid crystal phases of soap have however been done successfully at Surrey with the DQF pulse sequence. The use of ellipsometry is problematic in that we are unable to fit Fickian ingress data easily and meaningfully. Progress into overcoming this problem is covered in Chapter 5.

4.5 Conclusion

Fickian solvent ingress into polystyrene does not appear to be a function of polymer molecular weight. Reports in the literature which are contrary to this may be attributed to varying levels of orientation in the different molecular weights of polymer studied.

Chapter 5

Improved methods for extracting film thickness and refractive index information from ellipsometry

One explanation for the poor quality of fitting to the ellipsometry data sets discussed so far in this thesis, is that the model we assume, a single swelling layer with a uniform refractive index, is an over simplification. For Fickian ingress one would expect the refractive index to vary through the sample, representing the changing solvent concentration. One could of course try to fit thickness and refractive index values to a large number of very thin layers or indeed a continuous distribution. [134] However, using the Levenberg-Marquardt algorithm, one would become stymied by the ambiguity inherent in ellipsometry data (discussed in Section 2.4.4). There would be no guarantee that the refractive index profile gave the global minimum in the error between the experimental data and the model fit. Two methodologies have been developed to try to alleviate this problem. The first, proposed by Charmet and de Gennes [135] uses a series of approximations so that ellipsometry ψ and Δ data from an arbitrary refractive index profile can be inverted directly without fitting. The second, developed at Surrey, is a Bayesian inference analysis that uses simulated annealing (SA) to find candidates for the global minimum in the least-squares fit to the ellipsometry data and a Markov chain Monte-Carlo (MCMC) method to find the most probable solution when there is more than one candidate for global minimum in the error between the model fit and experimental data.

5.1 The Charmet and de Gennes formulae for an inhomogeneous layer with arbitrary refractive-index profile

5.1.1 The mathematical background

For thin films with a maximum thickness $z_{max} < \lambda/4\pi$ where λ is the wavelength of the incident light, Charmet and de Gennes [135] express the reflection coefficients in terms of the Fourier transform of the tested sample's index profile, $\Gamma(2q)$ where q is the normal component of the incident wave vector defined as $q = (2\pi/\lambda)n_0 \cos\phi_0$ where ϕ_0 is the angle of the incident beam and n_0 is the ambient refractive index. In an ellipsometry experiment many incident angles can be used, to give a range of q values. Thin layers are treated as a perturbation $|\delta n/n_0| < 1$. In their paper, Charmet and de Gennes derive an equation for ellipticity in terms of Γ that is written as:

$$\rho = \tan\psi e^{i\Delta} = \frac{r_p}{r_s}[1 + iA\Gamma(-2q) + iB\Gamma(2q)] \tag{5.1}$$

where

$$A = a(r_p^{-1} - r_s^{-1}) - br_p^{-1};\ B = a(r_p - r_s) - br_p^{-1} \tag{5.2}$$

where

$$a = n_0(\omega/c)^2 q^{-1};\ b = 2n_0^{-1}q. \tag{5.3}$$

r_p and r_s are given by the familiar Fresnel equations [81],

$$r_s = \frac{n_0 \cos\phi_0 - n_2 \cos\phi_2}{n_0 \cos\phi_0 + n_2 \cos\phi_2} \tag{5.4}$$

$$r_p = \frac{\frac{n_0}{\cos\phi_0} - \frac{n_2}{\cos\phi_2}}{\frac{n_0}{cos\phi_0} + \frac{n_2}{cos\phi_2}}. \tag{5.5}$$

n_2 and ϕ_2 are the refractive index of the substrate and the complex angle of refraction respectively. In practise, n_2, is usually known or it can be measured with ellipsometry before a coating is applied. ϕ_2 can be calculated from Snell's law [81] i.e.

$$n_2 \cos\phi_2 = n_0 \cos\phi_0. \tag{5.6}$$

The Fourier transform for the index profile is

$$\Gamma(k) = \int_0^\infty dz\delta n(z)e^{ikz}. \tag{5.7}$$

In the sample thickness limit $z_{max} < \lambda/4\pi$ one can expand e^{ikz} as:

$$e^{ikz} = 1 + ikz + \frac{(ikz)^2}{2!} + \ldots \tag{5.8}$$

hence

$$\Gamma(2q) = \Gamma_0 + 2iq\Gamma_1 + \frac{(2iq)^2}{2!}\Gamma_2 + \ldots \tag{5.9}$$

where

$$\Gamma_n = \int_0^\infty dz z^n \delta n(z) \tag{5.10}$$

representing successive moments of the index profile. The latter terms in Equation 5.9 can be neglected because one does not expect oscillations or a sudden jump in the refractive index profile. A Gaussian or exponential type decay is expected. Therefore to find the refractive index profile write

$$Z(q) = \frac{R_p}{R_s}\frac{r_s}{r_p} = \frac{\tan\psi e^{i\Delta}}{\tan\psi_0 e^{i\Delta_0}} = Z' + iZ''. \tag{5.11}$$

Z' and Z'' are respectively the real and imaginary parts of Z. Substituting Equation 5.9 into 5.1 gives

$$Z(q) = 1 + i(A+B)\Gamma_0 + 2q(A-B)\Gamma_1 - 2iq^2(A+B)\Gamma_2 + \ldots. \tag{5.12}$$

Assuming that r_s and r_p are real, then A and B are also real. Hence

$$\frac{Z'(q)-1}{A(q)-B(q)} = 2q\Gamma_1 + \ldots = F \tag{5.13}$$

and

$$\frac{Z''(q)}{A(q)+B(q)} = \Gamma_0 - 2q^2\Gamma_1 + \ldots = G. \tag{5.14}$$

By plotting F and G versus q one can deduce the moments Γ_0 and Γ_1. Charmet and de Gennes [135] then define an effective thickness, e_{eff} of a layer as

$$e_{eff} = \frac{2\Gamma_1}{\Gamma_0}. \tag{5.15}$$

Charmet and de Gennes say that they include the factor of two so for a homogeneous slab of thickness s, $e_{eff} = s$. An IDL program was written to implement Equations 5.1 to 5.6, 5.11 and 5.13 to 5.15. The algorithm was tested firstly using simulated data and then real ellipsometric data.

5.1.2 Testing the algorithm with simulated data

The most simple sample structure was chosen to test the Charmet and de Gennes algorithm, that is, a single uniform transparent film on a transparent substrate. A set of simulated ψ and Δ data was created for a range of thickness and refractive index values. A range of q values corresponding to $0° < \phi_0 < 90°$ were used. Here the example of a semi-infinite substrate with a refractive index of 1.50 and a thin film 10nm thick with refractive index 1.45 is illustrated. In Figures 5.1 and 5.2 plots of F and G versus q can be seen. Γ_1 is found from the gradient of F and Γ_2 is found from intercept of G when $q = 0$. In this case, the thin layer thickness is found to be 9.35nm when we neglect the factor of two given by Charmet and de Gennes in Equation 5.15. The value of the thickness of the layer compares favourably to the actual value (10nm) used in the data simulation.

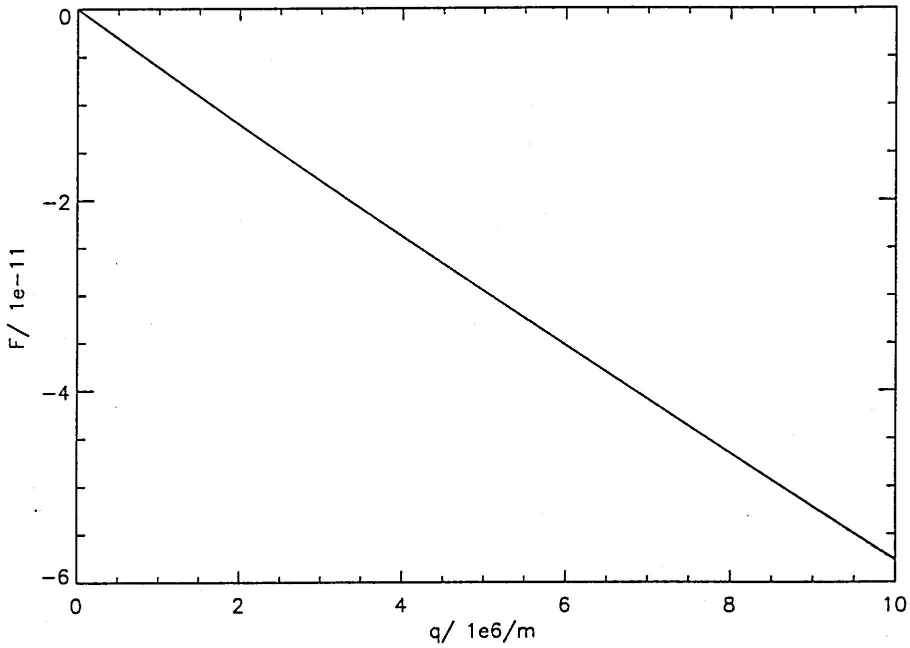

Figure 5.1: A plot of F (defined in the text) plotted against the normal component of the incident wave vector q obtained from simulated data for a 10nm thick film with refractive index 1.45 on a substrate with a refractive index of 1.50.

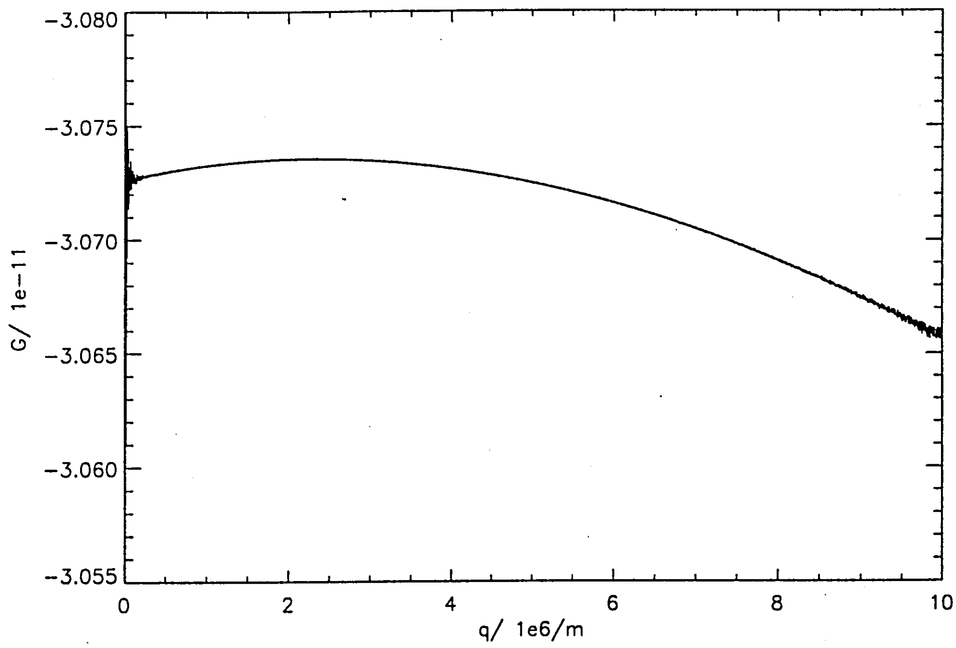

Figure 5.2: A plot of G (defined in the text) plotted against the normal component of the incident wave vector q obtained from simulated data for a 10nm thick film with refractive index 1.45 on a substrate with a refractive index of 1.50.

Charmet and de Gennes give no mathematical reason to include the factor of two in Equation 5.15. They merely hypothesise that they must include it to return the correct thickness value! Since we find that this term is unnecessary, we can only conclude that it is a mistake on their behalf. Using the same refractive indices for the substrate and film but varying the film thickness and the wavelength of incident light for $z_{max} < \lambda/4\pi$ the errors in thickness are generally less than 10%. Figure 5.3 shows this error (expressed as a percentage difference between e_{eff} and z_{max}) for three different incident wavelengths. These simulations were performed for the full range of q values. Experimentally, however, it is impossible to measure q at the extremes. $20° < \phi_0 < 85°$ is a realistic experimental range. For this range, the error grows to 20% for thicknesses close to $\lambda/4\pi$. These results for simulated data are extremely promising. Table 5.1 shows the ranges of refractive indices that give a 20% error when analysing simulated data with the Charmet

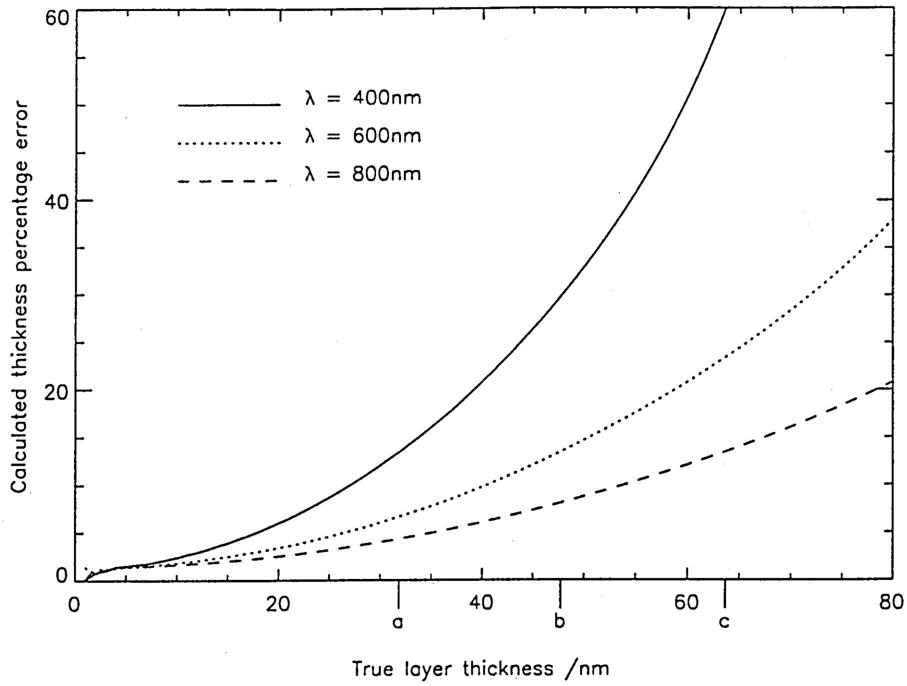

Figure 5.3: The errors obtained after applying the Charmet and de Gennes with $n_1 = 1.45$ and $n_2 = 1.50$ at wavelengths of 400nm (the continuous line), 600nm (the dotted line) and 800nm (the dashed line). On the horizontal axis a,b and c show the limit of applicability of this algorithm ($z_{max} < \lambda/4\pi$) for the aforementioned wavelengths

and de Gennes algorithm. The sample is a 10nm thick film on a semi-infinite substrate in air with $\lambda = 600$nm. Most organic materials have a refractive index between 1.35 and 1.6. Therefore, the thicknesses of most polymers on a glass or polymer substrate could be determined. However, real samples will always have some kind of imperfection, such as surface roughness. Moreover, noise in the data could affect the quality of the inversion.

5.1.3 Testing the algorithm with real ellipsometry data

Poly(methyl methacrylate) (PMMA) was dissolved in boiling acetone and then spin cast onto a thick glass substrate. Scans were performed using the University of Surrey ellipsometer using incident wavelengths of 400, 600 and 800nm and

Table 5.1: Ranges of refractive indices where the errors of the Born approximation result in an error less than 20% when determining the thickness of a 10nm transparent layer on a transparent substrate in air with $\lambda = 600$nm

Film index	Substrate index	Index range
1.4	Varied	1.33-1.47
1.5	Varied	1.47-1.68
1.6	Varied	1.52-2.0
Varied	1.4	1.35-1.45
Varied	1.5	1.41-1.52
Varied	1.6	1.46-1.57

angles between 20° and 85° in 0.1° increments. These data were fitted using the LM algorithm, and a thickness of 18.7nm was obtained. Scans had already been made on the substrate before the PMMA was deposited in order to determine the optical constants of the substrate.

The Charmet and de Gennes analysis on the experimental data could not produce a meaningful result. Looking at the ellipsometry data from the bare substrate provided an explanation for this problem (see Figures 5.4 and 5.5). This scan did not give a perfect step function in Δ that one would expect for a semi-infinite slab (as described in Section 2.4.5) and neither did ψ go to zero at the Brewster angle. There are two explanations for this result. Either the glass slab was contaminated or the ellipsometer acquisition was not accurate enough. Either or both of these explanations are probable. Without a compensator [136] the ellipsometer is subject to errors at low values of ψ. A limitation with the University of Surrey ellipsometer is that, since it uses a rotating analyser to measure the light polarization state, it cannot give the sign of the imaginary component of ρ. This means that Δ can only be measured between 0° and 180°.

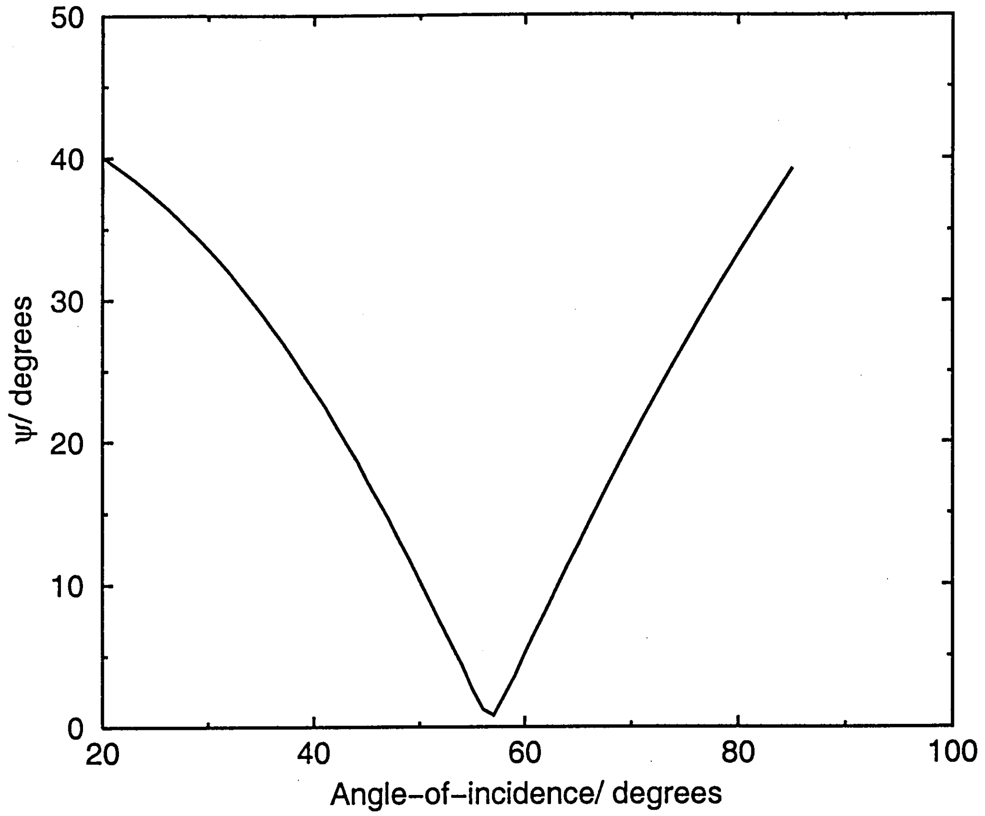

Figure 5.4: ψ as a function of angle-of-incidence for a glass slab measured using the University of Surrey ellipsometer

Similar samples were then analysed using a compensator-equipped ellipsometer at J.A. Woollam, Lincoln, Nebraska, USA which allows Δ to be measured over the full range from 0° to 360°. The results of these scans on the uniform glass slab are shown below in Figures 5.6 and 5.7. The values of ψ still do not at any point go to zero, and the Δ curve is still some way from being a step function. One of the assumptions of the Charmet and de Gennes model is therefore violated. A meaningful inversion of data from a polymer coated glass sample could not be obtained with this technique. Without evidence for a semi-infinite substrate, the technique is not valid.

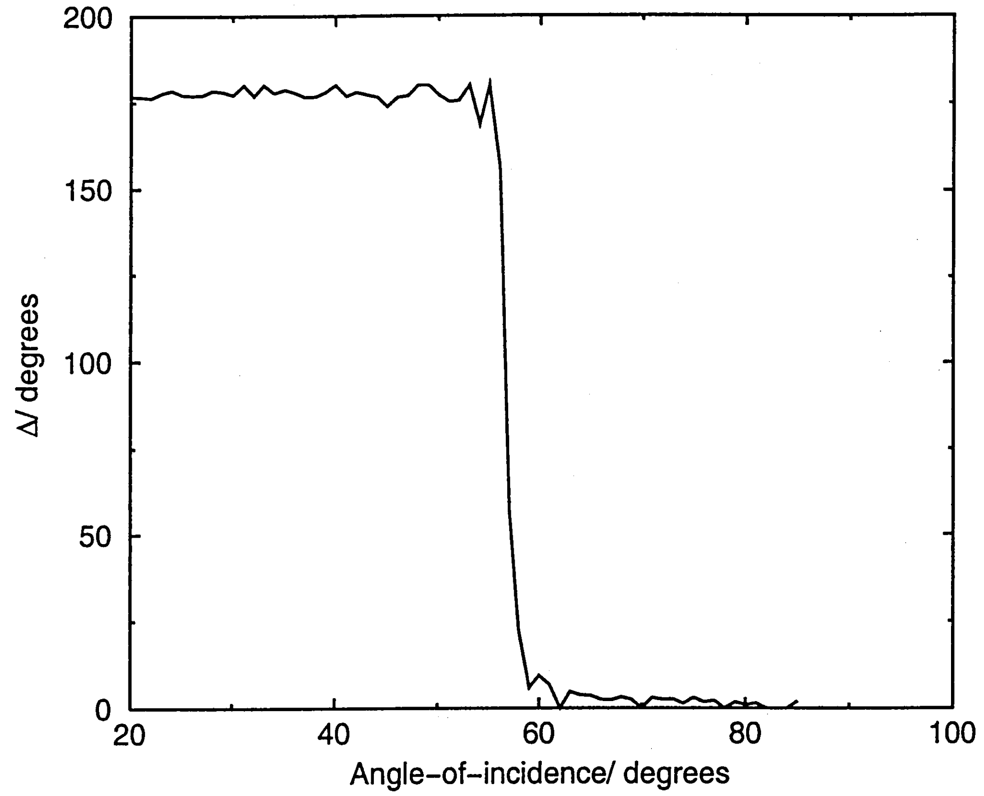

Figure 5.5: Δ as a function of angle-of-incidence for a glass slab measured using the University of Surrey ellipsometer

5.1.4 Discussion

The thin layer approximation version of the Charmet and de Gennes inversion technique works well for noise-free simulated data. However, even with a clean, flat glass substrate real ellipsometry data cannot be inverted. For the type of solvent ingress experiment described earlier, this technique has further flaws. The approximations given here are valid only for samples with a maximum thickness, $z_{max} < \lambda/4\pi$. The maximum value of λ typically available is say 1000nm (into the infra red range), suggesting the biggest swollen thickness measureable is around 80nm. This is fine for looking at the early stages of a Fickian precursor in a Case II system but nothing more. Charmet and de Gennes do also suggest an inversion process that does not make a thin layer assumption, however, an implementation

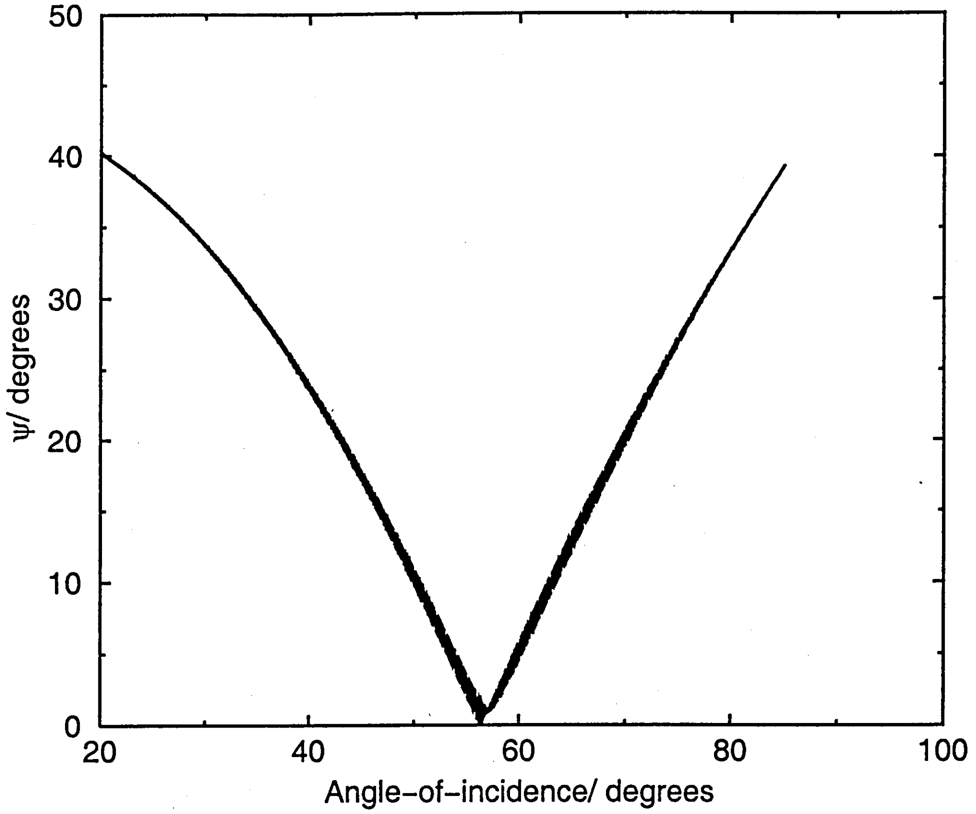

Figure 5.6: ψ as a function of angle-of-incidence for a glass slab measured using the J.A. Woollam ellipsometer

of this methodology either by us or by others [137] has not been successful. An additional limitation with these analyses is that they require an angular scan to obtain a range of q without the complications of optical dispersion. Since angular scans need movement of the light source and analyser arms, they are rather slow. Poor temporal resolution would be achieved.

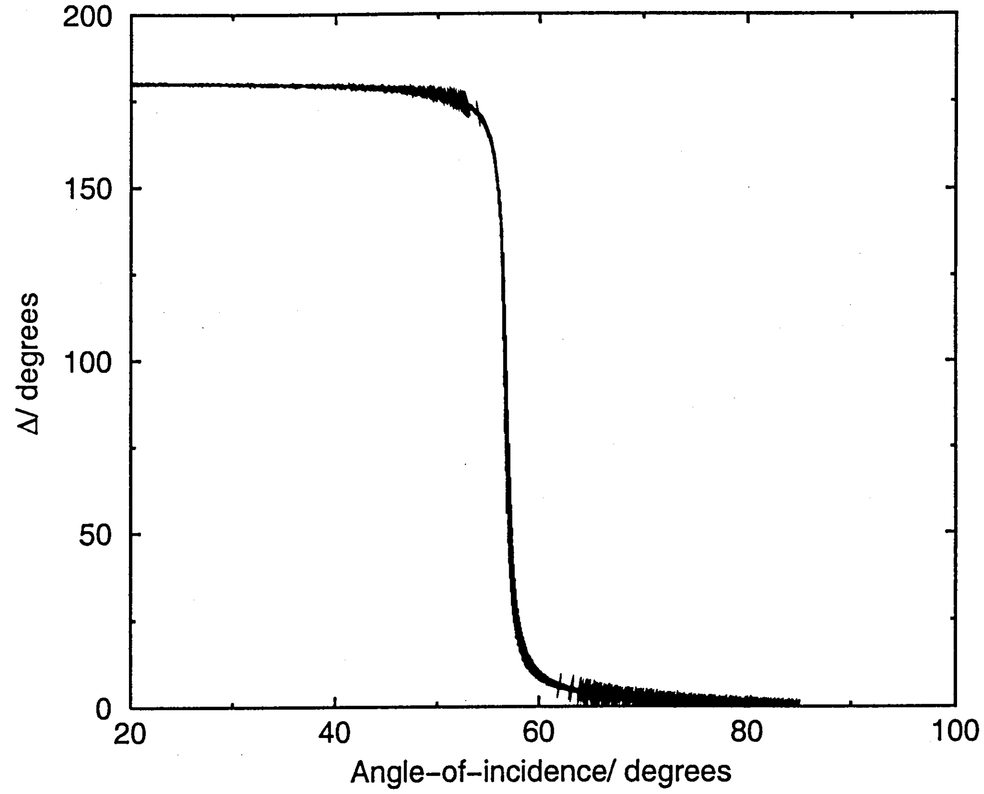

Figure 5.7: Δ as a function of angle-of-incidence for a glass slab measured using the J.A. Woollam ellipsometer

5.2 The Bayesian inference analysis of ellipsometry data

5.2.1 Introduction

Given the limited success of the Charmet and de Gennes method, the following Bayesian inference method was developed. The aim again is to produce what is effectively a model-free inversion method. Firstly, simulated annealing is used to perform a least-squares multi-parameter fit to the ellipsometry data. SA is a global optimisation algorithm. Hence, it has the advantage over LM in that a good initial guess of the fit parameters, giving a value of error close to the global minimum (or indeed maximum) of the error function, is not required.

No assumptions need to be made about the physical structure of the measured sample. However, SA is a stochastic technique. It will only find one possible structure if there is no more than one structure that fits the data. To overcome this limitation, Bayesian inference has been applied. This is the only way to consistently treat incomplete and noisy data when additional prior information is known. It is realised using the MCMC algorithm. This algorithm can explore solution space in its entireity to find every possible solution consistent with the ellipsometry data. In this section, the SA-MCMC is implemented and tested for the simple case of a bilayer on a semi-infinite substrate for real ellipsometry data. However, the algorithm could be generalised for a system of m unknown layers where m is an unknown parameter.

5.2.2 The mathematical background to SA

SA [138, 139] is based on an analogy with the thermal annealing of crystals where defects are removed by heating the crystal and then cooling it very slowly. Let us assume that the current state i of a system has energy E_i. Another state j, slightly different from i and with energy given by E_j, is generated by a random process. If $E_j < E_i$ then the system is taken to be in the new state j. Furthermore, if $E_j > E_i$ then the transition can still occur with probability given by the Boltzmann factor

$$P(i \to j) = \exp \frac{-(E_j - E_i)}{k_B T}, \tag{5.16}$$

where T is the absolute temperature and k_B is the Boltzmann constant. If the initial temperature is high enough, if at each temperature the system is given long enough to reach thermodynamic equilibrium, and if the cooling rate is slow enough, then at T=0K the system will be in any one of the minimum-energy states. In the SA analogy the energy becomes the error between the measured ellipsometry spectra and the spectra produced by the current N and d parameters.

T is redefined as a control parameter, and the constant k_B can be neglected. At high T values, practically all transitions are accepted (*c.f.* a liquid state with high entropy). As T decreases, the probability of transitions decreases so that when T is very small only transitions that lead to a decrease in error are accepted. In SA, T is initialised at a high value, T_0 and then slowly decreased. In our case,

$$T_{i+1} = \alpha T_i \tag{5.17}$$

where $0 < \alpha < 1$. For each T value one performs L_M transitions. The accepted states form a Markov chain. The values of T_0, α and L_M form what is called the cooling schedule. If these three values are high, then a global minimum in the error is guaranteed to be found, but the process is very time consuming. If the cooling schedule values are lower, there are no such guarantees but the process is considerably quicker. A good SA system is therefore a compromise between speed and accuracy. To find the best compromise solution for the values of the parameters in the cooling schedule, either trial-and-error or an optimisation algorithm, such as LM or indeed simulated annealing, can be used.

5.2.3 The shortcomings of SA

SA has one major shortcoming. It gives only one state of the system with no measure of the fit error. In general, perfect data has only one global minimum. However, real ellipsometry data is inherently noisy and ambiguous. Noisy and ambiguous data can have several possible candidates for the global minimum. The ideal ellipsometry fitting tool would give all possible solutions and their corresponding confidence intervals. This combination is achieved here with Bayesian inference and the Markov chain Monte Carlo algorithm.

5.2.4 Bayesian inference and the Markov chain Monte Carlo algorithm

Here we give a qualitative argument for using MCMC. We want to find every candidate for the global minimum of an error function. To achieve this, one merely runs the SA algorithm many times using the same cooling schedule. Each run produces a possible solution. One finds the confidence intervals by counting the number of times each solution appears. We can then state the most likely solution, but of course, any of the SA solutions could define the physical structure of the test sample. The full and thorough Bayesian inference description of the MCMC algorithm is given by Barradas, Keddie and Sackin. [140] A copy of this paper can be found in Appendix B.

5.2.5 Testing the SA-MCMC algorithm with a bilayer

A simple specimen was made to test the SA-MCMC algorithm. This consisted of a silicon substrate that had a thermal silicon oxide layer with a PS layer on top. Polystyrene (Mw= 696,500g/mol) was spin coated at 2000rpm for 30 seconds onto a (111) single crystal of silicon on which a thermal oxide had been grown. The oxide layer thickness was measured before the polystyrene was spun on. Both ellipsometry and Rutherford backscattering specrometry (RBS) scans were made of the same sample. Rutherford backscattering is the coulomb elastic scattering of charged particles. Incident ions scatter elastically from target atoms with an energy characteristic of the mass of the struck nucleus. [141, 142] The measured thicknesses from both these techniques are shown in Table 5.2. The ellipsometry data was fitted, in the first instance, by the LM algorithm. The fit however was not good. It was improved by assuming some surface non-uniformity in the fitted LM model. The best-fit values with this model are also given in Table 5.2. The SA-MCMC model implemented here cannot consider surface non-uniformity,

Table 5.2: Means and standard deviations of the thicknesses and refractive indices of a polystyrene and SiO_2 bilayer on an Si substrate. The fits have been obtained in the following ways: an LM using a literature value of SiO_2 refractive index, with and without allowing for PS thickness non-uniformity; and using MCMC for the whole range of solutions and restricted to the most probable solution. The subscript 1 refers to the oxide layer, and the subscript 2 refers to the PS

Solution	d_1/ nm	na_1	nb_1	d_2/ nm	na_2	nb_2	Comments
PS/ SiO_2 bilayer	36.9-45.8[a]			93.4(1.8)[b]	1.4476[c]	0.003666[c]	
LM(non-uniform)	36.1(0.7)	1.557(3)	0.028(2)	97.7(0.1)	1.4476[c]	0.003666[c]	$\Delta d_1 = 4.45(0.37)$
LM	37.2(0.8)	1.556(9)	0.024(6)	97.7(0.1)	1.4476[c]	0.003666[c]	$\Delta d_1 = 0$
MCMC	48.5(26.9)	1.52(5)	0.01(1)	90.5(25.7)	1.482(16)	0.0033(30)	$d_1 + d_2 = 139(2)$
MCMC(restricted)	28.4(6.7)	1.54(4)	0.016(11)	109.2(6.1)	1.483(11)	0.0031(22)	$10 < d_1 < 40$ $90 < d_2 < 120$

---

[a] Determined with RBS. The two values are measurements on the edge and centre of the sample.

[b] Determined with RBS.

[c] SiO_2 values from literature. [143]

hence, using this method to fit the ellipsometry data will never give a perfect fit. The value of χ^2 calculated using SA-MCMC only reflects the error in the model and not experimental error. To overcome this shortcoming, the error bar for every data point was taken as the deviation between the data and the best-fit assuming homogeneous layers. The minimum error for each point was set to 1°. This technique ensures that all solutions similar to the best-fit will be highly probable and so the given solution will reflect the real physical structure. The results of the SA-MCMC algorithm fitting are given in Table 5.2. These reveal that the values of thickness are ambiguous with d_1 taking values between 10 and 120nm and d_2 falling between 20 and 130nm where d_j is the thickness of layer j. $j = 1$ represents the oxide layer and $j = 2$ represents the polystyrene layer. The range of possible solutions is always such that $d_1 + d_2 \approx 140$nm. Given the inherent ambiguity of ellipsometry data it is curious to note that neither $d_1 = 0$ or $d_2 = 0$ is a solution. The na_j values for the two layers are however well defined and although they are close the values for the two layers are different. The polystyrene layer having na_1 slightly above 1.5 and the SiO_2 layer na_2 just below 1.5. There is a high probability of low nb_j values ($nb_j < 0.01$), however, there is still a low probability of high nb_j values ($nb_j > 0.01$). The strong linear correlation between the two layers ($d_1 + d_2 \approx 140$nm) probably stems from these similar refractive index values and the associated weak reflection from the interface between the two layers. The order of the two layers stacked on the substrate is not, however, interchangeable because the probability density of the refractive indices is not the same for both layers. The most probable values of the thicknesses are within the ranges 10nm$< d_1 <$ 40nm and 90nm$< d_2 <$ 120nm. The corresponding refractive indices to both these thickness regimes are shown in Table 5.2. The SiO_2 layer has a well defined refractive index with high certainty, whereas the PS layer does not. Overall, they compare well to the RBS and LM fitting.

5.2.6 Conclusion and further work

For the first time a method has been shown that can invert ellipsometry data without any knowledge of the thin film structure thus greatly increasing the applications of ellipsometry. All possible solutions that can reproduce the ellipsometry data set can be found. The drawback with this technique is the slowness of the computations required. For example, the bilayer data set shown here took about 24 hours to analyse. However, careful tuning of the cooling schedule, which has not been done at the present time, could give at least an order of magnitude improvement. Of course, the second improvement would be to increase the scope of the model to include many more layers, surface non-uniformity and biaxiality. In its final development this work could describe the exact shape of the solvent front swelling polymer. The limit would be the ambiguity inherent in the noisy ellipsometry data rather than the finite area of local minima solution space explored.

Chapter 6

Solvent flux limited diffusion of solvent into polymer

6.1 Introduction

In 1991 Gall and Kramer demonstrated Case II diffusion in the toluene/ polystyrene system. [144] In their experiments, deuterated toluene *vapour* was diffused over a range of temperatures and equilibrium solvent fractions. The equilibrium solvent fraction in the swelling polystyrene was varied by using large volumes of different fractions of polystyrene dissolved in toluene as a vapour source. Measurements were performed with forward recoil ion-beam spectrometry. Gall and Kramer showed that increasing the temperature increases the Case II front velocity and that the diffusion coefficient of the Fickian precursor ahead of the Case II front is approximately independent of solvent activity. However, the use of NMR microimaging at Surrey with *liquid* toluene ingressing PS revealed two characteristics: firstly, Fickian dynamics and secondly, polystyrene is dissolved by pure toluene. The characteristics are illustrated in Figure 6.1. The sample preparation is the same as that used for the MEK ingress experiments. The toluene reservoir is at the top of each image. The solid PS gives no signal and is the dark region towards the bottom. The swelling and dissolving gel region is the bright region in the middle. This region is shown expanding non-linearly with time. The diffuse grey region is the polystyrene dissolving into the solvent. A plot of the position of the polymer/gel interface with time is shown in Figure 6.2. A best-fit of A and B to the formula $x = At^{1/2} + B$ (where x is the position of the polymer/ rubber interface in mm and t is time) is overlayed in this plot. The good agreement is extremely convincing evidence of Fickian dynamics. A characteristic diffusivity of 9.1×10^{-7} cm^{2}s^{-1} can be found from A. B should of course be equal to zero, since at the beginning of the experiment there will be no gel region. However, the exact position of the front of the sample is notoriously difficult to determine exactly and B gives a measure of the error in finding this position.

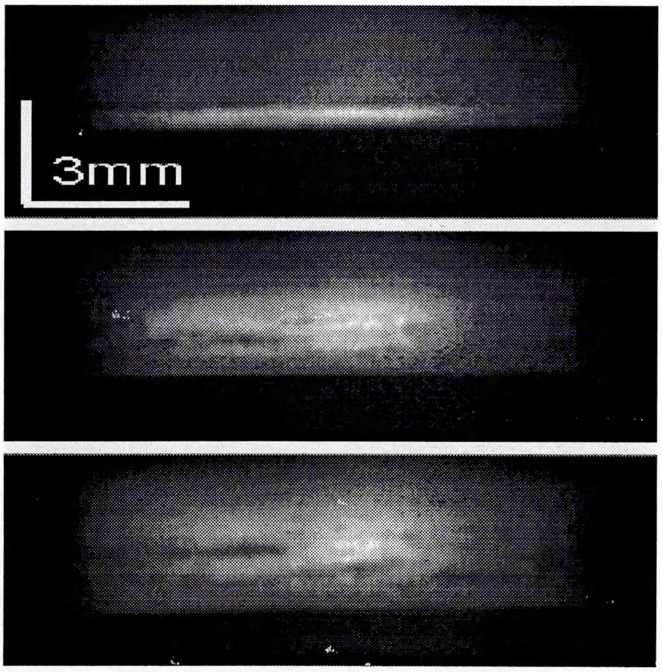

Figure 6.1: NMR microimages of pure toluene ingressing and dissolving PS. The first image is at 0.3 hours the other two images are at 2.3 and 4.3 hours respectively. The size of the gel region can be seen expanding non-linearly with time indicating non-Case II kinetics.

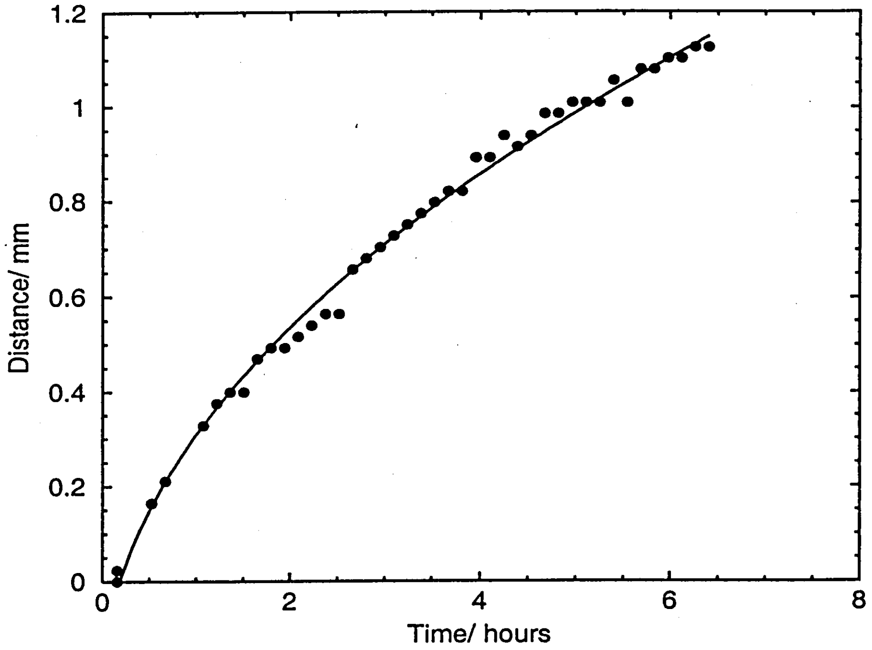

Figure 6.2: The position of the polymer/gel interface against time for toluene ingressing PS is shown by the circles. The solid line is the best-fit to the interface.

There are other anomalies in the literature regarding Case II diffusion. NMR measurements have sometimes shown the dynamics of the rubber changing on timescales orders of magnitude greater than any commonly accepted polymer chain disentanglement time. An example of this phenomenon has been observed at Surrey by Perry *et al* [145] for acetone vapour ingress into poly(vinyl chloride). Measurements showed that the dynamics of the rubber region behind the liquid front evolved over a period of days. One would normally expect this evolution to occur over a period of the order of seconds. [5] Furthermore, Hui *et al* [146] observed a very rapid rise in the Case II front velocity at higher equilibrium solvent concentrations which they were unable to explain in terms of the Thomas and Windle model. [17]

What has caused toluene diffusion to be Case II in the Gall and Kramer experiments but Fickian here? Three ways have previously been cited. One explanation is that any Case II diffusion process will become Fickian in the long time limit for very large samples. The solvent flux is proportional to the solvent concentration gradient. As the distance between the Case II solvent front and the sample surface increases, the solvent concentration gradient decreases, thus reducing the maximum flux into the glassy polymer. At some large time and distance, governed by the physical properties of the particular polymer/ solvent system studied, the amount of solvent arriving becomes the rate limiting factor and Fickian dynamics are thus observed. However, there has yet to be an unambiguous observation of the transition occasioned in this way. A second possibility is that varying the temperature of the experiment can, in some systems, increase the maximum solvent flux at the gel/glass interface more quickly than the liquid diffusivity in the rubber. This has been shown experimentally at the University of Surrey for the system of methanol ingressing poly (methyl methacrylate) (PMMA). [18] The third way to cause a Case II to Fickian transition is varying the composition of the solvent either by using different amounts of good and bad solvents, or pre-swelling the polymer with a good solvent before ingressing a bad solvent. This has also been demonstrated at Surrey for PMMA pre-exposed to acetone ingressed by methanol. [18]

At the heart of the Thomas and Windle model [17] is the assumption that swelling at the glass-to-rubber transition is the rate limiting step that can cause Case II diffusion. The transition to Fickian diffusion occurs when this is no longer the rate limiting process. We propose that there are circumstances in which the rate determining step is not the swelling at the solvent front. Instead, solvent ingress can be limited by the flux of solvent impinging on the polymer sample surface. We call this surface-flux-limited Case II diffusion. We suggest that the difference between Gall and Kramer's work [144] and that reported here is that theirs is in the surface-flux-limited regime. This new theory can also explain the work of Hui *et al* and Perry *et al* described above.

Experimentally we have changed the surface flux in three different ways: 1.

changing the vapour path length; 2. changing the activity of the toluene by using different polystyrene/ toluene fractions in the vapour source; and 3. varying the temperature of the experiment. STRAFI has been used because the signal from the vapour induced rubber region is too low to be measured using conventional MRI. In this chapter, our experimental observations of solvent-flux-limited Case II diffusion using toluene vapour ingressing polystyrene are reinforced by a new phenomenological model.

6.2 The model

The aim of the model is to represent solvent ingress into glassy polymer in as simple a way as possible. It uses the basics of the physics to give the qualitative behaviour of the system. Like our NMR experiments, we consider uniform polymer with its surface parallel to the solvent so that the solvent advance is one-dimensional. c the solvent concentration (number per unit volume) is a function of z (distance from the polymer surface) and t the time since solvent started to ingress into the polymer. At the polymer surface, $z = 0$. We define a dimensionless concentration $\phi = c/c_m$ where c_m is the maximum concentration of the solvent in the swollen polymer.

6.2.1 Fickian diffusion

First we consider the most simple solvent diffusion into the polymer with a constant diffusion coefficient D. The surface concentration is fixed at c_m. Neglecting a transformation of co-ordinates caused by sample swelling, Fick's second law in this case gives:

$$\frac{\partial\phi(z,t)}{\partial t} = D\frac{\partial^2\phi(z,t)}{\partial z^2} \tag{6.1}$$

subject to the boundary conditions

$$\phi(z > 0, t = 0) = 0 \tag{6.2}$$

$$\phi(z = 0, t) = 1. \tag{6.3}$$

Equation 6.1 can be solved analytically. [8] The result is a solvent front advancing as $t^{1/2}$. To solve Equation 6.1 numerically, space and time are discretised into elements of width a and δt respectively. The reduced solvent concentration in the ith element at time t is $\phi(i,t)$. Element 1 is at the surface. Analogous boundary conditions to Equations 6.2 and 6.3 can be written as:

$$\phi(i > 1, t = 0) = 0 \tag{6.4}$$

$$\phi(1, t) = 1. \tag{6.5}$$

The time evolution of the concentrations of the other elements is governed by the equation

$$\phi(i, t + \delta t) = \phi(i,t) + \frac{D\delta t}{a^2}\left[\phi(i-1,t) - 2\phi(i,t) + \phi(i+1,t)\right] \qquad i > 1. \tag{6.6}$$

From Equations 6.4, 6.5 and 6.6 results indistinguishable from their analytical analogues (Equation 3.17) are obtained as long as the reduced time increment $D\delta t/a^2$ is small and we have lengthscales much greater than a.

6.2.2 Case II diffusion

Ingress into a glassy polymer is slow until it becomes a rubber. This limits the flux from the rubber into the glass. This can be the rate-limiting step when the mechanical relaxation of the glassy polymer at the solvent front is very slow. The solvent front lies at the interface between the rubber and glass, between elements i_s and (i_s+1). To keep our model simple we characterise the rubber-glass boundary with just two parameters: 1. the critical reduced solvent concentration

ϕ_{rg} needed to transform the glass to a rubber; and 2. the maximum flux j_{rg} at the solvent front. We can write that $\phi(i_s, t) \geq \phi_{rg}$, $\phi(i_s+1, t) < \phi_{rg}$. At any time t, i_s is defined as being the largest value of i for which $\phi(i, t) > \phi_{rg}$. Slow mechanical relaxation at the the solvent front is modelled by limiting the flux from the most advanced rubbery element i_s into the adjoining glass element $(i_s + 1)$. The time evolution of the concentrations in the i_sth and $(i_s + 1)$th elements is governed by the equations

$$\phi(i_s, t + \delta t) = \phi(i_s, t) + \frac{D\delta t}{a^2}\left[\phi(i_s - 1, t) - \phi(i_s, t)\right] - \frac{j_f \delta t}{c_m a}, \tag{6.7}$$

and

$$\phi(i_s + 1, t + \delta t) = \phi(i_s + 1, t) + \frac{j_f \delta t}{c_m a}, \tag{6.8}$$

where

$$\frac{j_f \delta t}{c_m a} = \min\left(\frac{j_{rg}\delta t}{c_m a}, \phi(i_s, t) - \phi_{rg}\right). \tag{6.9}$$

The flux at the solvent front is j_f and j_{rg} is the flux into the glass if the concentration in the neighbouring rubber element is high enough. It is an upper bound to the flux. If the concentration in the last rubber element is very close to ϕ_{rg} then the flux is lower than j_{rg}. The flux into the glassy element $(i_s + 1)$ then tends towards the flux into the last rubber element i_s at the previous time step. The change in ϕ is $j_f/(c_m a)$ because the rate of change in concentration c inside a slice of width a due to a flux j_{rg} equals j_{rg}/a. This is then multiplied by our time step and divided by c_m to get the change in the reduced concentration ϕ in a time δt. Beyond the glassy element in contact with the last rubber element, there is no diffusion and $\phi(i) = 0$. The time evolution in the rubber, $i < i_s$, is given by Equation 6.6. The model does not predict a Fickian precursor because of the absence of diffusion in the glass. There are two competing rates, the slowest of which will be the rate limiting step to the front advance. For a solvent front at z_s, one rate, called the characteristic speed comes from the diffusion of the solvent from the surface in contact with the solvent. The diffusive speed is $s_D = D/z_s$. It can be found by differentiating the $t^{1/2}$ advance or by dimensional analysis. The second characteristic speed is for the glass-to-rubber transition at the solvent front $s_{rg} = j_{rg}/c_m\phi_{rg}$. If $s_D \ll s_{rg}$, that is to say the diffusion from the solvent surface is the limiting speed of advance, then the results are little different from Fickian diffusion without the boundary conditions given in Equations 6.7 and 6.8 with the solvent advancing as $t^{1/2}$. However, in the opposite limit where $s_D \gg s_{rg}$ then it is the glass-to-rubber transition itself which limits the speed of advance. The solvent front then advances with t. This is solvent-front-limited Case II ingress. s_D decreases as z_s increases but s_{rg} is fixed for a particular system. This means that at large z_s which occurs at long times, the solvent advance will always become proportional to $t^{1/2}$. The crossover in dynamics occurs at $s_D = s_{rg}$, when $z_s = Dc_m\phi_{rg}/j_{rg}$. Example behaviour of this model is shown in Figure 6.3. There are two dimensionless parameters: ϕ_{rg} and $\alpha = j_{rg}a/Dc_m$. The ratio $\alpha = s_{rg}/s_D$ with s_D evaluated at $z_s = a$. We set $\phi_{rg} = 0.2$. This is a reasonable value for a real system and indeed the results from the model are not sensitive to the precise value. The only parameter to vary is then α. Plots of $\alpha = 10^{-2}$, 10^{-3} and 10^{-4} are shown in Figure 6.3. The time unit is a^2/D and the length unit is a. For $\alpha = 10^{-2}$ the solvent advance is close to $t^{1/2}$. For $\alpha = 10^{-4}$ the solvent advance is linear for the entire period shown. For the intermediate value of α, the solvent front movement is linear up to $t = 10^5$. It then curves over and tends towards a $t^{1/2}$ dependence. This is as one expects because for $\alpha = 10^{-3}$ the solvent front will be diffusion limited for z_s greater than approximately 10^3a.

6.2.3 Low flux at the surface

Instead of having a liquid solvent reservoir in contact with the polymer surface, one could instead have solvent vapour. The flux of solvent available could be

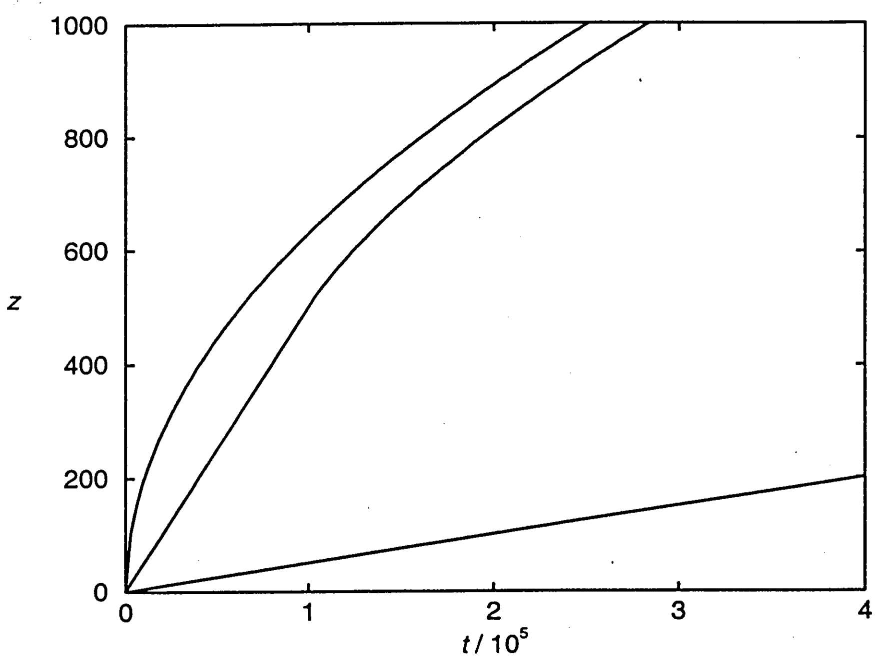

Figure 6.3: Calculations of the advance of the solvent front. The x axis is time in units of a^2/D. The time step $\delta t = 0.1a^2/D$ The y axis is the position of the solvent front in units of the element of width a. From top to bottom: $\alpha = 10^{-2}$, 10^{-3} and 10^{-4}

much lower than that from the liquid and indeed it could be so low as to be rate limiting. This phenomenon can be modelled by replacing the boundary condition of Equation 6.5 with a constant flux j_v. The boundary condition is written as:

$$\phi(1,t+\delta t) = \min\left(\phi(1,t) + \frac{D\delta t}{a^2}\left[\phi(2,t) - \phi(1,t)\right] + \frac{j_v}{c_m a}, 1\right). \tag{6.10}$$

That is to say, there is a constant flux j_v into the sample surface, unless this flux causes the concentration to exceed the maximum value. Equation 6.10 controls the flux into the rubber whereas Equation 6.7 controls the flux out of the rubber. Either of these equations can be rate limiting. We can again define a characteristic speed of advance, $s_v = j_v/(c_m\phi_{rg})$. It is the rate at which the solvent front advances if the flux at the surface is the rate limiting step. This will occur when $s_v \ll s_D, s_{rg}$. Linear ingress occurs even if $s_{rg} \gg s_D$. Hence a linear advance is seen for a polymer and solvent system that is Fickian when the polymer is is contact with liquid solvent. We call this solvent-flux-limited Case II diffusion. Example calculations were performed using this model are represented in Figure 6.4. The model has three dimensionless parameters ϕ_{rg} and the ratios

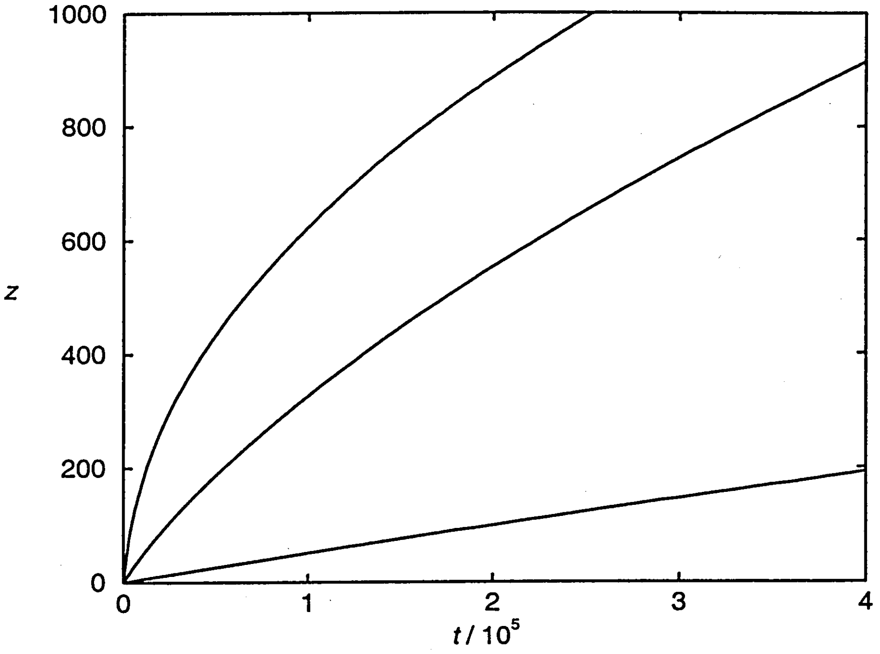

Figure 6.4: Calculations of the advance of the solvent front. The x axis is time in units of a^2/D, our time step $\delta t = 0.1a^2/D$. The y axis is the position of the solvent front in units of the element width a. From top to bottom, $\beta = 10^{-2}$, 10^{-3} and 10^{-4}; $\alpha = 10^{-2}$.

$\alpha = j_{rg}a/(Dc_m)$ and $\beta = j_v a/(Dc_m)$. Once these terms are fixed the solvent front position and concentration profile can be found at any time using Equations 6.6, 6.7, 6.8, 6.9 and 6.10. ϕ_{rg} is fixed at 0.2 as before. If we have that $s_v \gg s_{rg}, s_D$ this is the same situation as before. Hence, here we consider only $s_v \leq s_{rg}$. The results in Figure 6.4 are for the case $\alpha = 10^{-2}$ and $\beta = 10^{-2}$, 10^{-3} and 10^{-4}. For $\beta = 10^{-4}$ the solvent front advance is linear. For $\beta = 10^{-2}$ the advance is proportional to $t^{1/2}$. For $\beta = 10^{-3}$ it is neither linear nor $t^{1/2}$. Over the range plotted in Figure 6.4 neither diffusion nor flux at the surface completely dominate. Solvent concentration profiles at approximately the same position are plotted in Figure 6.5. When the ingress is solvent flux-limited the concentration profile is

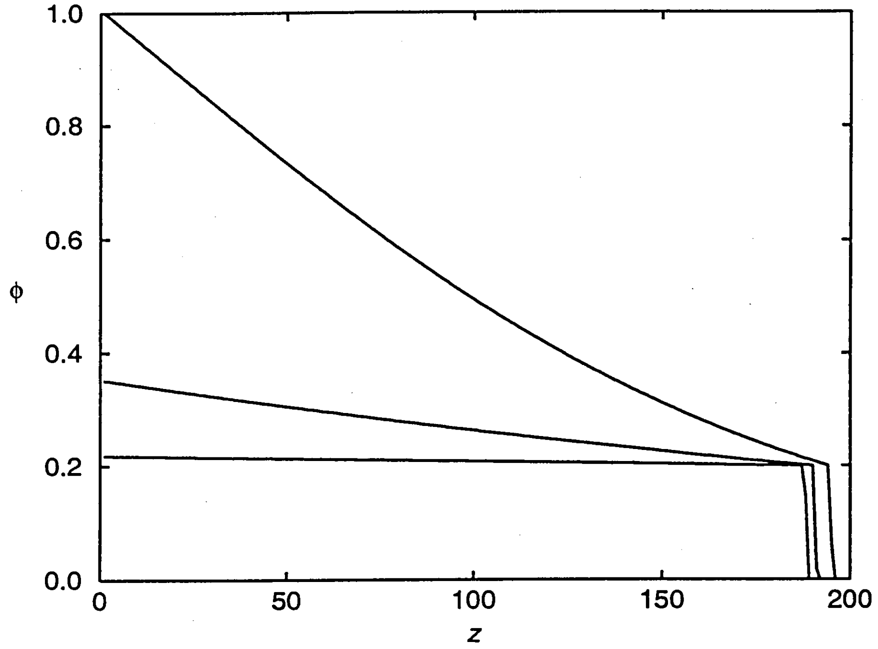

Figure 6.5: Three solvent profiles, ϕ as a function of z, are plotted. They are plotted at different times, each when the front has moved a distance close to $200a$. From top to bottom the curves are for $\beta = 10^{-2}$, 10^{-3} and 10^{-4}, respectively; $\alpha = 10^{-2}$. The three curves are at times 12,000, 51,000 and 390,000, in units of a^2/D, for $\beta = 10^{-2}$, 10^{-3} and 10^{-4}, respectively. The time step $\delta t = 0.1a^2/D$.

rather flat. The concentration is close to ϕ_{rg} everywhere. Because the solvent front advances as fast as the solvent arrives at the surface, the solvent does not build up as it does for Fickian or solvent-front-limited Case II diffusion. The solvent concentration profiles for solvent-flux and solvent-front-limited diffusion are therefore very different. For the former it is always slightly above ϕ_{rg}, for the latter it is considerably higher. However, in both cases the profile will be close to a straight line because in both cases diffusion is a fast process relative to the solvent front advance.

6.2.4 Relation to previous work

It is intriguing to compare the purely phenomenological model described here with more thorough analyses to be found in the literature. [17, 19, 147] In our model, we set the flux into the glassy polymer to be very small. Previously, other authors have instead used models in which visco-elastic relaxation couples to the diffusion of the solvent. Essentially, solvent diffuses into the glassy polymer that swells to accomodate increasingly more solvent. As it does so the diffusion coefficient increases rapidly. This slow diffusion into the glassy polymer and the resulting swelling, which both occur at the solvent front, then limit the ingress speed. Lasky *et al* [148] neglect the rapid viscosity change as solvent diffuses into the polymer and instead consider an effective viscosity of the glass ϕ_g. If we follow this suggestion then swelling takes a time of order $\phi_g/(ckT)$ where ckT is an approximation to the osmotic pressure exerted by the solvent. Similarly the rapid change in diffusion coefficient in the glassy polymer can be considered as some effective diffusion constant D_g. The width of the diffusion front is the distance the solvent diffuses in a time $\phi_g/(ckT)$. This is $(D_g ckT/\phi_g)^{1/2}$. An estimate of the velocity of the solvent front advance, s_{rg} is then $(D_g ckT/\eta_g)^{1/2}$. [148] Hence, s_{rg} can be estimated if one knows both the time taken for the initially glassy polymer to swell and the distance the solvent diffuses in this time. In their experiments, Lasky *et al* [148] find a value of $(ckT)^{1/2}$ of the order of 10^4Nms and η_0 of the order of 10^{14}Nsm^{-2}. A typical value of D_g for small molecule diffusion is 10^{-8}cm^{2}s^{-1}. This predicts a value of $s_{rg} \approx 1$nms^{-1}.

6.3 Experimental work

6.3.1 Sample preparation

The polystyrene and toluene were presented to the magnet in one of two ways. These are shown in Figures 6.6 and 6.7. The idea was to have a liquid reservoir separated from the PS by a vapour path. Ideally the PS would swell vertically upwards to avoid gravity causing the swelling rubber to flow down the sides of the test tube. Using arrangement A (Figure 6.6), longer vapour path lengths were made by inserting 8mm OD glass rod of varying lengths between the bottom of the 8mm OD small test tube and the top of the PTFE sleeve. The short vapour path length (3mm) was achieved with arrangement B (Figure 6.7). It should be noted that with set-up B the polymer swells down the test tube, where gravity causes the rubber to flow down the sides of the test tube and into the toluene where it is dissolved. Hence, this arrangement should only be considered unaffected by gravity in a very short time period. Sample A was adopted to alleviate this problem. The solvent reservoir was filled either with pure toluene or a homogeneous mixture of toluene and PS for the reduced activity experiments. For the variable temperature experiments dry heated air was blown over the sample. The temperature was measured using a PT100 resistor to an error of ±0.1°C. Fixed temperature experiments were performed at 17°C. This is the temperature of the bore of the magnet.

6.3.2 Estimating the toluene vapour flux

An estimate of the toluene vapour flux in set-up A

Refering to Figure 6.6. F_1 is the vapour flux leaving the solvent reservoir, F_2 is the flux in the space between the outer test tube and the sculpted tube and F_3 is the

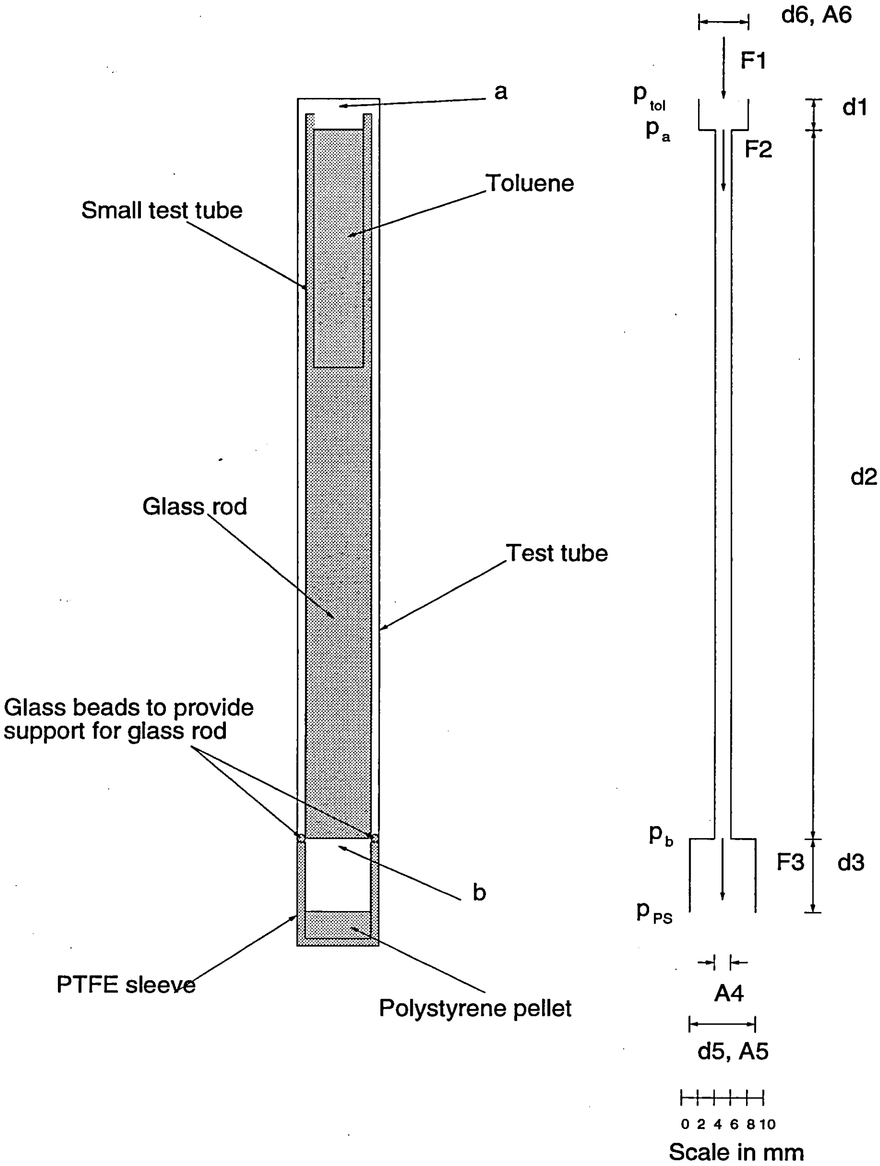

Figure 6.6: A schematic of the toluene and polystyrene sample preparation for long path lengths (Arrangement A)

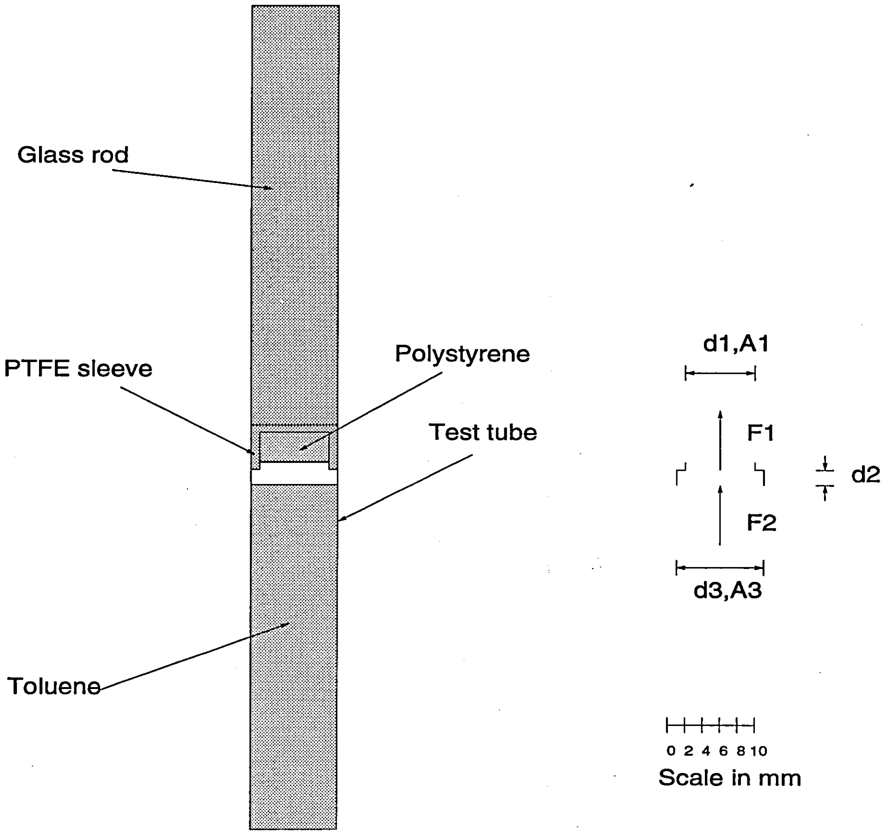

Figure 6.7: A schematic of the toluene and polystyrene sample preparation for the 3mm path length (Arrangement B)

flux entering the polystyrene. d_1 is the distance between the top of the reservoir and the top of the small sculpted test tube; d_2 is the distance between the top of the small sculpted test tube and the top of the PTFE sleeve; and d_3 is the distance between the top of the PTFE sleeve and the surface of the polystyrene. A_4 is the area between the sculpted test tube and the outer test tube; d_5 and A_5 are the diameter and area at the surface of the swelling polystyrene; and d_6 and A_6 are the diameter and area at the surface of the solvent reservoir. Assuming conservation of mass along the sample

$$F_1 A_6 = F_2 A_4 = F_3 A_5. \tag{6.11}$$

From Fick's first law:

$$F_1 = \frac{D_v(p_{tol} - p_a)}{d_1} \tag{6.12}$$

$$F_2 = \frac{D_v(p_a - p_b)}{d_2} \tag{6.13}$$

$$F_3 = \frac{D_v(p_b - p_{PS})}{d_3} \tag{6.14}$$

where D_v is the toluene vapour diffusion coefficient and p is the vapour pressure evaluated at the surface of the toluene reservoir (tol); at positions a and b as indicated in Figure 6.6; and at the surface of the swelling polystyrene (PS). Combining Equations 6.11 to 6.14 we can write

$$F_3 = \frac{D_v(p_{tol} - p_{PS})}{\frac{A_5}{A_4}d_2 + \frac{A_5}{A_6}d_1 + d_3} \tag{6.15}$$

Also, from ideal gas kinetics

$$D_v = \frac{3}{8}\left(\frac{\pi}{2}\right)^{\frac{1}{2}} \frac{1}{c_{air}\sigma^2}\left(\frac{RT}{M}\right)^{\frac{1}{2}} \tag{6.16}$$

where R is the universal gas constant, T is temperature, $M = \frac{M_{tol}M_{air}}{M_{tol}+M_{air}}$ (M_{air} and M_{tol} are the molecular weights of air and toluene respectively), σ is the mean of the radii of the air and toluene molecules assuming they are classical spheres and c_{air} is the number density of the mixture of air and toluene vapour. [149] The initial value of d_1 is $d_{1_{init}} = 2$mm however it increases as the toluene is absorbed by the PS as $d_1 = d_{1_{init}} + d_{swollen}\frac{A_5}{A_6}$ where $d_{swollen}$ is the change in length of the PS pellet at some time, d_2 is the part of the path length we have varied at values of 3.5, 9.5 and 19.5cm. The initial value of d_3 is $d_{3_{init}} = 11$mm however it decreases as the toluene is absorbed by the PS as $d_3 = d_{3_{init}} - d_{swollen}$. $d_5 = 8$mm and $d_6 = 6$mm giving $A_5 = 50.27\text{mm}^2$ and $A_6 = 28.27\text{mm}^2$. A_4 is 13.35mm^2. To calculate D_v: $\sigma = 3.36 \times 10^{-10}$m, $M = 11.08$g and $c_{air} = 2.49 \times 10^{24}\text{m}^{-3}$. At $T = 17°$C, this gives a value for D_v of $1.75 \times 10^{-5}\text{m}^2\text{s}^{-1}$.

An estimate of the toluene vapour flux in set-up B

In Figure 6.7, F_1 is the toluene vapour flux at the surface of the PS. F_2 is the vapour flux leaving the solvent reservoir. A_1 and d_1 are the area and diameter of the swelling polystyrene pellet. d_2 is the distance between the surfaces of the toluene and PS. A_3 and d_3 are the area and diameter of the surface of the toluene reservoir. We can write, assuming conservation of mass, that

$$F_1A_1 = F_2A_3. \tag{6.17}$$

From Fick's first law:

$$F_2 = \frac{D_v(p_{tol} - p_{PS})}{d_2}. \tag{6.18}$$

p_{tol} and p_{PS} are the toluene vapour pressures at the surface of the solvent reservoir and at the surface of the swelling polymer respectively. D_v is defined in Section 6.3.2. Substituting Equation 6.17 into Equation 6.18 and rearranging

$$F_1 = \frac{A_1D_v(p_{tol} - p_{PS})}{A_3d_2}. \tag{6.19}$$

In this experiment, $d_1 = 8$mm, $d_2 = 3$mm and $d_3 = 9$mm. Equations 6.15 and 6.19 require accurate values of p_{tol} which will be considered next.

6.3.3 Values for the toluene vapour pressure

Toluene vapour pressure as a function of polystyrene fraction

Values for the vapour pressure of a mixture of polystyrene (with a molecular mass of 290,000g/mol) and toluene at different fractions have been measured by Bawn, Freeman and Kamaliddin. [104] A graph of their results is shown in Figure 6.8. Flory-Huggins theory can be written in terms of vapour pressures:

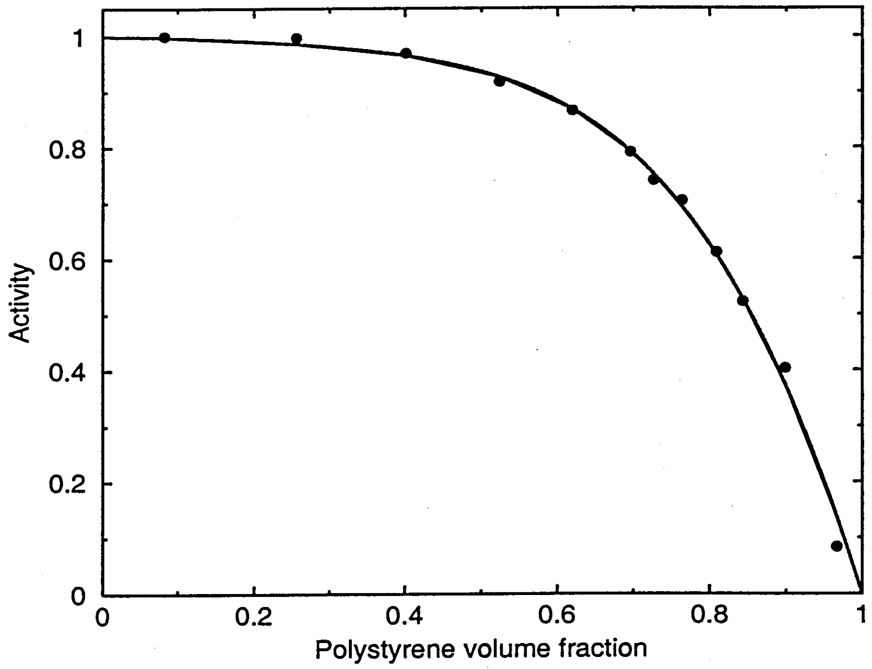

Figure 6.8: A graph of toluene activity above a mixture of PS and toluene as a function of PS volume fraction. The circles denote Bawn, Freeman and Kamaliddin's original data and the line is a best-fit to Flory-Huggin's theory

$$\frac{p_{PS}}{p_{tol}} = \exp(\ln(1-\phi_2) + (1-\frac{V_1}{V_2})\phi_2 + (X_0 + X_1\phi_2 + X_2\phi_2^2)\phi_2^2). \tag{6.20}$$

ϕ_2 is the polymer volume fraction, V_1 is the toluene molar volume (106.52cm^3/mol) and V_2 is the PS molar volume (273584.91cm^3/mol). X_0, X_1 and X_2 are the fit parameters representing a concentration dependent Flory-Huggins interaction parameter. [103] A least-squares best-fit of Equation 6.20 to the data of Bawn *et al.* gives $X_0 = 0.163977$, $X_1 = 1.08418$ and $X_2 = -0.779059$.

Toluene vapour pressure as a function of temperature

A plot of toluene vapour pressure against temperature is shown in Figure 6.9. [150]

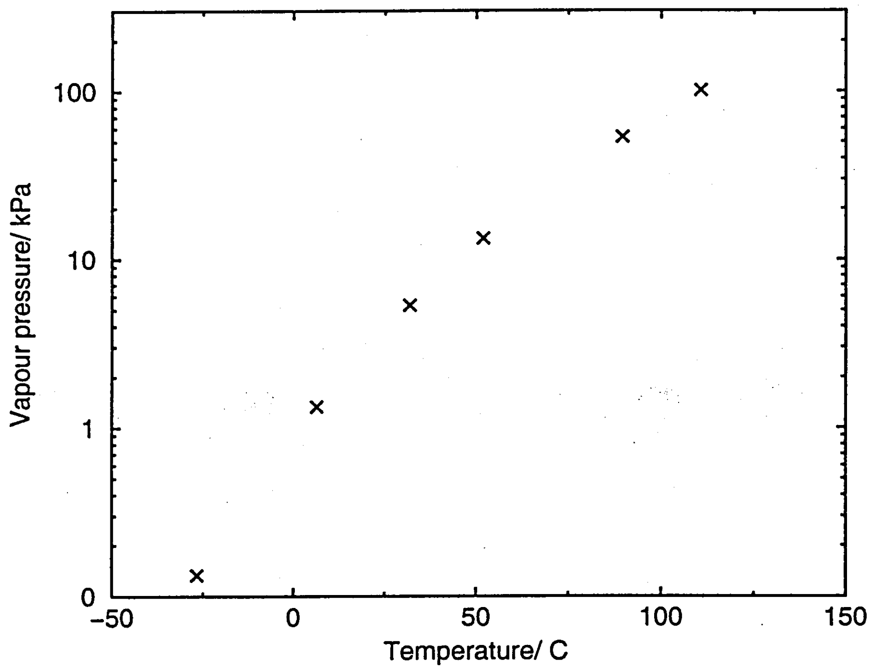

Figure 6.9: A graph of toluene vapour pressure as a function of temperature based on data from reference [150]

The toluene vapour pressure at 17°C is 3000Nm^{-2}.

6.3.4 STRAFI acquisition parameters

A quadrature echo sequence as described in Section 2.3.6 was used with a 90° pulse width of around 20μs, $\tau = 35\mu$s and n=16. The stepper motor was moved in 60μm increments.

6.3.5 Measuring the swelling front position

To measure the size of the swelling front the last eight echoes were summed giving signal only from the more mobile component. The front and rear portions of the swelling front were measured at the position of the half maximum of this summed signal.

6.3.6 Finding the solvent volume fractions through the swelling PS

Best-fits were made, at each stepper motor step, to the decaying NMR echo peak envelope S of the form

$$S = Ae^{-Bt} + C \tag{6.21}$$

where A, B and C are the fitted parameters. A gives the amount of short, polymer T_2 component. The mobile solvent has a long T_2 component and is thus represented by C. The solvent fraction is then simply calculated as $C/(A+C)$. Before fitting the echo peaks, the first two points were multiplied by a factor of 1.5×1.5. The first factor is to correct for systematic low intensity between the first STRAFI echo which is a pure Hahn echo and the second which is a superposition of Hahn and stimulated echoes. [151] The second factor is to compensate for errors in setting the 90° pulse. This value is justified for a number of reasons. Firstly, they give more physical echo train decays. Secondly, values of surface solvent concentration between the two methods used (these are described below in Section 6.3.7) are in much better agreement.

6.3.7 Finding the PS/ toluene fraction at the surface of the swelling PS

The surface PS/ toluene fraction has been found in two ways, namely: performing three component fits, as described above, to the decaying echoes of the NMR signal; and finding by how much the PS pellet has swollen. Since this increased volume must be due to the toluene in the polystyrene, a ratio of the total change in length of the PS pellet to the length of the gel region will give the toluene volume fraction.

6.3.8 Calculating the mass of toluene being taken up at the polymer surface

The mass of toluene taken up by the PS has been calculated in two ways: multiplying the Case II front velocity by the product of the toluene density and the polymer surface area; and from the change in area between two solvent concentration profiles at early times are used to find the amount of solvent taken up in a known length of time. In this short time frame, it is much more reasonable to consider that solvent uptake is constant with time.

6.3.9 Calculating diffusion coefficients from the solvent front shapes

We can rewrite Fick's first law as:

$$D(z,t) = -\frac{j(z,t)}{\partial\phi(z,t)/\partial z} \tag{6.22}$$

where D is the diffusion coefficient at time t, position z and solvent concentration ϕ. If both the shape and velocity of the solvent front do not vary with time then we can write

$$j(z,t) = v\phi(z,t). \tag{6.23}$$

Substituting Equation 6.23 into Equation 6.22, we have

$$D(z,t) = -\frac{v\phi(z,t)}{\partial\phi(z,t)/\partial z}. \tag{6.24}$$

Hence, if in an experiment we can determine c and its derivative with respect to position then, for a solvent front advancing at a constant known velocity, v we can determine the diffusion coefficient. In the work described here, we are able to vary the velocity by varying the incident flux, this gives a way of determining the diffusion coefficient in non-equilibrium situations. In particular, if D is history dependent, we can use Equation 6.24 to obtain values of D and, at least in principle, study the history dependence by varying v. To the best of our knowledge, this capability has not been pointed out or derived in the literature.

6.3.10 Analysis of STRAFI profiles

Shown in Figure 6.10 are a set of raw data stray field imaging profiles. The sample studied in this case is vapour from a pure toluene reservoir ingressing polystyrene with a vapour path length of 3.5cm. The profiles shown are MR spin-echo trains recorded at each sample location. The time interval between profiles is 30 hours. To the left of each profile is the vapour space, and to the right is the glassy polymer appearing as a series of short echo decay trains. The central, larger amplitude region, is the rubber. Both the swelling polymer surface and the rubber interface are well resolved. After best-fits have been made to the decaying NMR echo peak envelope as described in Section 6.3.6, a set of solvent concentration profiles are produced as shown in Figure 6.11 After an initial period in which the front shape forms (shown as profile (a) in the figure) the profiles overlay

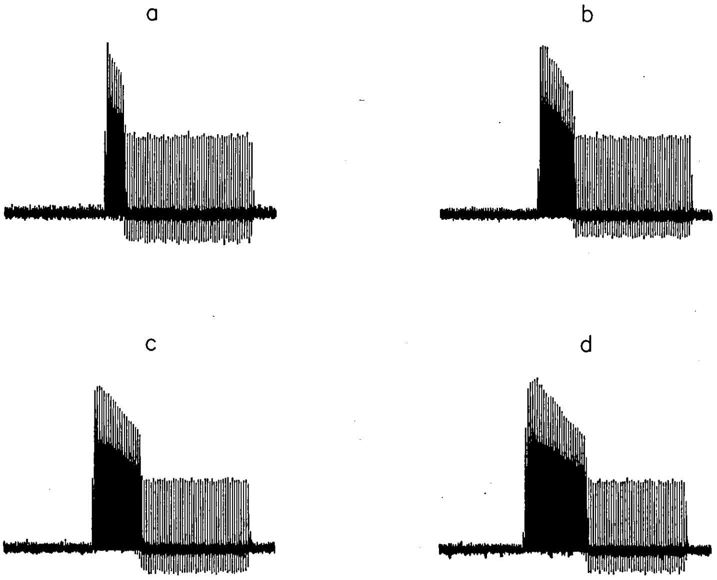

Figure 6.10: Raw data stray field profiles of the ingress of toluene vapour (d=3.5cm) into polystyrene at 17°C. The profiles are recorded after (a) 30, (b) 60, (c) 90 and (d) 120 hours. The profiles consist of 128 magnetic resonance spin echo trains. Each train consists of 16 echoes recorded over 1120μs. The trains are recorded at different slices of the sample separated by 60 μm. Hence each profile is 7.68mm long. To the left of each profile is the vapour space (no signal) and to the right the glassy polymer (strongly attenuated signal). The rubber is between. Within the rubber, the echo trains are bi-exponential decays. Even by eye, it is possible to estimate the solvent fraction.

each other (profiles (b) and (c) in the figure). From the gradient of the profiles, measured by drawing a tangent, the diffusivity is found using Equation 6.24. This calculated diffusivity relates to the time since the profile first passed $-z'/v$. We expect that diffusivity is both concentration and history dependent. When the profiles overlay, D as a function of both concentration and experiment history can be calculated from Equation 6.24. In Figure 6.11 a tangent is shown to the overlaying profiles at $\phi = 0.225$. The results of these calculations are given in Section 6.3.11. In theory, we could evaluate earlier profiles such as profile (a) in Figure 6.11 if the flux is determined from the time dependence of the profile shape. We could then estimate the concentration history dependence of

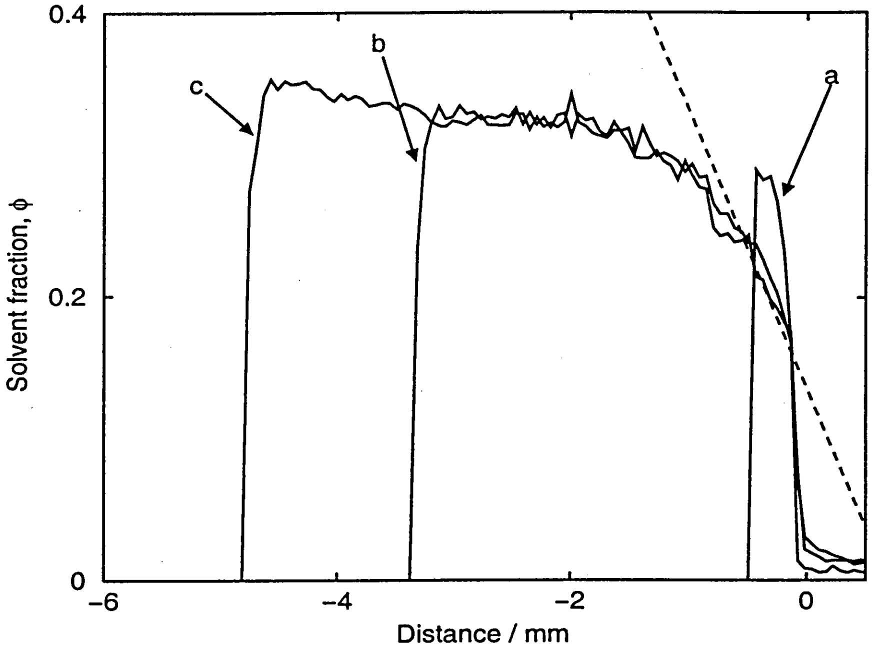

Figure 6.11: Three solvent fraction profiles extracted from STRAFI toluene vapour ingress data with d =3.5cm at 17°C, recorded after (a) 17 hours, (b) 8 and (c) 13 days. The profiles have been shifted so that the solvent front positions are at z'=0. After an initial development stage, the front shape assumes a constant, pseudo-equilibrium, form. The dashed line is a tangent to this shape from which the diffusivity at ϕ=0.225 is calculated.

D. However, the spatial and temporal resolution of MR are inadequate to study this early period. Additionally, when we fit to the echo trains there is ambiguity between the signal contributions from the solvent and from the polymer. At high solvent concentrations, the solvent diffusivity decreases the apparent spin relaxation of the solvent and the spin-spin relaxation time of the polymer also increases. One could, nevertheless, acquire data using a technique with higher spatial and temporal resolution, such as ion beam analysis. This can also better separate the solvent and polymer concentration fractions. By using different vapour path lengths one has the great advantage of tracing alternate cuts through $D(c, t)$ space. It should also be mentioned that, at low solvent concentration, although in theory we can evaluate the diffusion coefficient using the method described above, the gradient is so steep that it is limited by pixel resolution and only an upper bound to D can be found. Furthermore, is is not obvious that Fick's first law remains valid and higher order terms may need to be included.

6.3.11 Varying the vapour path length

Aim

The aim of this set of experiments is to determine whether, Case II ingress can be induced by limiting the solvent vapour supply. We expect to see that the Case II front velocity is proportional to the vapour flux. Here, we vary the solvent vapour flux by adjusting the vapour path length.

Experimental results

Plots of Case II front position versus time are shown in Figure 6.12 for path lengths of 19.5, 9.5, 3.5 and 0.3cm. The initial period, where the solvent is apparently seen not to ingress should not be confused with the induction period often reported in Case II systems. [144] The solvent front observed by MRI is broadened by the point spread function of the profile resolution. In consequence, in the early stages, when the distance ingressed is less than the profile resolution, the signal intensity within the first few pixels is seen to rise but the profile width does not increase appreciably. The Case II front velocities are given in Table 6.1. Values for the equilibrium surface PS fractions, calculated using the two methods described in Section 6.3.7, and the corresponding vapour pressures calculated from Equation 6.20 are shown in Table 6.2. Table 6.3 gives the mass of toluene arriving at the polymer surface for both of the surface fraction calculation methods. These are shown with the mass being taken up by the PS. In Figure 6.13 the Case II front velocity is compared to the flux arriving. As one can see in Figure 6.13, the Case II front velocity is proportional to the solvent vapour flux when the vapour flux is varied by changing the path length. There is good

Table 6.1: Toluene ingress Case II front velocity at different vapour path lengths

Path length/ mm	Front velocity/ $\mathrm{nms^{-1}}$
3	24.4
35	5.1
95	1.6
195	0.9

Table 6.2: The equilibrium PS surface fraction and corresponding vapour pressures as a fraction of the pure solvent vapour pressure calculated using the two different methodologies at different vapour path lengths

Path length/ mm	Surface PS fraction	p_{PS}/p_{tol}	Surface PS fraction	p_{PS}/p_{tol}
	Using two component fit		Using swelling	
3	0.46	0.95	0.53	0.92
35	0.52	0.93	0.64	0.85
95	0.70	0.79	0.70	0.79
195	0.75	0.72	0.67	0.82

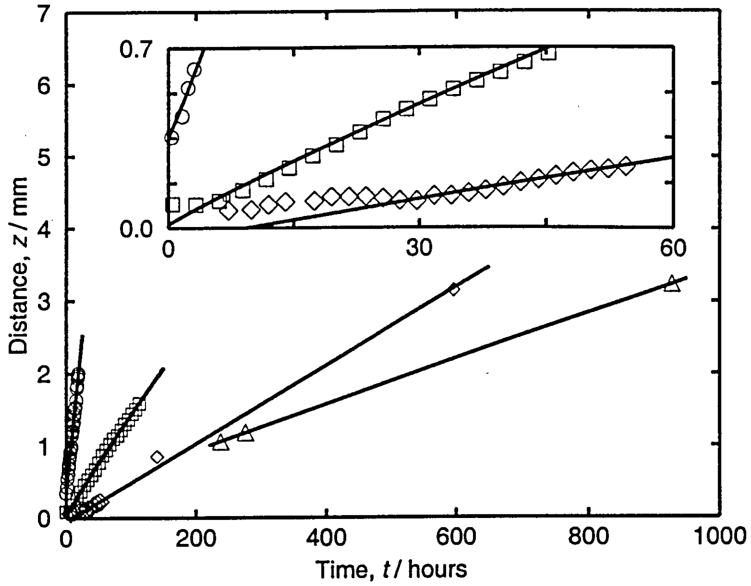

Figure 6.12: The Case II front position of toluene ingressing polystyrene at different vapour path lengths. The circles show a vapour path length of 3mm, the squares a path length of 35mm, the diamonds a path length of 95mm and the triangles a path length of 195mm

correlation over two orders of magnitude in spite of considerable errors involved in estimating both the swelling and the incident flux. This strongly suggests that we have observed Case II diffusion resulting from a limited surface flux. In their ion beam experiment at 20°C, Gall and Kramer [144] reported a front velocity of 0.04nms^{-1} for low activity deuterated toluene vapour ingressing polystyrene over an unspecified vapour path length. Our values also compare well with this. We extracted non-equilibrium diffusion coefficients from solvent concentration STRAFI profiles. Values of 5.7×10^{-8}, 6.8×10^{-8} and 5.8×10^{-8} cm^2/s were found for $\phi = 0.225$ at path lengths of 3.5, 9.5 and 19.5cm. These values are effectively the same as one would expect for a diffusion coefficient measured at the same solvent concentration and sample history. The values compare well with those found in the literature for similar systems. [40, 152]

Table 6.3: The toluene flux arriving at the surface of the PS compared to the mass taken up

Path length/ mm	Flux arriving/ gs^{-1}	Flux arriving/ gs^{-1}	Mass uptake/ gs^{-1}
	Using two component fit	Using swelling	
3	210×10^{-8}	330×10^{-8}	110×10^{-8}
35	4.1×10^{-8}	10×10^{-8}	22×10^{-8}
95	6.0×10^{-8}	5.7×10^{-8}	6.8×10^{-8}
195	3.7×10^{-8}	2.3×10^{-8}	4.0×10^{-8}

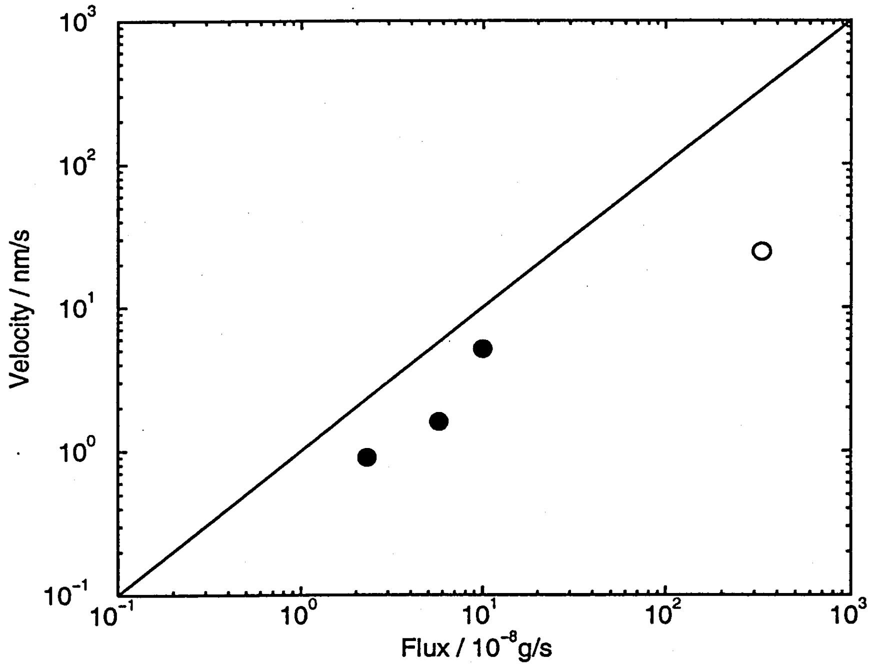

Figure 6.13: The Case II front velocity as a function of toluene vapour flux at the polystyrene surface. The filled circles are variable path length samples made with set-up A. The unfilled circle is the inverted sample where PS downward flow was a problem.

6.3.12 Changing the toluene vapour source activity

Aim

The aim of these experiments was to find how the Case II front velocity changed when the solvent supply was limited further by reducing the source activity.

Table 6.4: The activity of the toluene vapour of mixtures of PS and toluene at different concentrations

PS volume fraction	Activity
0.00	1.0
0.10	0.997
0.15	0.994
0.20	0.991
0.25	0.986
0.40	0.965
0.50	0.937
0.60	0.883

Experimental results

To reduce the activity, a of the toluene vapour source homogeneous mixtures of PS and toluene at varying concentrations were put into the solvent reservoir. The activity is given by Equation 6.20 since activity is equivalent to p_{PS}/p_{tol}. The mixtures were prepared by gently heating and stirring the PS and toluene over a period of days. Table 6.4 shows the different PS/ toluene mixtures used and the resulting activity. Experiments were performed with both set-up A and a path length of 35mm as well as with set-up B. Plots of the front position against time are shown in Figure 6.14. If the activity was reduced to below 0.883, no ingress was seen even when the sample was left for a number of weeks. The results shown in Figure 6.14 are what one would expect. The higher the activity of the toluene vapour the faster the front moves. The toluene ingress using sample set-up B, with a reduced vapour path, is quicker than using set-up A. Table 6.5 shows the Case II front velocities. Values for the equilibrium surface PS fractions and corresponding vapour pressures calculated from Equation 6.20 are shown in

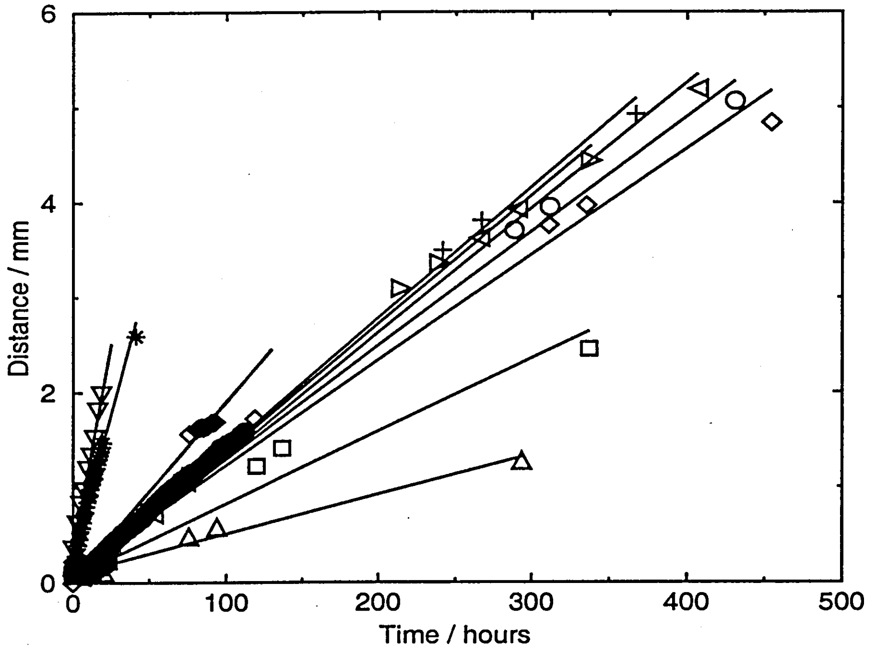

Figure 6.14: The front position of toluene ingressing polystyrene at different vapour activities. From left to right the associated activites are: triangles (down): a = 1.0 with set-up B, stars: a = 0.965 with set-up B, diamonds: a = 0.883 with set-up B, circles: a = 1.0 with set-up A, plus signs: a = 0.997 with set-up A, triangles (right): a = 0.994 with set-up A, triangles (left): a = 0.991 with set-up A, circles: a = 0.986 with set-up A, diamonds: a = 0.965 with set-up A, squares: a = 0.937 with set-up A, triangles (up): a = 0.883 with set-up A.

Tables 6.6 and 6.7 for set-ups A and B respectively. The mass taken up by the PS was calculated as before. The results using set-up A and set-up B are shown in Tables 6.8 and 6.9 respectively. In Figure 6.15 the Case II velocity is compared to the solvent flux arriving at the sample surface. Again, good correlation is found.

Table 6.5: Toluene ingress Case II front velocity with different toluene ativities in the solvent reservoir

Reservoir toluene activity	Front velocity/ nms^{-1}	
	Set-up A (35mm path length)	Set-up B
1.0	5.1	24.4
0.997	4.3	-
0.994	4.0	-
0.991	3.7	-
0.986	3.6	-
0.965	3.3	16.7
0.937	2.3	-
0.883	1.2	5.4

Table 6.6: The equilibrium PS surface fraction and corresponding vapour pressures as a fraction of the pure solvent vapour pressure calculated using the two different methodologies at different toluene reservoir activities. (Experiments performed with set-up A and a path length of 35mm)

Activity	Surface PS fraction	p_{PS}/p_{tol}	Surface PS fraction	p_{PS}/p_{tol}
	Using two component fit		Using swelling	
1.0	0.52	0.93	0.64	0.85
0.997	0.40	0.88	0.67	0.82
0.994	0.41	0.89	0.64	0.85
0.991	0.41	0.89	0.64	0.85
0.986	0.41	0.89	0.65	0.84
0.965	0.44	0.91	0.67	0.82
0.937	0.44	0.91	0.77	0.68
0.883	0.19	0.60	0.85	0.51

Table 6.7: The equilibrium PS surface fraction and corresponding vapour pressures as a fraction of the pure solvent vapour pressure calculated using the two different methodologies at different toluene reservoir activities. (Experiments performed with set-up B)

Activity	Surface PS fraction	p_{PS}/p_{tol}	Surface PS fraction	p_{PS}/p_{tol}
	Using two component fit		Using swelling	
1.0	0.46	0.95	0.53	0.92
0.965	0.42	0.96	0.13	0.99
0.883	0.62	0.87	0.70	0.79

Table 6.8: The toluene flux arriving at the surface of the PS compared to the mass taken up for different toluene activities in the solvent reservoir. (Experiments performed with set-up A)

Activity	Flux arriving/ gs^{-1}	Flux arriving/ gs^{-1}	Mass uptake/ gs^{-1}
	Using two component fit	Using swelling	
1.0	11.0×10^{-8}	10×10^{-8}	22×10^{-8}
0.997	7.9×10^{-8}	12×10^{-8}	19×10^{-8}
0.994	7.0×10^{-8}	9.7×10^{-8}	17×10^{-8}
0.991	6.8×10^{-8}	9.5×10^{-8}	16×10^{-8}
0.986	6.5×10^{-8}	9.8×10^{-8}	16×10^{-8}
0.965	3.7×10^{-8}	9.8×10^{-8}	14×10^{-8}
0.937	1.8×10^{-8}	17×10^{-8}	10×10^{-8}
0.883	19.4×10^{-8}	26×10^{-8}	3.9×10^{-8}

Table 6.9: The toluene flux arriving at the surface of the PS compared to the mass taken up for different toluene activities in the solvent reservoir. (Experiments performed with set-up B)

Activity	Flux arriving/ gs^{-1}	Flux arriving/ gs^{-1}	Mass uptake/ gs^{-1}
	Using two component fit	Using swelling	
1.0	210×10^{-8}	330×10^{-8}	110×10^{-8}
0.965	21×10^{-8}	27×10^{-8}	73×10^{-8}
0.883	55×10^{-8}	250×10^{-8}	8.7×10^{-8}

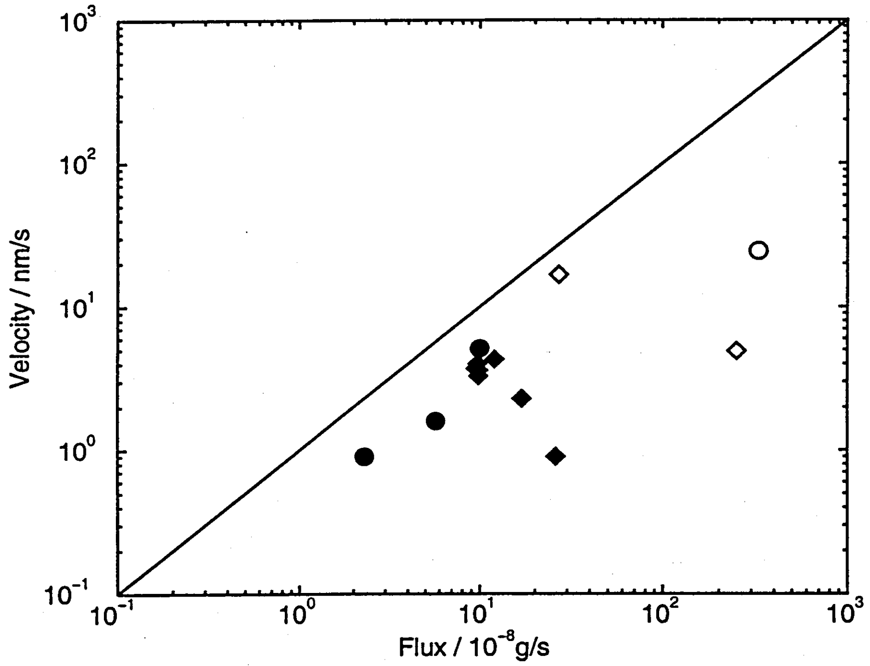

Figure 6.15: The Case II front velocity as a function of toluene vapour flux at the polystyrene surface. The circles are variable path length samples discussed in Section 6.3.11. The filled diamonds are variable reservoir activity samples made with set-up A. The unfilled diamonds are variable reservoir activity samples made with set-up B where downward flow of the PS was a problem

6.3.13 Temperature effects of toluene vapour ingressing PS

Aim

The aim of this set of experiments is to provide a large enough flux to remove the vapour flux as the rate-limiting step in diffusion. Increasing the temperature of the experiment greatly increases the flux. We expect the ingress to tend towards Fickian dynamics as the sample temperature is increased.

Experimental results

Sample set-up A with a path length of 35mm was used at temperatures T of 17.0, 41.5, 47.8, 73.3, 85.6 and 100.9°C. Figure 6.16 shows the solvent front position as a function of time.

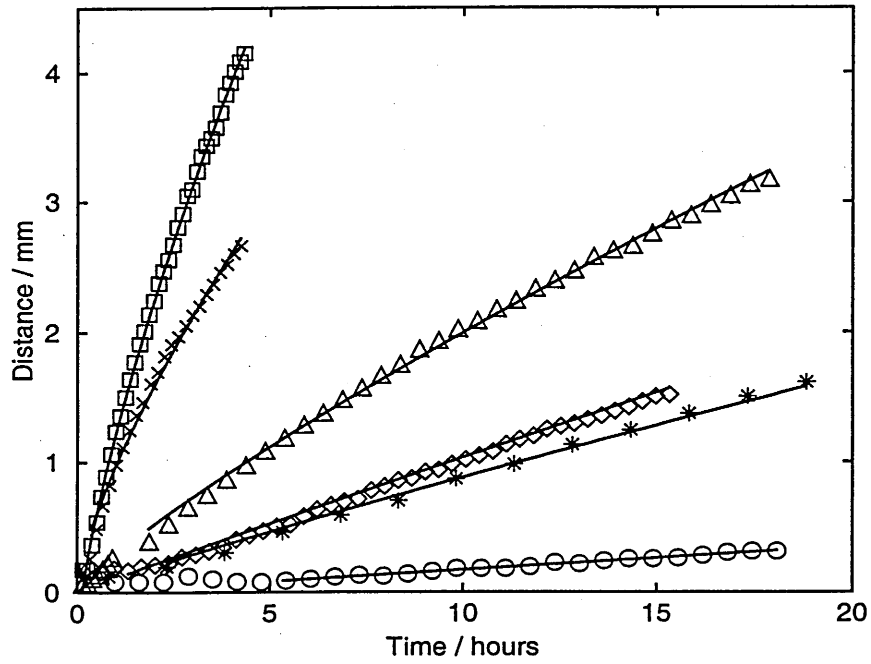

Figure 6.16: The effects on changing the temperature of toluene vapour ingressing PS. Key: 17.0°C: circles; 41.5°C: stars; 47.8°C: diamonds; 73.3°C: triangles; 85.6°C: crosses and; 100.9°C: squares.

These front positions were fitted against a curve of the form $x = At^n$ where x is distance, t is time and A and n are the fit parameters. The results are shown in Table 6.10. Between 17.0 and 47.8 °C the ingress of toluene appears to be Case II with a transition to the anomolous regime occuring above this temperature. With increasing temperature, the trend is towards Fickian diffusion.

An estimate was again made of the toluene vapour flux arriving at the surface of

Table 6.10: Best-fit parameters to the toluene vapour ingressing PS at varying temperature data in Figure 6.16

T/ °C	A	n	χ^2
17.0	14.8401	1.05930	1195.23
41.5	104.679	0.925358	18583.4
47.8	109.244	0.976306	9390.92
73.3	292.281	0.834292	57303.6
85.6	968.856	0.715899	89325.6
100.9	1477.71	0.738802	185460

the PS and the mass taken up by it. A number of further assumptions have been made in these calculations. Firstly, for all the samples for a short time period at the start of the experiment, ingress is assumed to be linear with time. This is valid because in the short time limit the ingress must be surface flux limited and hence one expects Case II behaviour. Secondly, it has been assumed that the Flory-Huggins interaction parameters are not a function of temperature. This assumption has had to be made due to the lack of available data in the literature. Shown in Table 6.11 are estimates of the linear front velocities as a function of temperature. The vapour pressure for toluene as a function of temperature was interpolated from Figure 6.9. These values are listed in Table 6.11. Using the same methods as before, equilibrium PS surface volume fractions were measured (Table 6.12) and used to find an estimate of the flux arriving at the surface of the polymer. This value is compared to the mass of toluene taken up by the PS calculated from the front velocity at short time (Table 6.13).

Broadly speaking, as temperature is varied, at short times, correlation exists between flux arriving and front velocity. This is shown in Figure 6.17. At higher temperatures where both surface flux and diffusivity in the polymer are higher,

Table 6.11: Pure toluene vapour pressures, diffusion coefficient of toluene vapour in air and estimated linear velocities at short experiment times all as a function of temperature

T/ °C	Toluene vapour pressure/ $\mathrm{Nm^{-2}}$	D_v/ $\mathrm{m^2s^{-1}}$	Front velocity/ $\mathrm{nms^{-1}}$
17.0	3000	1.75×10^{-5}	5.1
41.5	9160	1.83×10^{-5}	22.8
47.8	11700	1.84×10^{-5}	28.2
73.3	36000	1.92×10^{-5}	61.3
85.6	49100	1.95×10^{-5}	252.5
100.9	79100	1.99×10^{-5}	370.4

Table 6.12: The equilibrium PS surface fraction and corresponding vapour pressures as a fraction of the pure solvent vapour pressure calculated using the two different methodologies at different temperatures. (Experiments performed with set-up A and a path length of 35mm)

T/ °C	Surface PS fraction	p_{PS}/p_{tol}	Surface PS fraction	p_{PS}/p_{tol}
	Using two component fit		Using swelling	
17.0	0.52	0.93	0.64	0.85
41.5	0.27	0.98	0.50	0.94
47.8	0.37	0.97	0.59	0.89
73.3	0.25	0.99	0.47	0.95
85.6	0.35	0.97	0.58	0.90
100.9	0.40	0.96	0.53	0.92

Table 6.13: The toluene flux arriving at the surface of the PS compared to the mass taken up at various temperatures (Experiments performed with set-up A and a path length of 35mm)

T/ °C	Flux arriving/ gs^{-1}	Flux arriving/ gs^{-1}	Mass uptake/ gs^{-1}	Mass uptake/ gs^{-1}
	Using two component fit	Using swelling	Assuming Case II	Assuming Case II in short time
17.0	4.1×10^{-8}	10×10^{-8}	22×10^{-8}	5.6×10^{-8}
41.5	3.1×10^{-8}	12×10^{-8}	99×10^{-8}	48×10^{-8}
47.8	7.3×10^{-8}	28×10^{-8}	123×10^{-8}	49×10^{-8}
73.3	10×10^{-8}	35×10^{-8}	267×10^{-8}	43×10^{-8}
85.6	26×10^{-8}	100×10^{-8}	1098×10^{-8}	697×10^{-8}
100.9	55×10^{-8}	125×10^{-8}	1610×10^{-8}	923×10^{-8}

linear ingress breaks down, equivalent to varying the parameter β in the model. The effective surface concentration also varies with temperature as the Case II behaviour breaks down. This variation results in changing the relationship between vapour flux and front velocity.

Calculating the activation energy

At each temperature a diffusion coefficient was calculated at $\phi = 0.3$. If we assume that diffusivity in the rubber obeys an Arrhenius relationship then

$$D = D_0 e^{-\frac{E}{RT}} \tag{6.25}$$

where E is the activation energy, R is the universal gas constant and T is temperature. The gradient of a straight line of best-fit to a plot of $\ln D$ against $\frac{1}{T}$ will give E. This plot is shown in Figure 6.18. For the higher temperature sets, only the linear, early ingress was considered. Fitting to the more reliable lower temperture data, where pixel resolution is not a limiting factor, gives an activation energy of $E = 22\text{kJ/mol}$. This is comparable with literature values for small molecule diffusion processes in polymers. [18, 37, 144, 148]

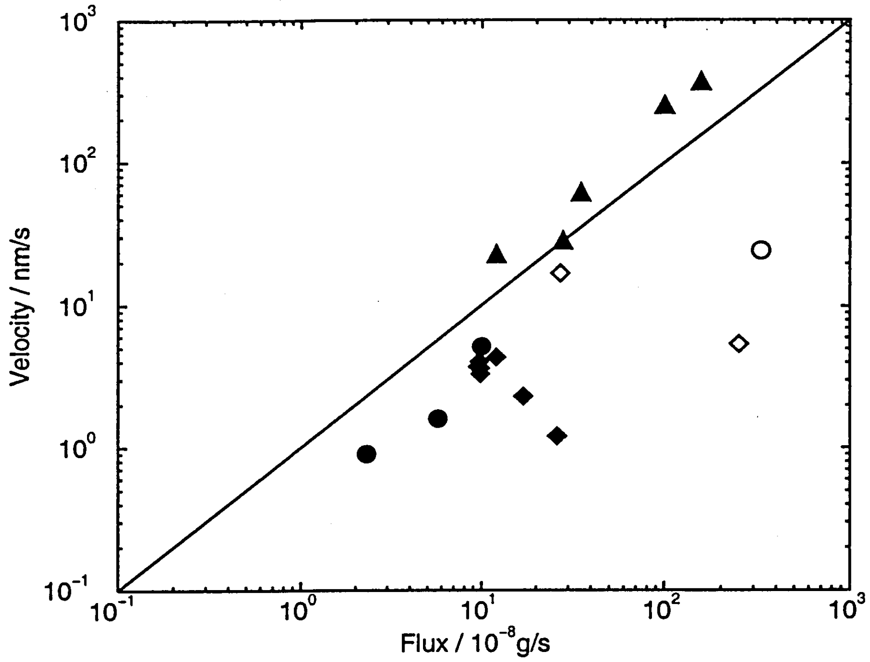

Figure 6.17: The Case II front velocity as a function of toluene vapour flux at the polystyrene surface. The circles are variable path length samples discussed in Section 6.3.11. The diamonds are variable reservoir activity samples discussed in Section 6.3.12. The triangles are data recorded as a function of temperature

6.4 Discussion

The results of this chapter explain a number of puzzles originating from earlier work.

- A plausible explanation emerges as to why, in experiments looking at acetone vapour ingress into PVC, the polymer chain dynamics were observed to evolve across the rubber region. This equated to evolution for long periods (days). [145] With limited solvent flux at the sample surface, the solvent concentration in the polymer is near uniform and is close to that corresponding to the glass-rubber transition rather than the (much higher) equilibrium concentration. The (very) small concentration gradient close to the transition is sufficient to give rise to large changes in polymer mobility.

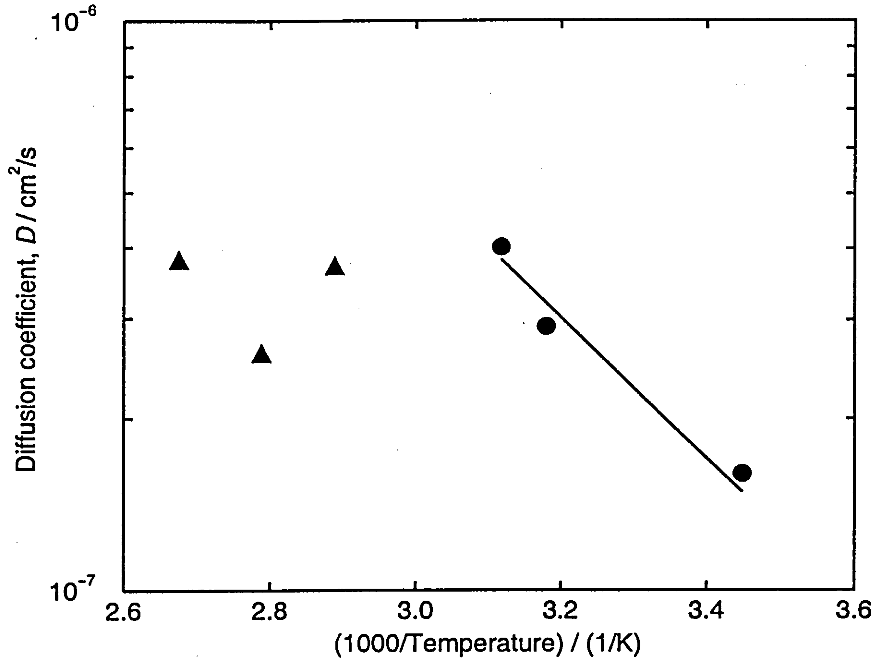

Figure 6.18: The effects on changing the temperature on the diffusion coefficient The triangles and circles show the diffusion coefficients at $\phi = 0.30$ as a function of temperature. At high temperatures, the ingress tends towards Fickian and these points (the triangles) are neglected in the best-fit solid line.

- It also becomes possible to explain the unusually large extent of the Fickian precursor ahead of the main solvent front seen in the same acetone vapour ingress experiments. In the model as described in Section 6.2, the solvent diffusivity in the glass is set to zero. In reality, it will be very small, but non-zero. With low vapour flux, the Fickian precursor has time to build.

- The new results explain why some systems can be both Fickian and Case II. The observed diffusion depends on experimental conditions and not on the visco-elastic properties of the polymer. For solvent-flux-limited Case II diffusion, the Case II velocity depends solely on the solvent flux at the surface.

- It is possible, too, that the current work explains why the ion beam data of Hui *et al* [146] on iodohexane ingress into polystyrene led these authors to infer solvent diffusivities in the glassy state which apparently varied between samples. The experiment involved exposing glassy polymer to vapour above equilibrated iodohexane/ polystyrene solutions. The front velocity increased markedly with the solvent fraction in the reservoir. It is now apparent that the variable in this work was the vapour flux to which the samples were exposed.

We have demonstrated both by simple numerical modeling and by experiment that limiting the flux of a solvent impinging on a glassy polymer sample can result in Case II diffusion of the solvent into the polymer. This contrasts with Case II diffusion as normally described [17], where the rate limiting step is the swelling of the polymer at the solvent front. It has been shown that by varying the solvent flux, it is possible to vary the Case II front velocity. It is worth emphasising that the low surface flux is necessary but not sufficient to cause Case II ingress of this kind. A low flux of diffusant applied to a matrix will normally result in Fickian transport. The special boundary condition of the glass-to-rubber transition remains necessary for linear ingress. Without it, even if the diffusion coefficient is a strong function of concentration, the flux at the solvent front is always proportional to the concentration gradient and generalised Fickian diffusion must result, with D a function of c. It is also worth emphasising that Case II diffusion is a transitory phenomena. Left long enough in a sufficiently large system, the diffusion will always revert to Fickian behaviour.

It has been shown that the solvent diffusion coefficient can be derived readily from the solvent concentration profile when the incident solvent flux is limited. It is suggested that, with higher temporal and spatial resolution data, this provides a means of readily accessing the concentration history dependence of the diffusivity – if such history dependence exists – in the region of the solvent-induced glass transition.

A paper of the work in this chapter has been submitted to *Macromolecules.*

Appendix A

Derivation of multi-component atomistic diffusion equation

Here we derive Equation 3.11. This is the equation used for multi-component diffusion. Consider two diffusing species r and s from a larger number t. Thus

$$i = 1, 2, \ldots, r, s, \ldots, t. \tag{A.1}$$

There are n_r^m molecules of species r in a plane (y, z) at position m along the x direction (which is the direction of diffusion) and n_s^m molecules of species s in a plane (y, z) at position m. The total number of molecules in the plane (y, z) at m is given by N where

$$N = \sum_{i=1}^{t} n_i^m. \tag{A.2}$$

We now calculate the net flux of the different species across a surface between position m and $m + 1$ arising from mutual exchange of atoms in neighbouring planes m and $m + 1$ with the same y and z coordinate. If the probability of type r in plane m exchanging position with a species of type s at $m + 1$ (where the neighbours r and s have the same y and z coordinate) per unit time is $P_{r,s}$, then the flux of r crossing *forwards* from position m to position $m+1$ previously occupied by s is $F_{forward}$, and we can write:

$$F_{forward} = P_{r,s} n_r^m \frac{n_s^{m+1}}{N} = \frac{P_{r,s}}{N} n_r^m (n_s^m + \frac{dn_s^m}{dx}\Delta x) \tag{A.3}$$

where Δx is the distance in the x direction between plane m and $m+1$. Similarly we can write the reverse flux of r from plane $m+1$ to plane m, $F_{reverse}$ as:

$$F_{reverse} = P_{r,s} n_s^m \frac{n_r^{m+1}}{N} = \frac{P_{r,s}}{N} n_s^m (n_r^m + \frac{dn_r^m}{dx}\Delta x). \tag{A.4}$$

Hence the net flux number is:

$$F_{forward} - F_{reverse} = \frac{P_{r,s}}{N}\left(n_r^m \frac{dn_s^m}{dx} - n_s^m \frac{dn_r^m}{dx}\right)\Delta x. \tag{A.5}$$

$P_{r,s}$ is proportional to the diffusion coefficient $D_{r,s}$. n_r^m is proportional to concentration ϕ_r hence summing over all species, the flux of component i is:

$$F_i = \frac{\sum_{i \neq j} D_{i,j}}{\sum_k \phi_k}\left(\phi_i \frac{\partial \phi_j}{\partial x} - \phi_j \frac{\partial \phi_i}{\partial x}\right). \tag{A.6}$$

This is Equation 3.10. From Fick's second law we can then write that:

$$\frac{\partial \phi_i}{\partial t} = \frac{1}{\sum_k \phi_k}\left[\sum_{i \neq j} \frac{\partial}{\partial x} D_{i,j}\left(\phi_j \frac{\partial \phi_i}{\partial x} - \phi_i \frac{\partial \phi_j}{\partial x}\right)\right]. \tag{A.7}$$

This is Equation 3.11.

Bibliography

[1] C. Hall. *Polymer Materials: An Introduction for Technologists and Scientists.* Macmillan Education Ltd., Basingstoke, UK, 1989.

[2] N. G. McCrum, C. P. Buckley, and C. B. Bucknall. *Principles of Polymer Engineering.* Oxford Science Publications, Oxford, UK, 1997.

[3] F. Rodriguez. *Principles of Polymer Systems.* Taylor and Francis, Washington D.C., USA, 1996.

[4] I. M. Campbell. *Introduction to Synthetic Polymers.* Oxford University Press, Oxford, UK, 2000.

[5] A. Yu. Grosberg and A. R. Khokhlov. *Giant Molecules.* Academic Press, San Diego, California, USA, 1997.

[6] K. J. Laidler and J. H. Meiser. *Physical Chemistry.* Houghton Mifflin Company, Boston, Massachusetts, USA, 1999.

[7] A. Fick. *Annalen der Physik*, 170:59, 1855.

[8] J. Crank. *The Mathematics of Diffusion.* Oxford University Press, Oxford, UK, 1975.

[9] K. Ueberreiter and F. Asmussen. *Journal of Polymer Science*, 57:187, 1962.

[10] T. Alfrey. *Chemical Engineering News*, 43:64, 1965.

[11] P. J. Mills, C. J. Palstrom, and E. J. Kramer. *Journal of Materials Science*, 21:1479, 1986.

[12] P. J. Mills and E. J. Kramer. *Journal of Materials Science*, 21:4151, 1986.

[13] T. K. Kwei, T. T. Wang, and H. M. Zupko. *Macromolecules*, 5:645, 1972.

[14] A. Kumar and R. K. Gupta. *Fundamentals of polymers.* McGraw-Hill, New York, USA, 1998.

[15] J. Crank. *Journal of Polymer Science*, 11:151, 1953.

[16] S. Parker. PhD thesis, Department of Physics, University of Surrey, Guildford, Surrey, UK, 1999.

[17] N. L. Thomas and A. H. Windle. *Polymer*, 23:529, 1982.

[18] D. M. Lane, P. J. McDonald, and J. L. Keddie. In R. Botto P. Blumler, B. Blumich and E. Fukushima, editors, *Spatially Resolved Magnetic Resonance.*, Weinheim, Germany, 1998. Wiley-VCH.

[19] W. C. Wu and N. A. Peppas. *Journal of Applied Polymer Science*, 49:1845, 1993.

[20] P. J. McDonald and R. Sackin. Unpublished result.

[21] G. D. Cody and R. E. Botto. *Macromolecules*, 27:2607, 1994.

[22] P. J. Flory. *Principles of Polymer Chemistry.* Cornell University Press, Ithaca, New York, USA, 1953.

[23] M. L. Huggins. *Physical Chemistry of High Polymers.* Wiley, New York, USA, 1958.

[24] S. Gunduz and S Dincer. *Polymer*, 21:1041, 1980.

[25] H-M. Petri, N. Schuld, and B. A. Wolf. *Macromolecules*, 28:4975, 1995.

[26] R. .A. Orwoll. *Rubber Chemistry and Technology*, 50:451, 1977.

[27] T. M. Hyde, L. F. Gladden, M. R. Mackley, and P. Gao. *Journal of Polymer Science: Part A: Polymer Chemistry*, 33:1795, 1995.

[28] T. J. Roseman and S. Z. Mansdorf. *Controlled Release Delivery.* Marcel Dekker, New York, USA, 1983.

[29] L. F. Thompson, C. G. Wilson, and M. J. Bowden. *Introduction to Microlithography.* American Chemical Society, Washington D.C., USA, 1983.

[30] H. Okuno, K. Renzo, and T. Uragami. *Journal of Membrane Science*, 103:31, 1995.

[31] J. S. Vrentas, C. M. Jarzebski, and J. L. Duda. *AIChe Journal*, 21:94, 1975.

[32] S. J. Black, A. H. L. Chamberlain, T. D. Hart, D. M. Lane, and P. J. McDonald. In *Proceedings of the 28th Congress Ampere, Extended Abstracts*, 1996.

[33] T. M. Aminabhavi and H. G. Naik. *Polymers and Polymer Composites*, 6:205, 1998.

[34] K. L. Perry, P. J. McDonald, and A. S. Clough. *Magnetic Resonance Imaging*, 12:217, 1994.

[35] I. Devotta, V. Premnath, M. V. Badiger, P. R. Rajamohanan, S. Ganapathy, and R. A. Mashelkar. *Macromolecules*, 27:532, 1994.

[36] J. Manjkow, J. S. Papanu, D. S. Soong, D. W. Hess, and A. T. Bell. *Journal of Applied Physics*, 62:682, 1987.

[37] M. Ercken, P. Adriaensens, D. Vanderzande, and J. Gelan. *Macromolecules*, 28:8541, 1995.

[38] P. Mansfield, R. Bowtell, and S. Blackband. *Journal of Magnetic Resonance*, 99:507, 1992.

[39] P. Y. Ghi, D. J. T. Hill, D. Maillet, and A. K. Whittaker. *Polymer*, 38:3985, 1997.

[40] L. A. Weisenberger and J. L. Koenig. *Macromolecules*, 23:2445, 1990.

[41] J. Wironen, C. Shen, J. Yan, and C. Batich. *Journal of Applied Polymer Science*, 59:825, 1996.

[42] J. R. Lu, E. M. Lee, and R. K. Thomas. *Acta Crystallographica Section A*, 52:11, 1996.

[43] K. Tang and Z. Zhang. *Journal of Polymer Science: Part B: Polymer Physics*, 34:1175, 1996.

[44] T. P. Russell. *Material Science Reports*, 5:171, 1990.

[45] F. Bloch, W. W. Hansen, and M. Packard. *Physical Review*, 70:474, 1946.

[46] E. M. Purcell, H. C. Torrey, and R. V. Pound. *Physical Review*, 69:37, 1946.

[47] N. Bloembergen, E. M. Purcell, and R.V. Pound. *Physical Review*, 73:679, 1948.

[48] W. G. Proctor and F. C. Yu. *Physical Review*, 77:17, 1950.

[49] W. C. Dickinson. *Physical Review*, 77:736, 1950.

[50] E. L. Hahn. *Physical Review*, 80:580, 1950.

[51] R. R. Ernst. *Advances in Magnetic Resonance*, 2:1, 1966.

[52] R. R. Ernst and W. A. Anderson. *The Review of Scientific Instruments*, 37:93, 1966.

[53] P. C. Lauterbur. *Nature*, 242:190, 1973.

[54] P. Mansfield and P. K. Grannell. *Journal of Physics C*, 6:422, 1973.

[55] J. B. Aguayo, S. J. Blackband, J. Shoeniger, M. A. Mattingley, and M. A. Hinterman. *Nature*, 322:198, 1986.

[56] C. D. Eccles and P. T. Callaghan. *Journal of Magnetic Resonance*, 68:393, 1986.

[57] P. C. Lauterbur. In S. Chien and C. Ho, editors, *NMR in Biology and Medicine*, New York, USA, 1986. Raven Press.

[58] H. Kamei and Y Katayama. *IEEE/ eighth annual conference of the engineering in medicine and biology society, abstracts*, page 1159, 1986.

[59] A. A. Samoilenko, D. Y. Artemov, and A. L. Sibel'dina. *JETP Letters*, 47:348, 1988.

[60] R. K. Harris. *Nuclear Magnetic Resonance Spectroscopy.* Longman Scientific and Technical, Harlow, UK, 1994.

[61] R. M. Steinfeld, G. C. Bassler, and T. C. Morrill. *Spectrometric Identification of Organic Compounds.* John Wiley and Sons, New York, USA, 1991.

[62] P. J. McDonald. *Progress in Nuclear Magnetic Resonance Spectroscopy*, 30:69, 1997.

[63] U. Goerke, P. J. McDonald, and R. Kimmich. In J. H. Moore and N. D. Spencer, editors, *Encyclopedia of Chemical Physics and Physical Chemistry.* IOP publishing, Philadelphia, USA, 1999.

[64] P. T. Callaghan. *Principles of Nuclear Magnetic Resonance Microscopy.* Oxford Science Publications, Oxford, England, 1991.

[65] A. A. Samoilenko, D. Y. Artemov, and A. L. Sibel'dina. *Bruker Report*, 2:30, 1987.

[66] J. B. Miller and A. N. Garroway. *US Patent 5 126 674*, 1992.

[67] P. J. McDonald and B. Newling. *Reports on Progress in Physics*, 61:1441, 1998.

[68] E. Fukushima and S. B. W. Roeder. *Experimental Pulse NMR: a Nuts and Bolts Approach.* Addison-Wesley, Reading, Massachusetts, USA, 1981.

[69] D. I. Hoult. *Progress in NMR Spectroscopy*, 12:41, 1978.

[70] C. E. Hayes, W. A. Edelstein, J. F. Schenck, O. M. Meuller, and M. Eash. *Journal of Magnetic Resonance*, 63:622, 1985.

[71] D. I. Hoult and R. E. Richards. *Journal of Magnetic Resonance*, 24:71, 1976.

[72] A. G. Webb and L. D. Hall. *Polymer*, 32:2926, 1991.

[73] A. A. Maudsley, S. K. Hilal, W. H. Perman, and H. E. Simon. *Journal of Magnetic Resonance*, 51:147, 1983.

[74] B. Newling, S. J. Gibbs, L. D. Hall, D. E. Haycock, W. J. Frith, and S. Ablett. *Chemical Enginerring Science*, 52:2059, 1997.

[75] C. Kunze and R. Kimmich. *Magnetic Resonance Imaging*, 12:805, 1994.

[76] M. Heidenreich, W. Kockenberger, R. Kimmich, N. Chandrakumar, and R. Bowtell. *Journal of Magnetic Resonance*, 132:109, 1998.

[77] A. Spyros, N. Chandrakumar, M. Heidenreich, and R. Kimmich. *Macromolecules*, 31:3021, 1998.

[78] S. R. Hartmann and E. L. Hann. *Physical Review*, 128:2042, 1962.

[79] M. H. Levitt. *Journal of Chemical Physics*, 94:30, 1991.

[80] N. Chandrakumar and R. Kimmich. *Journal of Magnetic Resonance*, 137:100, 1999.

[81] M. Born and E. Wolf. *Principles of Optics.* Cambridge University press, Cambridge, UK, 1997.

[82] R. M. A. Azzam and N. M. Bashara. *Ellipsometry and Polarized Light.* North- Holland, Amsterdam, The Netherlands, 1977.

[83] A. Zuber, H. Janchen, and N. Kaiser. *Applied Optics*, 35:5553, 1996.

[84] J-P. Drolet, S. V. Russev, M. I. Boyanov, and R. M. Leblanc. *Journal of the Optical Society of America*, A11:3284, 1994.

[85] D. W. Marquardt. *Journal of the Society of Industrial and Applied Mathematics*, 11(2):431, 1963.

[86] R. W. Richards and S. K. Peace. *Polymer Surfaces and Interfaces III.* John Wiley and Sons, Ltd., Chichester, UK, 1999.

[87] J. A. Woollam Co., Inc., Lincoln, Nebraska, USA. *Guide to Using WVASE32.*

[88] C. S. Tsay and A. J. McHugh. *Journal of Polymer Science: Part B: Polymer Physics*, 28:1327, 1990.

[89] W. J. Cooper, P. D. Krasicky, and F. Rodriguez. *Journal of Applied Polymer Science*, 31:65, 1986.

[90] F. A. Long and L. J. Thompson. *Journal of Polymer Science*, 14:321, 1954.

[91] S. Prager and F. A. Long. *Journal of the American Chemical Society*, 73:4072, 1951.

[92] T. K. Kwei and H. M. Zupko. *Journal of Polymer Science: Part A-2*, 7:867, 1969.

[93] W. V. Titow, M. Braden, B. R. Currell, and R. J. Loneragen. *Journal of Applied Polymer Science*, 18:867, 1974.

[94] G. W. Miller, S. A. D. Visser, and A. S. Morecroft. *Polymer Engineering and Science*, 11:73, 1971.

[95] A. G. Webb and L. D. Hall. *Polymer Communications*, 31:425, 1990.

[96] P. J. Shatzberg. *Journal of Physical Chemistry*, 67:776, 1963.

[97] R. F. Fedors. *Polymer*, 21:207, 1980.

[98] C. Bindschaedler, R. Gurny, E. Doelker, and N. A. Peppas. *Journal of Colloid and Interface Science*, 108:75, 1985.

[99] E. A. van der Zeeuw, L. M. C. Sagis, and G. J. M. Koper. *Macromolecules*, 29:801, 1996.

[100] K. Ueberreiter. In J. Crank and G. S. Park, editors, *Diffusion in Polymers*, New York, USA, 1968. Academic.

[101] I. Devotta and R. A. Mashelkar. *Chemical Engineering Communications*, 156:31, 1996.

[102] B. Narasimhan and N. A. Peppas. *Macromolecules*, 29:3283, 1996.

[103] J. Brandrup, E. H. Immergut, and E. A. Grulke. *Polymer Handbook.* Wiley, New York, USA, 1999.

[104] C. E. H. Bawn, R. F. J. Freeman, and A. R. Kamaliddin. *Transactions of the Faraday Society*, 46:677, 1950.

[105] L. H. Sperling. *Introduction to Physical Polymer Science.* Wiley, New York, USA, 1992.

[106] E. L. Cussler and E. N. Lightfoot. *Journal of Physical Chemistry*, 69:1135, 1965.

[107] R. B. Bird, W. E. Stewart, and E. N. Lightfoot. *Transport phenomena.* Wiley, New York, USA, 1960.

[108] C. F. Curtiss and J. O. Hirschfelder. *Journal of Chemical Physics*, 17:550, 1949.

[109] G. S. Park. *Journal of Polymer Science*, 11:97, 1953.

[110] A. T. Hutcheon, R. J. Kokes, J. L. Hoard, and F. A. Long. *Journal of Chemical Physics*, 20:1232, 1952.

[111] P. H. Tang, C. J. Durning, C. J. Guo, and D. DeKee. *Polymer*, 38:1845, 1997.

[112] U. W. Gedde. *Polymer Physics.* Chapman and Hall, London, UK, 1995.

[113] K. Fuchs, C. Friedrich, and J. Weese. *Macromolecules*, 29:5893, 1996.

[114] J. R. Royer, J. M. DeSimone, and S. A. Khan. *Macromolecules*, 32:8965, 1999.

[115] B. R. Baird, H. B. Hopfenberg, and V. T. Stannett. *Polymer Engineering and Science*, 11:274, 1971.

[116] K. Umezawa, W. M. Gibson, J. T. Welch, K. Araki, G. Barros, and H. L. Frisch. *Journal of Applied Physics*, 71:681, 1992.

[117] M. M. Hassan and C. J. Durning. *Journal of Polymer Science: Part B: Polymer Physics*, 37:3159, 1999.

[118] M. M. Hassan, C. J. Durning, H. M. Tong, and K. W. Lee. In K. L. Mittal and K.W. Lee, editors, *Polymer Surfaces and Interfaces: Characterisation, Modification and Application.* VSP, Utrecht, Netherlands, 1996.

[119] S. R. Lustig, J. M. Caruthers, and N. A. Peppas. *Chemical Engineering Science*, 47:3037, 1992.

[120] D. W. Schubert. *Polymer Bulletin*, 38:177, 1997.

[121] W. M. Prest and D. J. Luca. *Journal of Applied Physics*, 50:6067, 1979.

[122] W. M. Prest and D. J. Luca. *Journal of Applied Physics*, 51:5170, 1980.

[123] J. C. Bray and H. B. Hopfenberg. *Journal of Polymer Science B*, 7:679, 1969.

[124] Y. Cohen and S. Reich. *Journal of Polymer Science: Polymer Physics*, 19:599, 1981.

[125] K. H. Storks. *Journal of the American Chemical Society*, 60:1753, 1938.

[126] A. Keller. *Philosophical Magazine*, 2:1171, 1957.

[127] P. H. Till. *Journal of Polymer Science*, 24:30, 1957.

[128] E. W. Fischer. *Zeitschrift fur Naturforschung*, 12a:753, 1957.

[129] S. Sawamura, H. Miyaji, K. Izumi, S. J. Sutton, and Y. Miyamoto. *Journal of the Physical Society of Japan*, 67:3338, 1998.

[130] S. J. Sutton, K. Izumi, H. Miyaji, Y. Miyamoto, and S. Miyashita. *Journal of Materials Science*, 32:5621, 1997.

[131] A. Bax, R. Freeman, and S. P. Kempsell. *Journal of the American Chemical Society*, 102:4849, 1980.

[132] E. R. Bodenhausen. *Principles of Nuclear Magnetic Resonance in One and Two Dimensions.* Clarendon Press, Oxford, UK, 1987.

[133] M. Klinkenberg, P. Blumler, and B Blumich. *Journal of Magnetic Resonance Series A*, 119:197, 1996.

[134] M. Sullivan, J. W. Taylor, and C. Babcock. *Journal of Vacuum Science and Technology B: Microelectronics Processing*, 9:3423, 1991.

[135] J. C. Charmet and P. G. de Gennes. *Journal of the Optical Society of America*, 73:1777, 1983.

[136] H. G. Tompkins. *A User's Guide to Ellipsometry.* Academic Press, San Diego, USA, 1993.

[137] R. Lennart. University of Cambridge, Personal communication.

[138] E. Aarts and J. Korst. *Simulated Annealing and Boltzmann Machines: A Stochastic Approach to Combinatorial Optimization and Neural Computing.* John Wiley and Sons, Chichester, UK, 1989.

[139] R. H. J. M. Otten and L. P. P. van Ginneken. *The Annealing Algorithm.* Kluwer Academic Publishers, Norwell, USA, 1989.

[140] N. P. Barradas, J. L. Keddie, and R. Sackin. *Physical Review E*, 59:6138, 1999.

[141] W. Chu, J. W. Mayer, and M. Nicolet. *Backscattering Spectrometry.* Academic Press, San Diego, USA, 1978.

[142] C. Jeynes, N. P. Barradas, M. J. Blewett, and R. P. Webb. *Nuclear Instruments and Methods B*, 136-138:1229, 1998.

[143] E. D. Palik. *Handbook of Optical Constants.* Academic, London, England, 1991.

[144] T. P. Gall and E. J. Kramer. *Polymer*, 32:265, 1991.

[145] K. L. Perry, P. J. McDonald, E. W. Randall, and K. Zick. *Polymer*, 13:2744, 1994.

[146] C. Y. Hui, K. C. Wu, R. C. Lasky, and E. J. Kramer. *Journal of Applied Physics*, 61:5137, 1987.

[147] P. Gao and M. R. Mackley. *Proceedings of the Royal Society of London A*, 444:267, 1994.

[148] R. C. Lasky, E. J. Kramer, and C. Y. Hui. *Polymer*, 29:1131, 1988.

[149] E. H. Kennard. *Kinetic Theory of Gases.* McGraw-Hill Book Company, New York, USA, 1938.

[150] R. C. Weast. *Handbook of Chemistry and Physics.* CRC Press, Cleveland, Ohio, USA, 1974.

[151] T. B. Benson and P. J. McDonald. *Journal of Magnetic Resonance*, A112:17, 1995.

[152] D. M. Lane and P. J. McDonald. *Polymer*, 38:2329, 1997.